The Sunyaev-Zel'dovich Effect as a Probe of the Thermodynamics of Extragalactic Systems

by

Devin Thomas Crichton

A dissertation submitted to The Johns Hopkins University in conformity with the requirements for the degree of Doctor of Philosophy.

Baltimore, Maryland

July, 2017

Abstract

The thermal Sunyaev-Zel'dovich effect is a spectral distortion of the cosmic microwave background that enables the study of the thermal state of ionized gas in extragalactic systems. The magnitude of this effect is proportional to the electron pressure distribution, and its integrated signal directly relates to the thermal energy of ionized gas. Additionally, as it does not suffer from cosmic surface brightness dimming, it enables observations out to arbitrarily high redshift. In this thesis, I present three studies which utilize this effect. In the first, I demonstrate a strong detection of the the average Sunyaev-Zel'dovich signal from radio selected galaxies, based on a statistical study of these systems. While these objects are thought to host powerful, accreting black holes whose associated jets could provide significant energetic input into the ionized halo gas, the results are consistent with expectations from purely gravitational heating. Conversely, in the second study, using a similar statistical analysis of optically selected radio-quiet quasars, I show evidence for a Sunyaev-Zel'dovich signal that is difficult to explain from purely gravitational arguments. The modeling favors a scenario in which much of the thermal energy originates from a coupling of the bolometric output of the luminous quasar emission to the ionized host halo,

ABSTRACT

with an efficiency of $\sim$15%. Finally, in the third study, I evaluate the constraints on the radial distribution of the electron pressure in massive, Sunyaev-Zel'dovich selected galaxy clusters. Here I extract constraints on the average self-similar pressure profiles of these systems finding no strong evidence for evolution in their shape. However, an increase in intrinsic scatter around these best fit profiles, from $\sim$45% to 70–90% from $z \sim 0.37$ to 0.67, is observed. This increase in intrinsic scatter has not previously been detected and indicates that non-gravitational processes could have an enhanced influence on these systems in earlier epochs of cosmic history.

Primary Reader: Prof. Tobias A. Marriage

Secondary Reader: Prof. Nadia L. Zakamska

Acknowledgments

I am grateful to my wife Carolyn for all the love and support she has provided during my time as a graduate student. Her constant encouragement made this work possible. I would also like to thank my family for their enduring support and, in particular, my mother, whose guidance and care have always been appreciated. To all my friends in Baltimore, and around the world, I thank you for your support over the years and, to those of you who I will shortly be saying goodbye to, I will miss the times we spent together dearly. I am grateful to all the mentors I have had throughout my scientific development, especially to Prof. Kavilan Moodley who introduced me to the fields of Astrophysics and Cosmology as well as to the ACT collaboration. I am greatly appreciative of all the members of this collaboration, without whom the data I have relied on for this work would not exist. Their efforts and support through my time as a graduate student have been invaluable. In particular, I would like to thank my advisor, Prof. Tobias Marriage, whose guidance, encouragement, and friendship has allowed me to make the most of my time at Johns Hopkins and greatly aided in my professional development. I look forward to working closely with him for many years to come. I am additionally grateful to my collaborators, in particular

ACKNOWLEDGMENTS

Dr Megan Gralla, Prof. Nadia Zakamska and Kirsten Hall, all of whom have played an integral role in the work I have presented here. I would like to acknowledge the funding opportunities provided to me through the Fulbright Foreign Student Program. I will always be proud to have been a part of this fantastic program, and I look forward to maintaining my connection with the brilliant community of international scholars it has produced. This work was supported by the US National Science Foundation through awards AST-0408698 and AST-0965625 for the ACT project, as well as awards PHY-0855887 and PHY-1214379. Funding was also provided by Princeton University, the University of Pennsylvania, and a Canada Foundation for Innovation (CFI) award to UBC. ACT operates in the Parque Astronómico Atacama in northern Chile under the auspices of the Comisión Nacional de Investigación Científica y Tecnológica de Chile (CONICYT). Computations were performed on the GPC supercomputer at the SciNet HPC Consortium. SciNet is funded by the CFI under the auspices of Compute Canada, the Government of Ontario, the Ontario Research Fund – Research Excellence; and the University of Toronto. We acknowledge the use of the Legacy Archive for Microwave Background Data Analysis (LAMBDA), part of the High Energy Astrophysics Science Archive Center (HEASARC). HEASARC/LAMBDA is a service of the Astrophysics Science Division at the NASA Goddard Space Flight Center. This research made use of Astropy, a community-developed core python package for Astronomy (Astropy Collaboration et al., 2013) and the affine invariant MCMC ensemble sampler implementation provided by the emcee python package (Foreman-Mackey et al., 2013). Additionally, tools from scikit-learn (Pedregosa et al., 2011) were used.

Dedication

This thesis is dedicated to my wife Carolyn, my family, Lauren, Ryan, Christine and Graham, and my shining golden labrador Hank.

Contents

List of Tables

List of Figures

Chapter 1

Introduction

In this Chapter I will briefly outline the theoretical foundations upon which the studies presented in this work rely. I will introduce the general relativistic framework that describes the evolution of the smooth cosmological background and then briefly discuss the behavior of density perturbations within this background. It is from these perturbations that the structures we observe throughout the Universe form. In this cosmological context, I will introduce our current theoretical understanding of the self-similar expectations for the thermodynamics of the gravitationally heated ionized gas hosted by massive halos. Additionally, the role of astrophysical processes (such as energetic feedback) in breaking these predictions will be discussed. Finally, I will introduce the datasets that have made this work possible.

Throughout this thesis, I will assume a geometrically flat, ΛCDM (Cold Dark Matter with cosmological constant, Λ) cosmology, which I will introduce below. This concordance

cosmology is consistent with a broad range of observations.

1.1 Cosmology and Structure Formation

1.1.1 The Smooth Cosmological Background

The Flat-ΛCDM cosmology begins with the assumption of an isotropic and homogeneous universe described by the Friedmann-Lamaître-Robertson-Walker (FLRW, Friedmann, 1922) metric,

$$\mathrm{d}s^2 = c^2\,\mathrm{d}t^2 - a^2(t)\,\mathrm{d}\vec{x}^2, \tag{1.1}$$

Here, $a(t)$ is the cosmological scale factor that describes the evolution of physical distances in the expanding spacetime, with respect to the comoving coordinates, $\vec{x}$.

Under this metric and within the Flat-ΛCDM paradigm, the general relativistic field equations provide a description of a universe whose evolution depends only on the relative contributions to the overall energy density of cold dark matter, regular (denoted as baryonic) matter, radiation and the cosmological constant. See, for example, Dodelson (2003) and Weinberg (2008) for reviews of modern cosmology. This evolution is described through the differential equations for the scale parameter known as the Friedmann equations,

$$H^2 \equiv \left(\frac{\dot{a}}{a}\right)^2 = \frac{8\pi G}{3}\rho + \frac{\Lambda}{3}, \tag{1.2}$$

$$\frac{\ddot{a}}{a} = -\frac{4\pi G}{3}\left(\rho + \frac{3p}{c^2}\right) + \frac{\Lambda}{3}. \tag{1.3}$$

These equations describe the dependence of the evolution of the Hubble parameter, $H \equiv \dot{a}/a$, on the stress-energy content of the universe, through the energy density and pressure contributions of the contents of the universe (ρ and p) and the cosmological constant, Λ.

From here on out, I make use the cosmological redshift as a line-of-sight parameter, defined as $z \equiv 1/a - 1$, which directly encodes the observed shift of the wavelengths of emitted light due to the metric expansion of space. The evolution of the expansion rate is conventionally denoted $H(z) = H_0 E(z)$, normalized to the observed local value of the Hubble constant, H_0, with the cosmological scaling contained in $E(z)$. The energy densities of the components of the universe are also normalized by the characteristic critical density of the universe,

$$\rho_c(z) = \frac{3H^2(z)}{8\pi G}. \tag{1.4}$$

In a flat universe, densities normalized by this critical density represent the fractional contribution of different components to the total energy density of the universe. I define three such relative densities based on their values at $z = 0$.

$$\Omega_{\rm M} \equiv \frac{\rho_{\rm M}(z=0)}{\rho_c(z=0)}, \quad \Omega_{\rm R} \equiv \frac{\rho_{\rm R}(z=0)}{\rho_c(z=0)}, \quad \Omega_\Lambda \equiv \frac{\rho_\Lambda(z=0)}{\rho_c(z=0)} = \frac{\Lambda}{3H_0^2}, \tag{1.5}$$

where $\rho_{\rm M}$ represents the energy density of matter (dark and baryonic) and $\rho_{\rm R}$ represents the energy density of radiation. These contributions scale differently with redshift due to

the varying effects of cosmological expansion on these physical quantities. The matter contribution scales as $\rho_{\rm M} \propto (1+z)^3$, the radiation contribution, $\rho_{\rm R} \propto (1+z)^4$, and the Λ contribution, ρ_Λ does not evolve with redshift.

As radiation is only a significant contribution to the energy density of the universe at very early times, it is neglected for the remainder of this section. Under these definitions, the cosmological scaling of the Hubble parameter simply becomes:

$$E(z) \equiv \sqrt{\Omega_{\rm M}(1+z)^3 + \Omega_\Lambda}. \tag{1.6}$$

In an expanding spacetime, concepts of distance become context dependent due to the time evolution of physical scales (as reviewed in Hogg, 1999). In this thesis I will make use of three distance definitions:

The comoving distance, $D_{\rm C}(z)$:

The distance obtained by integrating the differential, comoving distance contributions along the line-of-sight from the time of emission of the signal we're observing in the distant universe, t_e at redshift $z_{\rm e}$, to the present day at t_p corresponding to $z = 0$:

$$D_{\rm C}(z_{\rm e}) \equiv \int_{t_e}^{t_p} \frac{c\,{\rm d}t}{a(t)} = \frac{c}{H_0}\int_0^{z_{\rm e}} \frac{{\rm d}z}{E(z)}. \tag{1.7}$$

The luminosity distance, $D_{\rm L}(z)$:

This is the distance definition that preserves the inverse square law for the diminish-

ing flux, S, of a distant emitter at redshift z of physical luminosity L,

$$S = \frac{L}{4\pi D_{\rm L}^2(z)}. \tag{1.8}$$

In a flat universe,

$$D_{\rm L}(z) = (1+z)D_C(z). \tag{1.9}$$

The angular diameter distance, $D_{\rm A}(z)$:

This distance represents a quantity equivalent to the line-of-sight distance required in a Euclidean geometry to relate an observed angular separation, $\delta\theta$, to an equivalent transverse proper distance, δs through the relation

$$\delta s = D_{\rm A}(z)\delta\theta. \tag{1.10}$$

In a flat universe,

$$D_{\rm A}(z) = \frac{D_{\rm C}(z)}{1+z} = \frac{D_{\rm L}(z)}{(1+z)^2}. \tag{1.11}$$

When referencing the properties of dark matter halos, characteristic masses (and equivalently radii) will be conventionally described with reference to their average overdensity, Δ, with respect to the critical density of the universe at their redshift. That is,

$$M_\Delta = \frac{4}{3}\pi\Delta\rho_c(z)R_\Delta^3. \tag{1.12}$$

Typically values of $\Delta = 200$ or 500 are used. The average overdensity within which a halo is expected to be virialized corresponds to $\Delta_{\rm vir} \approx 200$.

Recent values obtained through a study of cosmic microwave background anisotropies with the *Planck* satellite, determined $\Omega_{\rm M} = 0.308 \pm 0.012,\ \Omega_\Lambda = 0.692 \pm 0.012$ and $H_0 = 67.8 \pm 0.9$ km s^{-1} Mpc^{-1} (Planck Collaboration et al., 2016a). For simplicity, throughout this work, a consistent set of cosmological parameter values will be used. These chosen values are $\Omega_{\rm M} = 0.30,\ \Omega_\Lambda = 0.7$ and $H_0 = 70h_{70}$ km s^{-1} Mpc^{-1}. For halo masses, the unit h^{-1} M$_\odot$ is occasionally used where, in the absence of a subscript, $h \equiv h_{100} = H_0/(100$ km s^{-1} Mpc$^{-1})$.

1.1.2 Formation of Large Scale Structure

In order to provide insight into the large scale environments within which structures form, I will outline the the behavior of large scale structure in the universe through the evolution of small density perturbations in the smooth, expanding background. For these purposes, I will start with linear order perturbations in the matter density field in the context of a cold dark matter (CDM) dominated cosmology (in this case, with zero curvature).

These matter perturbations will be denoted through the relative density contrast field $\delta(\vec{x},t)$, around the average matter density, $\overline{\rho_{\rm M}}$, such that,

$$\rho_{\rm M}(\vec{x},t) = \overline{\rho_{\rm M}}(t)(1+\delta(\vec{x},t)) \tag{1.13}$$

These perturbations are seeded by stochastic quantum fluctuations in the extremely early universe, expanded to larger scales through the process of inflation (Guth & Pi, 1982; Linde, 1982). As there was no characteristic length scale at the epoch at which they were generated, the spatial power spectrum of these initial perturbations (in terms of the density contrast field) are thought to be well described by a power law,

$$P(k) \propto k^{n_s}, \tag{1.14}$$

with strong theoretical arguments for $n_s \lesssim 1$ (the case $n_s = 1$ is known as the Harrison-Zel'dovich-Peebles spectrum).

Since the length scales of interest here are sufficiently smaller than the characteristic length scale of the universe $\sim c/H(z)$, the Newtonian theory of gravity is sufficient, and, since I am considering perturbations in a pressureless CDM fluid, the evolution of the matter density field is governed by the continuity equation,

$$\frac{\partial \rho}{\partial t} + \nabla \cdot (\vec{v}\rho) = 0, \tag{1.15}$$

for the conservation of mass, as well as the the pressureless Euler equation for a fluid in a gravitational potential ϕ,

$$\frac{\partial \vec{v}}{\partial t} + (\vec{v} \cdot \nabla)\vec{v} = -\nabla\phi, \tag{1.16}$$

where this potential must satisfy the Poisson equation,

$$\nabla^2\phi = 4\pi G\rho_{\rm M}. \tag{1.17}$$

The unperturbed solutions to these equations are, as expected from the Friedmann equations and Hubble law,

$$\overline{\rho_{\rm M}} = \overline{\rho_{\rm M,0}}/a^3 \quad \text{and} \quad \vec{v} = H\vec{x}. \tag{1.18}$$

By solving these equations for a small perturbation around these results, that is choosing,

$$\rho_{\rm M}(\vec{x},t) = \overline{\rho_{\rm M}}(1+\delta(\vec{x},t)), \tag{1.19}$$

and ignoring non-linear terms in the density contrast parameter, $\delta(\vec{x},t)$, the linear growth equation may be obtained,

$$\ddot{D} + \frac{2\dot{a}}{a}\dot{D} - 4\pi G\overline{\rho_{\rm M}}D = 0. \tag{1.20}$$

Here, $D(t)$ is the time-dependent term of the separable solution $\delta(\vec{x},t) = D(t)\delta(\vec{x})$, called the linear growth factor. This separability implies that the scale dependence of the distribution of matter density fluctuations is set at early times.

Hence, the power spectrum of linear perturbations grows as

$$P_{\rm lin}(k,t) \propto P_0(k)D^2(t), \tag{1.21}$$

However, $P_0(k)$ here is not simply the primordial power spectrum ($\propto k^{n_s}$) as, between the end of the inflationary epoch and the beginning of the matter dominated epoch, there was a period of radiation dominated expansion. In conjunction with the notion of the particle horizon from a fully relativistic treatment, that is the length scale beyond which physical interactions cannot occur, this period of radiation domination imparts an additional scale dependence on the seed power spectrum for the growth of structures (e.g., Dodelson, 2003; Schneider, 2006). Understanding the characteristic length scale thus imparted is particularly important for linking large scale structures observed in the late universe to the physical conditions in the early universe. Accounting for these effects, the power spectrum may be written in terms of a transfer function, $T(k)$ such that,

$$P_0(k) \propto k^{n_s} T^2(k). \tag{1.22}$$

In general, in the linear regime, this transfer function accounts for the fact that modes which entered the horizon during radiation domination suffer significant damping as the increased expansion rate in this epoch acts to suppress structure growth (the second term in Equation 1.20 dominates). Moreover, this damping is dependent on the relative scale factors of the universe when the mode entered the horizon and when radiation ceased to be the dominant component to the universal energy density. Approximately, in the limiting

regimes,

$$T(k) \propto \begin{cases} 1, & \text{if } k \ll 1/L_{\rm eq} \\ \\ k^{-2}, & \text{if } k \gg 1/L_{\rm eq}. \end{cases} \tag{1.23}$$

Here $L_{\rm eq}$ is the comoving horizon length scale characteristic of matter and radiation (energy density) equality. This scale is important as it encodes the approximate length scale of the peak in the spatial power spectrum of matter density fluctuations since, assuming $n_{\rm s} = 1$,

$$P(k) \propto \begin{cases} k, & \text{if } k \ll 1/L_{\rm eq} \\ \\ k^{-3}, & \text{if } k \gg 1/L_{\rm eq}, \end{cases} \tag{1.24}$$

where the damping of small scales is encoded by the k^{-3} decline in the power spectrum. In a ΛCDM universe (e.g. Voit, 2005),

$$L_{\rm eq} \approx \frac{c}{H(z_{\rm eq})} \sim 100 \text{ Mpc}. \tag{1.25}$$

If a large overdensity is able to form in a localized region, it will break away from the linear evolution and collapse into a non-linear structure. Some insights into this process can be obtained from only linear considerations (e.g., Peebles, 1980; Voit, 2005). In particular, the mass perturbation in a localized region of radius r can be determined by smoothing the matter density fluctation field $\delta(\vec{x})$ with a tophat window function of radius r, W_r,

$$\sigma_r(\vec{x}) = \frac{\delta M_r}{M_r}(\vec{x}) = \int \delta(\vec{x'}) W_r(|\vec{x'} - \vec{x}|)\, {\rm d}^3x'. \tag{1.26}$$

Noting that the variance of this quantity may be related to the power spectrum,

$$\left\langle \left| \frac{\delta M_r}{M_r} \right|^2 \right\rangle = \sigma_r^2 = \frac{1}{(2\pi)^3} \int P(k) |W_{k_r}(k)|^2 \, \mathrm{d}^3 k, \tag{1.27}$$

yields, for $P(k) \propto k^n$ a smoothed variance of $\sigma_r^2 \propto k_r^{n+3}$. Therefore the typical smoothed overdensity fluctation $|\delta M_r / M_r|$ is proportional to $k_r^{(n+3)/2}$ where, from Equation 1.24, $n = 1$ for $k \ll 1/L_{\mathrm{eq}}$ and $n = -3$ for $k \gg 1/L_{\mathrm{eq}}$. Additionally, the mass within a spherical region M_r is proportional to $r^3 \propto k_r^{-3}$. Then, in the two limiting cases for the matter density fluctuation power spectrum,

$$\left| \frac{\delta M_r}{M_r} \right| \propto \begin{cases} M_r^{-2/3}, & \text{if } k_r \ll 1/L_{\mathrm{eq}} \quad (\text{high } M_r) \\ 1, & \text{if } k_r \gg 1/L_{\mathrm{eq}} \quad (\text{low } M_r). \end{cases} \tag{1.28}$$

Simple models of spherical collapse find that, when $|\delta M_r / M_r|$ reaches a critical threshold, the region of radius r will decouple from linear expansion and rapidly grow non-linearly. From these simple arguments, we therefore see that, inhomogeneities on small scales, $k_r \gg 1/L_{\mathrm{eq}}$, corresponding to low masses, collapse earlier than those on large scales, $k_r \ll 1/L_{\mathrm{eq}}$, corresponding to high masses, and, therefore structure formation in this cosmological background takes place hierarchically. That is, the collapse of structures above a certain mass scale is suppressed relative to masses below that scale. This is consistent with what is seen in numerical n-body simulations as discussed in Section 1.1.3. Some further considerations additionally allow approximate forms for the abundance of collapsed halos

as a function of mass to be constructed (Press & Schechter, 1974).

I also note here that the matter power spectrum is typically normalized through the same variance expressed here, generally through the quantity σ_8 corresponding to a tophat smoothing scale of comoving radius 8 h^{-1} Mpc.

1.1.3 Non-Linear Structure Formation

Formulations for the spherical collapse of overdense regions in a cosmological background have been explored (e.g., Kaiser, 1986; Lacey & Cole, 1993; Peebles, 1980), finding that overdensities, after passing a critical, cosmology-dependent, threshold ($\delta_c = 1.69$ for a flat, $\Omega_{\rm M} = 1$, universe), rapidly collapse and relax into a virialized halo. Bryan & Norman (1998) show that the average overdensity of such a collapsed region (with respect to $\rho_c(z)$) can be numerically approximated by,

$$\Delta_c = 18\pi^2 + 82(\Omega_{\rm M}(z) - 1) - 39(\Omega_{\rm M}(z) - 1)^2, \tag{1.29}$$

leading to the commonly used mass definition of M_Δ with $\Delta = 200$, when discussing an approximately fully virialized region of a dark matter halo.

While the linear treatment of small perturbations in a the matter density field may be analytically evaluated, and simple models for non-linear collapse have been widely explored, in practice much of our modern understanding of these processes come from large n-body simulations. These simulations have reached particle counts of 10^{10} (Illustris, Vo-

gelsberger et al., 2014) and volumes of $(7200\ h^{-1}\ \mathrm{Gpc})^3$ (New Horizon, Kim et al., 2011). They are found to reproduce similar overarching features to those apparent from theoretical considerations. That being that structure formation is hierarchical, with the smallest structures collapsing first and the largest structures arising from a complicated history of mergers over many billions of years. Additionally, these simulations have provided much more precise insight into the statistical properties of dark matter halos and the coevolution of dark matter and galaxies.

By measuring the abundance of halos in such simulations, well-calibrated mass functions have been determined. For example, Tinker et al. (2008), constrain, to within 5%, the abundances of 10^{11}–$10^{15}\ h^{-1}\mathrm{M}_\odot$ dark matter halos and the evolution of these abundances from $z = 2.5$ to $z = 0$. These calibrated relations for the abundance of halos have allowed us to infer cosmological constraints from observed abundances in surveys of, for example, galaxy clusters.

In addition, simulations have yielded insights into the remarkable consistency of the radial distribution of dark matter in collapsed halos. With the Navarro-Frenk-White (NFW, Navarro et al., 1996) profile,

$$\rho_{\mathrm{DM}}(R) \propto \frac{1}{x(1+x)^2}, \tag{1.30}$$

determined to be well fit by by simulated halos and widely prevalent in the literature. Here $x \equiv R/R_{\mathrm{s}}$, where $R_s = cR_{\mathrm{vir}}$. Similarly the evolution and mass dependence of halo concentration, expressed with respect to different average density contrasts, Δ, through $c_\Delta = R_\Delta/R_{\mathrm{s}}$, has been well established through simulation based approaches (e.g., Duffy

et al., 2008).

1.2 Gravitationally Supported Ionized Gas

While, in the above, we consider the gravitational collapse of overdense regions in terms of the distribution of their dark matter components, there is also a large ($\lesssim$20% by mass in galaxy clusters) baryonic component present. This luminous component is gravitationally shock heated during infall, and is extremely energetic, reaching large temperatures of $\sim 10^8$ K corresponding to energy scales on the order of $\lesssim$10 keV for 10^{15} $M_\odot$ systems. As such it is highly ionized and able to radiatively cool via thermal bremsstrahlung. Massive halos containing this hot, ionized, gas, such as galaxy clusters, are powerful sources of X-ray emission due to this thermal radiation.

While the processes which can effect the distribution of this gas may be complicated, under the assumption that gravitation plays a dominant role (as should be the case for the most massive systems) and, if no characteristic scale is introduced during collapse, we can derive self-similar expectations for its thermodynamic properties. These expectations originate from assuming this gas is in virial equilibrium with the gravitational potential of its dark matter halo. Under this consideration, the average per-particle kinetic energy can be related to the gravitational potential energy,

$$\langle E_{\rm k} \rangle = -\frac{1}{2} \langle E_{\rm p} \rangle. \tag{1.31}$$

Making use of a kinetic temperature, this defines the relationship between the self-similar characteristic gas temperature T_Δ corresponding to a halo mass M_Δ (e.g., Kaiser, 1986; Nagai et al., 2007a; Voit, 2005),

$$\begin{aligned}\frac{3}{2}k_{\rm B}T_\Delta &= \frac{\mu m_{\rm p} G M_\Delta}{2R_\Delta} \\ &= \frac{\mu m_{\rm p}}{3} G^{2/3} \left(\frac{\Delta H^2(z)}{2}\right)^{1/3} M_\Delta^{2/3} \\ &= 0.73\,{\rm keV}\ \Delta^{1/3} \left(\frac{M_\Delta}{10^{15}\,{\rm M}_\odot}\right)^{2/3} (h_{70}E(z))^{2/3}\end{aligned} \tag{1.32}$$

where μ is the mean molecular weight per ion, chosen to be 0.59 in the last line of this equation. Here Equations 1.12 and 1.4 have been used in the first step. A typical choice of $\Delta = 500$ is common for X-ray and SZ studies.

This characteristic electron temperature can be used to define a characteristic electron pressure, $P_{\rm e,\Delta} = n_{\rm e,\Delta} k_{\rm B} T_\Delta$ where the electron number density, $n_{\rm e}$ is assumed to depend on the cosmic baryon fraction $f_{\rm B} \equiv \Omega_{\rm B}/\Omega_{\rm M}$ such that,

$$\begin{aligned}n_{\rm e,\Delta} &= \frac{f_{\rm B}\Delta\rho_c(z)}{\mu_{\rm e} m_{\rm p}} \\ &= \frac{3}{8\pi}\frac{f_{\rm B}\Delta H^2(z)}{G\mu_{\rm e} m_{\rm p}},\end{aligned} \tag{1.33}$$

where $\mu_{\rm e}$ is the mean molecular weight per free electron, which is assumed to take the

value 1.14 here. Again, making use of Equation 1.4, the characteristic pressure is,

$$\begin{aligned} P_{\mathrm{e},\Delta} &= \frac{f_{\mathrm{B}}}{8\pi}\frac{\mu}{\mu_{\mathrm{e}}}\frac{\Delta^{2/3}H^{8/3}(z)}{(2G)^{1/3}}M_{\Delta}^{2/3} \\ &= 3.4\times10^{-6}\,\mathrm{keVcm^{-3}}\;\Delta^{4/3}\left(\frac{M_{\Delta}}{10^{15}\,\mathrm{M_{\odot}}}\right)^{2/3}\;(h_{70}E(z))^{8/3}, \end{aligned} \tag{1.34}$$

using 0.175 for the fiducial value of f_{B}. In practice, the precise value of the numerical terms, f_{B}, μ and μ_{e}, are not important as long as they are used consistently, so the adopted values here are chosen to be the same as those of Nagai et al. (2007b).

Both observations (e.g., Arnaud et al., 2001, 2010; Planck Collaboration et al., 2013a; Sun et al., 2011; Vikhlinin et al., 2006) and hydrodynamic simulations (e.g., Battaglia et al., 2012, 2010; Dolag et al., 2005; Trac et al., 2011) of the hot gas associated with galaxy clusters of masses $\gtrsim 10^{14}\,\mathrm{M_{\odot}}$ have found remarkable agreement in the radial profiles and integrated measures of gas thermodynamic properties (density, pressure and entropy) when rescaled to self-similar quantities such as those outlined above.

1.2.1 The Role of Feedback and Non-gravitational Effects

The agreement of self-similar scalings with observations implies that the ionized gas in dark matter halos, at least for the most massive objects, is gravitationally dominated. However, self-similar scaling with mass has long been known to break down in the cores of galaxy clusters (Kaiser, 1991). This is indicative of the broad influence of non-gravitational effects on this otherwise gravitationally stratified gas. This influence may be probed through

deviations in the shape or normalization of self-similarly scaled observations.

Such non-gravitational effects include the feedback processes which are of great importance in bringing observations of galaxy counts in line with galaxy formation models (e.g., Croton et al., 2006). Nominal expectations for such models typically have difficulty reproducing the galaxy luminosity function, on both the faint and bright ends. Additionally, the formation of galaxies appears to be an anti-hierarchical process, with a substantial population of galaxies hosting large stellar populations at $z \gtrsim 1$ and an observed decrease in the star formation rate at low redshift (Bower et al., 2006; Cowie et al., 1996; Madau et al., 1998). This is in contrast to the hierarchical manner in which dark matter halos collapse. Both of these related problems may be reconciled by invoking some degree of energetic feedback. Such processes provide a reheating or redistribution of the halo gas, cutting off the fuel of star formation, ideally in a self-regulating fashion (e.g., Hopkins et al., 2006). Such self-regulation could be realized by energetic feedback related to processes associated with star formation or accretion onto supermassive black holes. These reheating effects are analogous to the reheating of the gas at the cores of galaxy clusters, sustaining them against catastrophic cooling, and are likely closely related (e.g., Rawlings & Jarvis, 2004; Scannapieco & Oh, 2004). Indeed the influence of active galactic nuclei (AGN) feedback has been directly observed in the ICM through the low density cavities in this medium seen to coincide with AGN jets in some systems (e.g. Fabian et al., 2000; McNamara et al., 2000; Vantyghem et al., 2014).

While such effects have been directly observed in galaxy clusters, they should be even

more important in low mass systems whose gravitational potentials are less energetically dominant. Therefore probing the thermodynamics of ionized plasma in extragalactic structures over a broad range of masses can constrain the energetics of the feedback processes relevant to galaxy formation.

1.3 Cosmic Microwave Background Anisotropies

The Cosmic Microwave Background (CMB) is the relic radiation of the big bang. This radiation field was emitted in the early universe, once the primordial plasma cooled sufficiently (through cosmic expansion) for photons to decouple from matter and stream freely through the universe. This occurred shortly after the recombination epoch where the first atoms formed and the universe was approximately 400,000 year old. This thermal radiation is the oldest light we are able to observe today, creating the so-called surface of last scattering, beyond which the universe appears opaque from our perspective. The CMB is observed today as a nearly isotropic blackbody radiation field with a temperature of 2.72548 ± 0.00057 K (Fixsen, 2009). However, spatial fluctuations of the order of $\Delta T / T_{\rm CMB} \sim 10^5$ in this radiation provide some of the most powerful constraints on cosmological parameters (see e.g. Hu & Dodelson, 2002). While these constraints are derived from CMB fluctuations of primordial origin, late-time anisotropies induced in this observed radiation field can also be powerful observational tools.

One such secondary anisoptropy, the Sunyaev-Zel'dovich effect (SZ Sunyaev & Zel-

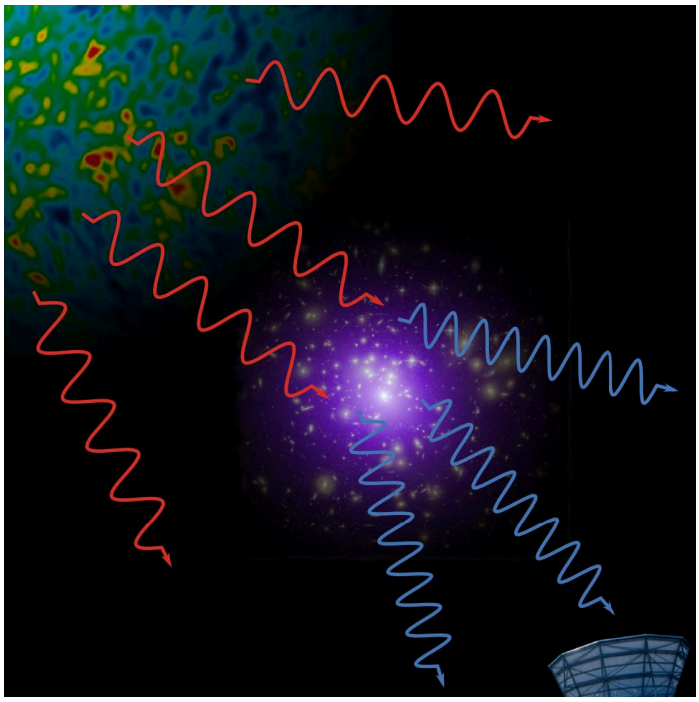

Figure 1.1: Schematic illustration of the Sunyaev-Zel'dovich Effect. CMB photons propagate from the surface of last scattering before interacting with intervening ionized gas (here, shown hosted by a galaxy cluster (Image credit: NASA/CXC/MIT; Optical: NASA/STScI)) before being observed.

dovich, 1980, 1970) refers to the inverse Compton scattering of CMB photons by ionized plasma along the line-of-sight. Figure 1.1 shows a schematic illustration of this. Two manifestations of this effect are described below.

1.3.1 The Thermal Sunyaev-Zel'dovich Effect

When CMB photons scatter off a sufficiently high temperature plasma, hot, thermalized electrons will impart some of their thermal energy on the scattered photons, subtly shifting the spectral energy distribution of the CMB. This is known as the thermal Sunyzaev-Zel'dovich (tSZ) effect. The amplitude of this distortion is parameterized through the

Compton-y parameter (Birkinshaw, 1999; Carlstrom et al., 2002; Rephaeli, 1995):

$$\frac{\Delta I_\nu}{I_{\nu,\mathrm{CMB}}} = y g(\nu), \quad y \equiv \frac{\sigma_\mathrm{T}}{m_\mathrm{e} c^2} \int n_\mathrm{e} T_\mathrm{e} \, \mathrm{d}l, \tag{1.35}$$

Here σ_T is the Thomson scattering cross-section, and m_e, n_e and T_e are the electron mass, number density and temperature, respectively. The integral is taken along the line-of-sight, l. The spectral distortion function, $g(\nu)$, for a non-relativistic population of electrons, takes the form,

$$g\left(x \equiv h\nu / k_\mathrm{B} T_\mathrm{CMB}\right) = \frac{x^4 \mathrm{e}^x}{(\mathrm{e}^x - 1)^2} \left(x \frac{\mathrm{e}^x + 1}{\mathrm{e}^x - 1} - 4 \right). \tag{1.36}$$

The shape of this spectral distortion is shown in Figure 1.2. As seen in Equation 1.35, the CMB spectral intensity $I_{\nu,\mathrm{CMB}}$ suffers a relative shift, ΔI_ν due to this effect. Observations of CMB anisotropies, such as those provided by CMB observatories, are typically referenced to the fiducial CMB blackbody intensity, therefore, the spectral intensity of the SZ signal observed by these experiments takes the form of $g(\nu)$. Uniquely, this predicts an observed decrement (negative signal) from this effect at frequencies below 220 GHz as can be seen in Figure 1.2.

A notable property of this effect, is that, unlike emission processes, its surface brightness does not suffer from cosmological redshift dimming. This makes the tSZ effect a powerful probe of the distant universe.

As shown in Eq. 1.35, the amplitude of the tSZ effect depends on the integral of the electron thermal pressure $P_\mathrm{e} = n_\mathrm{e} T_\mathrm{e}$ along the line-of-sight. If we measure the total inte-

grated SZ amplitude across the solid angle that the object we are observing subtends, we find,

$$Y \equiv \int y d\Omega \propto \frac{P_{\rm e}\,{\rm d}V}{D_{\rm A}^2(z)}. \tag{1.37}$$

That is, this integrated SZ amplitude, Y, is proportional to the total integrated thermal electron pressure over the entire volume of the ionized plasma being observed. This can be directly related to the total thermal energy of the plasma,

$$E_{\rm th} = \frac{3}{2}\left(1+\frac{1}{\mu_{\rm e}}\right)\int P_{\rm e}\,{\rm d}V, \tag{1.38}$$

where $\mu_{\rm e}$ is the mean molecular weight per free electron. This fact makes the tSZ effect an extremely useful probe of the thermal energy of ionized gas in cosmic structures.

In addition, it follows from Equation 1.37, and the discussion in Section 1.2, that there is a characteristic self-similar scaling relation for the volume integrated tSZ amplitude,

$$Y_\Delta = \frac{\sigma_{\rm T}}{m_{\rm e}c^2} P_{{\rm e},\Delta} \frac{4\pi}{3} R_\Delta^3 \tag{1.39}$$

$$= 3.5\times10^{-5}\,{\rm Mpc}^2\;\Delta^{1/3}\left(\frac{M_\Delta}{10^{15}\,{\rm M}_\odot}\right)^{5/3}\;(h_{70}E(z))^{2/3}. \tag{1.40}$$

This relationship, the self-similar expectation for the so-called Y-M relation, makes the tSZ effect particularly useful for cosmology since the amplitude of the observed signal can be related to the mass of the systems under observation. Using a given set of cosmological

parameters, one can theoretically predict the expected distribution of gravitational halos in both mass and redshift. By utilizing the tSZ effect we can observationally constrain this distribution and, consequently, make inferences on cosmological parameters, in particular the relative matter energy density, $\Omega_{\rm M}$ and the amplitude of the matter fluctuation power spectrum σ_8 (e.g. Birkinshaw, 1999; Carlstrom et al., 2002).

However, there are additional effects that break the simple hydrostatic derivation presented above, such as those outlined in Section 1.2.1. Systematic effects, generally attributed to poorly constrained deviations from self-similarity due to feedback processes and non-thermal pressure contributions, are currently restricting the utility of cosmological studies based on tSZ observations. While large tSZ galaxy cluster surveys from the Atacama Cosmology Telescope (ACT, Hasselfield et al., 2013b), the *Planck* Satellite (Planck Collaboration et al., 2016d) and the South Pole Telescope (SPT, de Haan et al., 2016) provide powerful cosmological probes, their utility is limited by these systematic concerns.

1.3.2 The Kinetic Sunyaev-Zel'dovich Effect

There is an additional Sunyaev-Zel'dovich effect describing the transfer of the bulk kinetic energy of the ionized gas to the CMB photons. This is known as the kinetic Sunyaev-Zel'dovich (kSZ) effect. The observed amplitude of this effect depends on the bulk line-of-sight velocity of the ionized gas, $v_{\rm e}$ producing an observed fluctuation in CMB temperature,

$$\frac{\Delta T}{T_{\rm CMB}} = -\tau_{\rm e}\frac{v_{\rm e}}{c}. \tag{1.41}$$

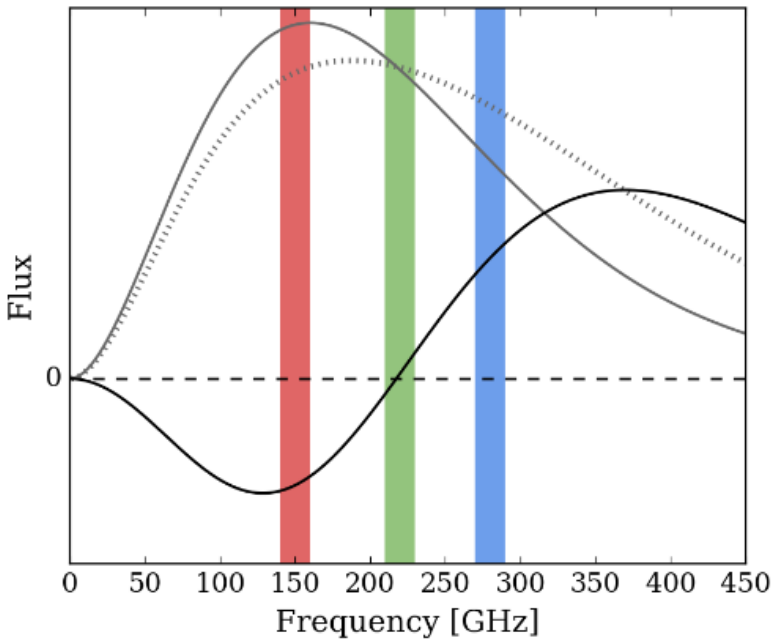

Figure 1.2: The spectral distortion of the thermal Sunyaev-Zel'dovich effect (tSZ) on the CMB spectrum. In arbitrary units, the intensity of the CMB blackbody radiation as a function of observed frequency is shown in the solid gray line. An exaggerated distortion of this spectrum, due to the tSZ effect, is shown in the dotted gray line. The solid black curve represents the relative difference between the distorted and undistorted spectrum, the spectral feature the tSZ effect imparts on CMB observations. As can be seen, a negative signal is predicted below 220 GHz and a positive signal is predicted above 220 GHz. The 148, 218 and 277 GHz ACT MBAC bands are overlayed in red, green and blue, respectively.

Note that, unlike the thermal SZ effect, the spectral shape of this signal is identical to that of the CMB, making it difficult to observe over the primary CMB anisotropies. The kSZ was first observed statistically using data from the Atacama Cosmology Telescope (Hand et al., 2012) and promises to be a compelling probe of large-scale baryonic physics and the cosmological velocity field (e.g. Ferraro et al., 2016). In this work, however, I will focus only on the tSZ effect.

1.4 The Atacama Cosmology Telescope

The Atacama Cosmology Telescope (ACT, Fowler et al., 2007; Swetz et al., 2011) is a 6 meter millimeter-wave telescope located at an altitude of 5,200 meters above sea level in the high and dry site of the Atacama Desert in Chile. ACT's large-diameter primary mirror and sensitive detector arrays enable it to conduct large surveys of the millimeter sky at arcminute resolution. Since commissioning in 2007, ACT has conducted a series of large surveys spanning 1000s of square degrees. In 2007–2013, with its initial detector array complement, the Millimeter Bolometer Array Camera (MBAC, Swetz et al., 2011), ACT conducted a southern and an equatorial survey in three frequency bands centered at 148, 218 and 277 GHz. These bands were selected for the availability of atmospheric windows and their suitability for studying the CMB, the SZ effect and high redshift thermal dust emission. Figure 1.2 shows how these bands span the tSZ distortion spectrum.

In this work we make use of the original set of ACT surveys conducted with MBAC.

Table 1.1: ACT and *Herschel*-SPIRE survey characteristics and associated calibration uncertainties

	ACT			*Herschel*-SPIRE		
Band	148 GHz	218 GHz	277 GHz	600 GHz	857 GHz	1200 GHz
Beam FWHM	1.4 arcmin	1.0 arcmin	0.9 arcmin	0.6 arcmin	0.4 arcmin	0.3 arcmin
Typical RMS noise (mJy beam^{-1})	2.2	3.3	6.5	13.3[c]	12.9[c]	14.8[c]
Flux calibration uncertainty (percent)	3[a]	5[a]	15	7[b]	7[b]	7[b]

[a] A correlated component to the calibration uncertainty of 3 percent between the ACT 148 and 218 GHz bands is also accounted for.

[b] The calibration uncertainty of the *Herschel*-SPIRE data includes a 5 percent component correlated across all three bands.

[c] Here we list the relevant values for the *Herschel*-SPIRE HerS survey. For the HeLMS survey data used in Chapter 2, RMS noise levels are comparable as confusion noise from the CIB is the most significant contributor.

These surveys consist of a southern ($20^{\rm h}43^{\rm m} <$ R.A. $< 7^{\rm h}53^{\rm m}$, $-57^\circ <$ Dec. $< -48^\circ$) and equatorial ($21^{\rm h}20^{\rm m} <$ R.A. $< 3^{\rm h}52^{\rm m}$, $2.^\circ 12 <$ Dec. $< 2.^\circ 34$) strip covering areas of approximately 850 and 450 square degrees respectively.

The data processing methodologies, calibration and beam characterization for these data are described in Dünner et al. (2013), Hajian et al. (2011) and Hasselfield et al. (2013a), respectively. The manner in which the ACT maps are calibrated induces some correlated uncertainty in flux measurements between bands (See discussion in Gralla & Crichton et al. (2014)). This correlated uncertainty is accounted for in the modeling in Chapters 2 and 3. The resulting uncertainties are summarized in Table 1.1. For this work we use the point source matched filtered ACT data which optimally recovers the flux of point sources while filtering out large scale emission from the CMB and atmosphere. The matched filter methodology is described in Marriage et al. (2011a). Figure 1.3 shows an example patch of matched filtered 148 GHz ACT data.

In 2013 a new set of polarization sensitive detectors were commissioned (ACTPol, Niemack et al., 2010; Thornton et al., 2016). Currently the next generation of ACT detectors are undergoing deployment, comprising Advanced ACTPol (Henderson et al., 2016).

1.5 Large Herschel-SPIRE Surveys

The *Herschel Space Observatory* Spectral and Photometric Imaging REceiver (*Herschel*-SPIRE) observed at frequencies of 600, 857 and 1200 GHz (Griffin et al., 2010).

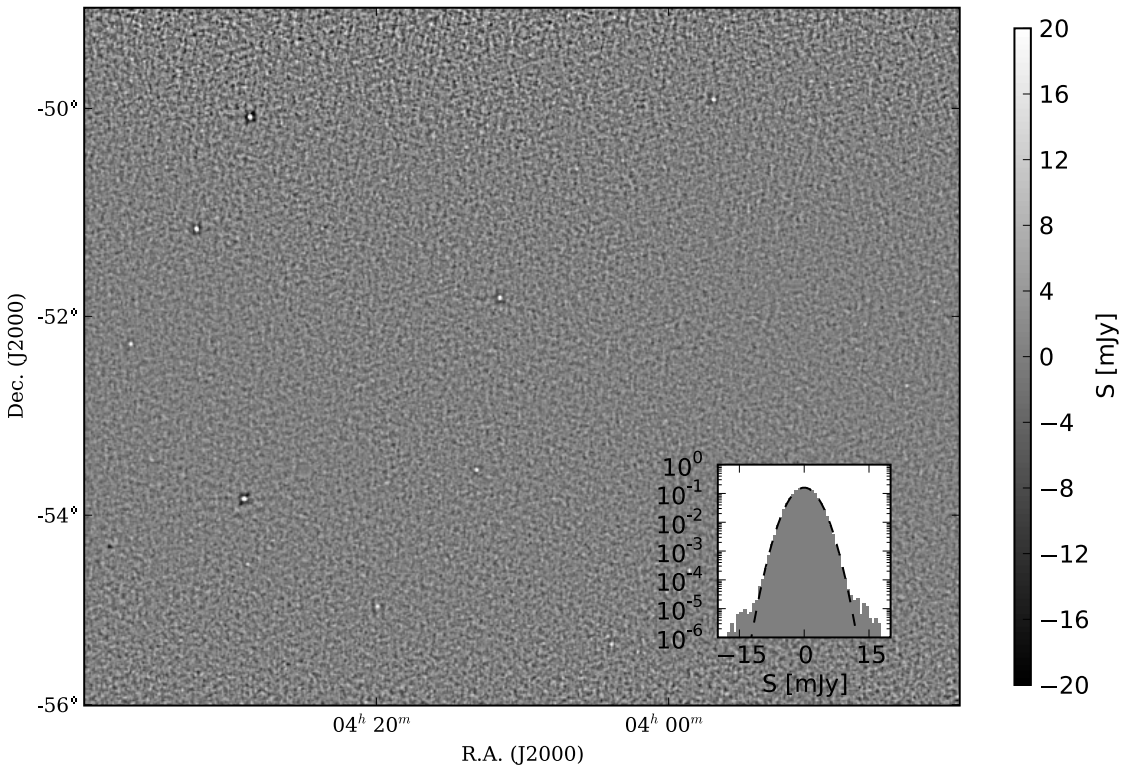

Figure 1.3: An extracted submap of point-source matched-filtered 148 GHz ACT data from the southern survey as presented in Marriage et al. (2011a). Several sources are evident in their positive emission in this map. The inset plot shows a histogram of the pixels in mJy, demonstrating the approximately Gaussian noise properties of maps filtered this way, with the outliers corresponding to detected sources.

These bands make *Herschel*-SPIRE ideally suited for extragalactic science as they are sensitive to dusty emission in galaxies at high redshift.

For the work in this thesis, we make use of the *Herschel*-SPIRE data from the publicly available *Herschel* Stripe 82 survey (HerS; Viero et al., 2014)[1] and the HerMES Large-Mode Survey (HeLMS), which is an element of the Herschel Multi-Tiered Extragalactic Survey (HerMES[2]; Oliver et al., 2012). HerS covers 70 square degrees overlapping the celestial equator ($02^{\rm h}25^{\rm m} <$ R.A. $< 00^{\rm h}45^{\rm h}$, $-2^\circ <$ Dec. $< 2^\circ$) while HeLMS is made up of a 270 square degree area partially covering the region spanning $23^{\rm h}45^{\rm m} <$ R.A. $< 01^{\rm h}15^{\rm m}$, $-8^\circ <$ Dec. $< 8^\circ$. Figure 1.4 shows the data from these surveys overlayed with the location of the ACT equatorial region.

The properties of the *Herschel*-SPIRE data used here are listed in Table 1.1. The SPIRE flux calibration uncertainty and beam full width at half-maximum (FWHM) are derived from observations of Neptune (Griffin et al., 2013). A significant fraction of the typical RMS noise values for *Herschel*-SPIRE flux recovery, as quoted in Table 1.1, originates from confusion noise from the CIB of the order of 8 mJy beam^{-1} (Viero et al., 2014).

1.6 Planck Compton-y Map

The *Planck* collaboration have constructed all sky estimates of the Compon-y signal from the tSZ effect (Planck Collaboration et al., 2016b). For the work presented in this

[1] http://www.astro.caltech.edu/hers/HerS_Home.html
[2] http://irsa.ipac.caltech.edu/data/Herschel/HerMES/

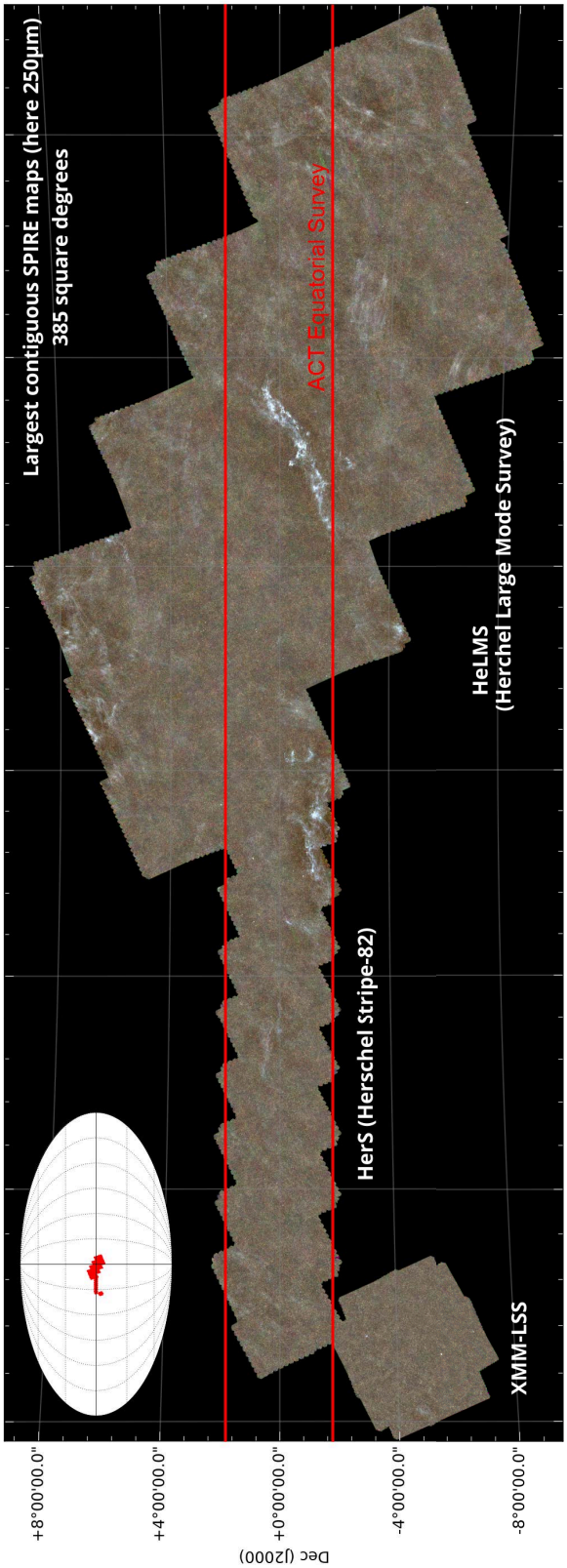

Figure 1.4: Three band RGB images of the large *Herschel*-SPIRE surveys on the equator, (Oliver et al., 2012, image adapted from `http://hedam.oamp.fr/HerMES/img/helms_hers_xmm-lss.png`). Shown here are the HerMES HeLMS survey and the HerS survey. Overlayed is the red outline of a region representing the coverage of the ACT equatorial strip in this region.

thesis, we make use of a version of this map extracted using the Modified Internal Linear Combination Algorithm (MILCA, Hurier et al., 2013). Through this process, different contributing components — the SZ Compton-y signal, the CMB and emission from the infrared sources making up the Cosmic Infrared Background (CIB) — are separated out. The resulting map is optimized such that the variance in the output Compton-y map is minimized after removing the other components using the specific frequency dependence of each contribution. We use maps constructed using the MILCA algorithm from the *Planck* high frequency instrument (HFI) spanning frequencies from 100–857 GHz, smoothed to a common angular resolution of $7'$. This algorithm specifically accounts for the spatial localization of the different contributing components, which is important for estimating the tSZ signal that originates from discrete sources on the sky (typically galaxy clusters). This is in contrast to methods aiming to separate out a spatially uniform signal, such as the CMB, where spatial localization is not as important.

Chapter 2

The SZ Effect Associated with Radio-loud AGN

A particularly powerful mechanism by which AGN are able to influence their surroundings, with a history of direct observations, is the process of radiatively inefficient accretion which is thought to power so-called "radio mode" AGN feedback. This accretion, which shares and interacts with the same gas reservoir from which stars potentially form, is therefore an important feedback contribution in galaxy formation models. A review of observations of such AGN to gas interactions can be found in McNamara & Nulsen (2007). In particular cavities or bubbles (e.g. Figure 2.1) excised by the powerful mechanical feedback such systems are able to provide, is observed in the X-ray halos of nearby galaxy clusters (e.g. Fabian et al., 2000; McNamara et al., 2000; Vantyghem et al., 2014). This evidence, as observed in the ionized intracluster medium, is seen to coincide with radio

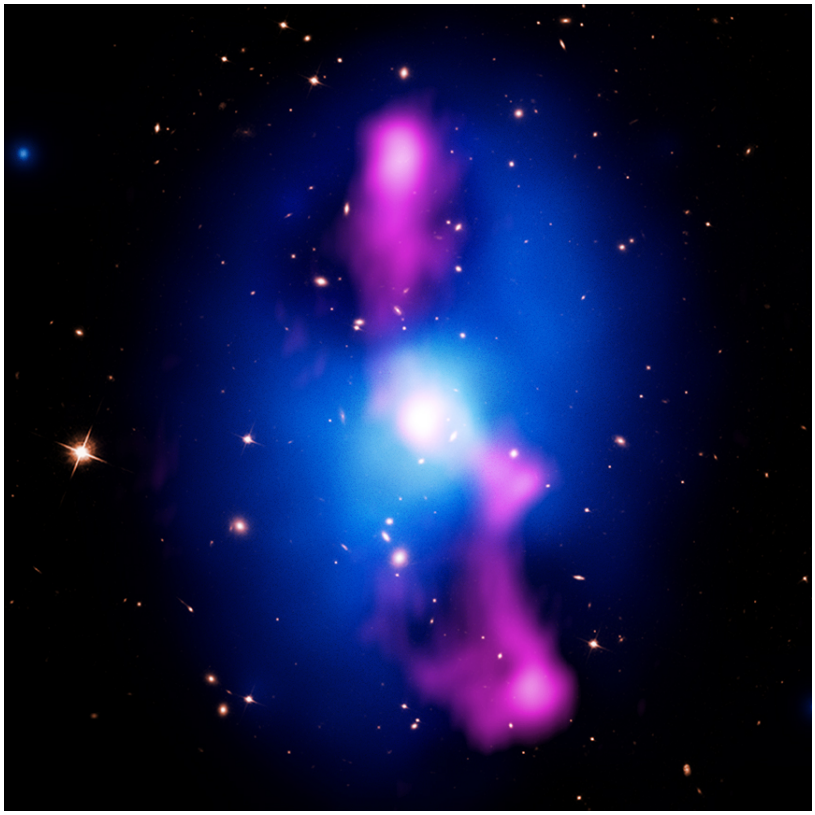

Figure 2.1: Cavities in the observed in the X-ray emission (blue) of the galaxy cluster MS 0735.6+7421. These cavities are clearly associated with the AGN driven jets observed in the VLA radio emission shown in pink. The member galaxies are shown in the optical as observed with *Hubble* are also shown. (Image credit: X-ray: NASA/CXC/Univ. of Waterloo/Vantyghem et al. (2014); Optical: NASA/STScI; Radio: NRAO/VLA)

emission apparently originating from AGN driven jets within the central galaxies of these objects.

However, in more typical radio mode AGN hosts, such effects are likely present but more difficult to observe. Direct observations, such as those described above, are restricted to dozens of systems, typically at $z \sim 0.5$ as required to make detailed X-ray observations (e.g. Ineson et al., 2013). However, much of the radio galaxy population, with catalogs selected at 1.4 GHz with flux densities above 1 mJy, span a wide range of redshift with typical median values of $z \sim 1$ (Condon, 1989). Therefore, in order to study the general population of environments of AGN exhibiting radio-mode feedback, a different approach is required. In this study we attempt to constrain the average thermal energy of the hot ionized gas associated with the hosts of these systems using the Sunyaev-Zel'dovich effect. This signal, which does not suffer from the same surface brightness dimming effects of e.g. X-ray emission, allows us to probe the thermodynamic state of the ionized gas around radio galaxies over a statistical sample of radio selected sources over the entire redshift range they cover. The work described here is published in Gralla & Crichton et al. (2014).

Care has been taken to model the emission associated with these systems which is significant in the bands of interest. This emission is dominated by synchrotron which may vary significantly from source to source (de Zotti et al., 2010; Lin et al., 2009; Sadler et al., 2006; Sajina et al., 2011). Generally models characterize the synchrotron spectral behavior of these sources into two types: steep-spectrum and flat-spectrum sources, corresponding to $\alpha \gtrsim 0.8$ and $\alpha \sim 0$ respectively, where α is the synchrotron spectral index defined such

that flux density $S \propto \nu^{-\alpha}$. Optically thin synchrotron emission, usually generally associated with extended radio lobes, results in a steep spectrum. Conversely, optically thick emission, typically associated with compact cores, produces a flattened spectrum source (e.g., de Zotti et al., 2010, for a review).

To constrain the millimeter emission and SZ contribution to the average SEDs of these systems, we stack 148, 218 and 277 GHz observations from the Atacama Cosmology Telescope (ACT) at the locations of radio sources sources drawn from the catalog of Kimball & Ivezić (2008). This dataset is constructed from Faint Images of the Radio Sky at Twenty-Centimeters (FIRST) and NRAO VLA Sky Survey (NVSS) catalogs cross-matched with one another. We additionally make use of Parkes and the Green Bank Telescope data at 4.8 GHz and far-infrared data from surveys conducted by *Herschel*-SPIRE to constrain these models. Through this modeling, we are able to constrain the average synchrotron spectral behaviour and it's evolution as a function of observed source flux. Additionally, we find a robust 5σ detection of the SZ contribution to the millimeter SEDs of these sources which had previously been undetected.

2.1 The Radio-loud AGN Catalog

For this study, we use a large sample of radio galaxies from two radio surveys. The Faint Images of the Radio Sky at Twenty-Centimeters (FIRST Becker et al., 1995; White et al., 1997) survey produced a map of over 10 000 deg^2 of the sky at 1.4 GHz (20 cm)

through the period of 1993 to 2004 using the Very Large Array (VLA). These data have an imaging resolution of $5''$ and an accurate astrometric resolution of $1''$. This survey produced a catalog of radio sources down to limiting flux densities ranging from 0.75 mJy to 1 mJy in its equatorial region (which overlaps with ACT's equatorial survey).

Additionally, we utilize the National Radio Astronomy Observatory (NRAO) VLA Sky Survey (NVSS; Condon, 1989), a separate, shallower survey also conducted at 1.4 GHz which covers the full Northern sky (above -40° declination) with a limiting flux density of $\sim$2.5 mJy and a lower (when compared to FIRST), $45''$, imaging resolution.

To fully make use of the different properties of these sensitive radio surveys, we choose a sample drawn from a cross-matched catalog, combining these two datasets. The catalog[1] of Kimball & Ivezić (2008) provides such a cross-matched dataset. We use all FIRST detections from this catalog within the ACT equatorial survey region (See Section 1.4) that have at least one NVSS source matched (within $30''$) to them. In the case of multiple matches, we choose the highest ranked (per the algorithm outlined in Kimball & Ivezić (2008)) cross-match. By using a combined catalog, we both cut down on the possibility of false sources (such as false positives due to beam sidelobes) and are able to make use of the respective strengths of each catalog. We use the high astrometric precision of the FIRST source locations to define the source locations on which the stacking procedure is applied while using the NVSS source fluxes in our modeling. This allows us to make use of the larger $45''$ FWHM NVSS beam which is less subject to bias due to resolving out the flux

[1] `http://www.cv.nrao.edu/~akimball/radiocat/`

density of sources extended on $>1''$ scales.

We apply some additional cuts to this catalog before producing our stacked SEDs. To avoid double counting sources or potentially including sidelobes of very bright sources, we exclude sources with neighbors within $1'$, roughly corresponding the the beam scale of ACT. This cut leaves 9,436 objects that fall within the overlapping FIRST and ACT observing regions (339 deg^2; $305^\circ \leq$ R.A. $\leq 58^\circ$, $-1.5^\circ \leq$ Dec. $\leq 1.5^\circ$).

We additionally restrict the 1.4 GHz flux range of the sample, reducing the total number of objects to the 4,563 sources with NVSS-determined fluxes $5 < S_{1.4} < 200$ mJy. This flux cut allows us to avoid issues with the differing flux density thresholds of the FIRST and NVSS surveys as well as restricting the catalog to a statistically well defined sample by excluding the few extraordinarily bright objects at high fluxes.

Radio sources selected at 1.4 GHz are likely drawn from a population of both radio-loud AGN and star forming galaxies (SFGs). These SFGs comprise of a low redshift (z 0.1) population of galaxies whose star formation rates are high enough that significant radio emission is present in the form of synchrotron and free-free emission associated with their young stellar populations. We're interested restricting the population as best we can to radio AGN and therefore aim to remove such source. Based on the empirical 1.4 GHz source count models based on luminosity functions from Dunlop & Peacock (1990) and Sadler et al. (2002), we expect $\sim$140 SFGs for this sample and find 149 SFGs in the Best & Heckman (2012) catalog). By removing sources in the catalog within $5'$ of classified SFGs from Best & Heckman (2012), we remove a 211 sources from the sample.

To further enhance the purity of our sample, we also exclude sources detected with an ACT flux density above 3 times the locally measures RMS noise level in any of the ACT bands. Detected sources in ACT represent extraordinary objects biased bright by either by the orientation of their emission mechanisms (e.g. blazars, Urry & Padovani, 1995) or due to the presence of intervening structures strongly magnifying their observed emission (e.g. lensed dusty star forming galaxies, Marsden et al., 2014a; Negrello et al., 2010; Vieira et al., 2010). Strong negative signals in the ACT 150 GHz band likely represent the SZ signal from contaminating foreground galaxy clusters. Since the noise in the ACT datasets are not entirely uniform, these noise based cuts are not uniform in their corresponding flux but typical values for these thresholds are 6 mJy at 148 GHz, 9 mJy at 218 GHz, and 18 mJy at 277 GHz. The ACT flux density cuts exclude 219 (4.8%) radio sources from the Kimball & Ivezić (2008) sample. While the cuts detailed above are performed to construct an unbiased sample, we find that modifying the details of the cuts (such as the flux density thresholds) does not strongly influence the results of the stacking procedure.

For the remaining 4,344 sources, assumed to be comprised of almost entirely of radio AGN, we adopt the empirical redshift distribution of de Zotti et al. (2010) (constructed with data from Brookes et al., 2008), which we make use of when modeling the stacked SED. This distribution is plotted in Figure 2.2 and has a median redshift of 1.06.

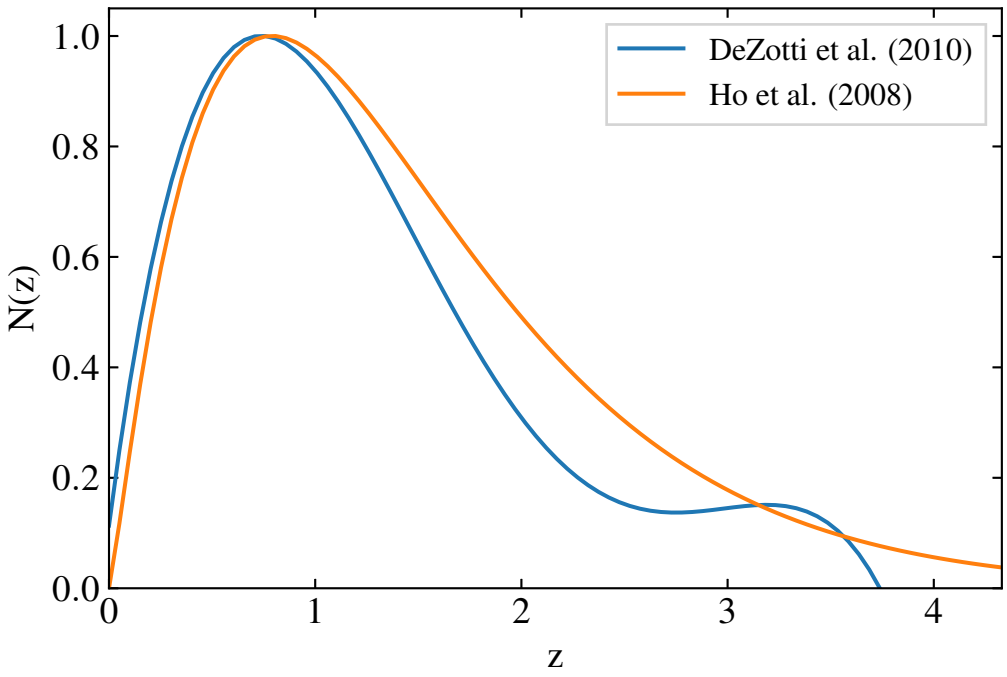

Figure 2.2: Blue: The assumed redshift distribution of the radio AGN sample based on the the fit of de Zotti et al. (2010) to data from Brookes et al. (2008). Orange: The redshift distribution of Ho et al. (2008) which is used as another estimate of the redshift distribution in the calculation of the systematic effects a different distribution could have in Section 2.6.2.

2.2 Radio to Millimeter Datasets

For this work we construct stacked SEDs using seven bands in addition to the 1.4 GHz flux densities from the NVSS measurements in the sample catalog. We use three bands of ACT data from the equatorial survey as described in Section 1.4 as well as three bands of *Herschel*-SPIRE data described in Section 1.5. Of the radio sources in the sample from Kimball & Ivezić (2008), 2,123 fall within the HerS or HerMES survey regions. In addition, in order to get stronger constraints on the synchrotron emission of the radio AGN, we make use of 4.85 GHz data from the Parkes-MIT-NRAO survey[2] (PMN; Griffith & Wright, 1993; Tasker et al., 1994) and a Green Bank Telescope survey (Condon et al., 1994).

For the ACT data we use point source matched filtered maps described in Marriage et al. (2011a). To extract flux densities from these data for the large catalog of radio sources we simply take the pixel-centered estimate of the flux but then apply a correcting factor for the smearing out of the source signals that occurs due to the pixelization on the ACT maps. Assuming the sources are uniformly distributed within the ACT map's $0.5'$-square pixels the average correction factors are found to be 1.06 at 148 GHz, 1.10 at 218 GHz, and 1.14 at 277 GHz. For the other datasets, the instruments beams are sufficiently well sampled by the map pixelization that such effects are negligible.

We check the ACT datasets for biases by performing null tests, calculating the stacked flux densities of randomly selected locations within the ACT and FIRST overlap region in all three ACT frequency bands. These null catalogs are subject to the same flux cuts

[2]http://www.parkes.atnf.csiro.au/observing/databases/pmn/pmn.html

and masks as the non-randomized data. We performed these null tests using 1000 random realizations of null catalogs with sources arbitrarily split into bins of the same size as each of the seven flux bins described in Section 2.3. These tests were found to be consistent with no signal, indicating no detectable systematic bias in the ACT data within the statistical uncertainties. Quantifying this, we found these null tests to be consistent with zero signal with a χ^2 of 5.7, 11.3 and 3.4 at 148 GHz, 218 GHz and 277 GHz, respectively, each with 7 degrees of freedom (for the the 7 flux bins). The corresponding probability of a random realization to exceed the observed 148 GHz, 218 GHz and 277 GHz χ^2 estimates are 0.57, 0.13 and 0.85 respectively.

2.3 Stacked AGN Spectral Energy Distributions

With the data in hand, we construct stacked estimates of the mean radio to far-infrared SEDs of the radio AGN sample by taking the weighted averages of flux density estimates of each source in the catalog. Stacking can be shown to produce the maximum likelihood estimate of the average SED of a source sample when the noise in the data is gaussian or confusion limited (see Appendix A). Before stacking we bin the sources in seven logarithmically spaced bins in 1.4 GHz flux, $S_{1.4\,\mathrm{GHz}}$ (as determined by the NVSS flux measurements) with bin centers ranging from 6.4 mJy to 149.1 mJy. The 1.4 GHz flux densities are used directly in normalizing the modeled synchrotron emission and are therefore not used as data points in the fits described below. For the ACT flux densities, we use the ACT

Table 2.1: Mean flux density at radio source locations for the radio-loud AGN catalog. The uncertainties are calculated through a bootstrapped resampling analysis.

Bin	$S_{1.4}$ Range (mJy)	N_{bin}	$S_{1.4}$ (mJy)	$S_{4.8}$ (mJy)	S_{148} (mJy)	S_{218} (mJy)	S_{277} (mJy)	$S^{\dagger}_{600}$ (mJy)	$S^{\dagger}_{857}$ (mJy)	$S^{\dagger}_{1200}$ (mJy)
1	5.00 – 8.47	1767	6.43	3.7 ± 0.2	0.37 ± 0.05	0.66 ± 0.08	1.0 ± 0.2			
2	8.47 – 14.3	1092	10.9	5.7 ± 0.3	0.38 ± 0.07	0.79 ± 0.1	1.3 ± 0.2			
3	14.3 – 24.3	672	18.5	7.8 ± 0.3	0.59 ± 0.09	0.83 ± 0.1	1.5 ± 0.3			
4	24.3 – 41.2	412	31.3	$12. \pm 0.5$	0.64 ± 0.1	1.1 ± 0.2	0.96 ± 0.3	3.9 ± 0.4	4.4 ± 0.4	4.4 ± 0.4
5	41.2 – 69.7	222	53.5	$21. \pm 0.9$	0.94 ± 0.1	1.4 ± 0.2	1.5 ± 0.5			
6	69.7 – 118.	118	88.4	$30. \pm 1.$	1.4 ± 0.2	1.8 ± 0.3	2.7 ± 0.7			
7	118. – 200.	61	149.	$45. \pm 1.$	1.9 ± 0.3	0.83 ± 0.4	1.5 ± 0.9			

†The *Herschel* data shown correspond to a single 1.4 GHz flux density bin containing all radio sources in the sample within the *Herschel* survey area.

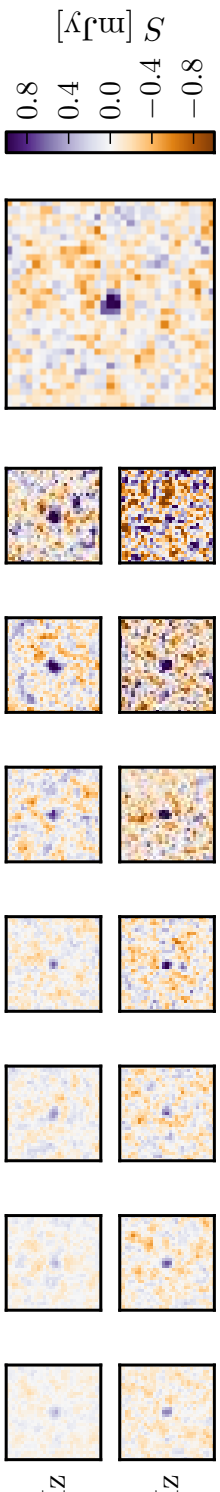

Figure 2.3: Thumbnail images ($0.25^\circ \times 0.25^\circ$) of matched filtered ACT data stacked on FIRST source locations, and binned by NVSS 1.4 GHz flux. Some contribution of the SZ decrement can be seen as the signal at 148 GHz is diminished in the lower flux density bins while the the 218 GHz flux remains bright. The 277 GHz map is significantly noisier than the other bands so we choose to show, for visualization purposes only, the 277 GHz flux densities stacked for the entire sample instead of for each $S_{1.4\,\mathrm{GHz}}$ bin. The bin indices correspond to those shown in Table 2.1.

hits-counts maps, which encode how time much ACT observed each patch of the sky in the observing seasons the data are drawn from, as the weights in our average. These weight maps roughly correspond to inverse variance weights in the case of matched filtered maps (e.g. Marriage et al., 2011a).

Similarly, weighted averages are determined for the 4.85 GHz GBT/PMN and far-infrared *Herschel*-SPIRE data. These the weights for these data area defined as the inverse of the square of the uncertainties on the flux density measurements derived from error maps provided by these surveys. The *Herschel*-SPIRE datasets used do not fully overlap with the region of sky we are using (defined by the ACT equatorial survey) so instead we make use of only the 2,123 out of 4,344 radio sources that lie within our survey area. Due to the restricted statistics on the far-infrared data and the low level of dusty emission expected from these sources (which should be the dominant source of emission at these bands), we do not separate the far-infrared data into bins before stacking. Instead, we construct stacked estimates for the entire unbinned sample and assume these estimates hold within there uncertainties for each bin when we fit models to the stacked data.

We derive uncertainties on these weighted average flux estimates by preforming a bootstrap analysis where we resample from the flux bins, with replacement, and estimate the standard deviations on the stacked flux densities from the standard deviations of these resamples. We note that the uncertainties thus determined are found to be significantly (up to 10 times) higher than expected from just statistically averaging down the known noise levels in the ACT data sets given the number of sources present. This indicates that sample

variance is, fractionally, a large contributor to the uncertainties, in particular for the low flux bins where the source counts per bin are high.

The results of the stacking procedure are shown in Table 2.1. Each row shows the stacked flux density results for each $S_{1.4\,\mathrm{GHz}}$ bin for each of the radio to far-infrared bands we use. Thumbnail images of the stacked ACT data in each bin are additionally shown in Figure 2.3. The stacked flux densities correspond to $> 3\sigma$ detections at 148 GHz and 218 GHz for all except the highest $S_{1.4\,\mathrm{GHz}}$ bin. Typical ranges for the ACT flux densities are found to be 0.2 mJy to 2.0 mJy with the lowest $S_{1.4\,\mathrm{GHz}}$ bin comprising 1,767 sources and the highest comprising 61 sources.

Qualitatively, at low frequencies, the flux densities appear generally as expected for a synchrotron dominated emission spectrum. The stacked 148 GHz, 218 GHz and 277 GHz flux densities are always lower than the typical 1.4 GHz flux in each bin, which is expected with for a power law synchrotron dominated spectrum with $S_\nu \propto \nu^{-\alpha}$ and $\alpha_{1.4\,\mathrm{GHz}-148\,\mathrm{GHz}} > 0$. However this behavior does not extend to the higher frequency bands where $S_{218\,\mathrm{GHz}}$ and $S_{277\,\mathrm{GHz}}$ are greater than $S_{148\,\mathrm{GHz}}$ for almost all $S_{1.4\,\mathrm{GHz}}$ bins. In the following section we quantitatively explore physical explanations for the shape of the stacked SEDs by fitting composite models to these data with different physically motivated components.

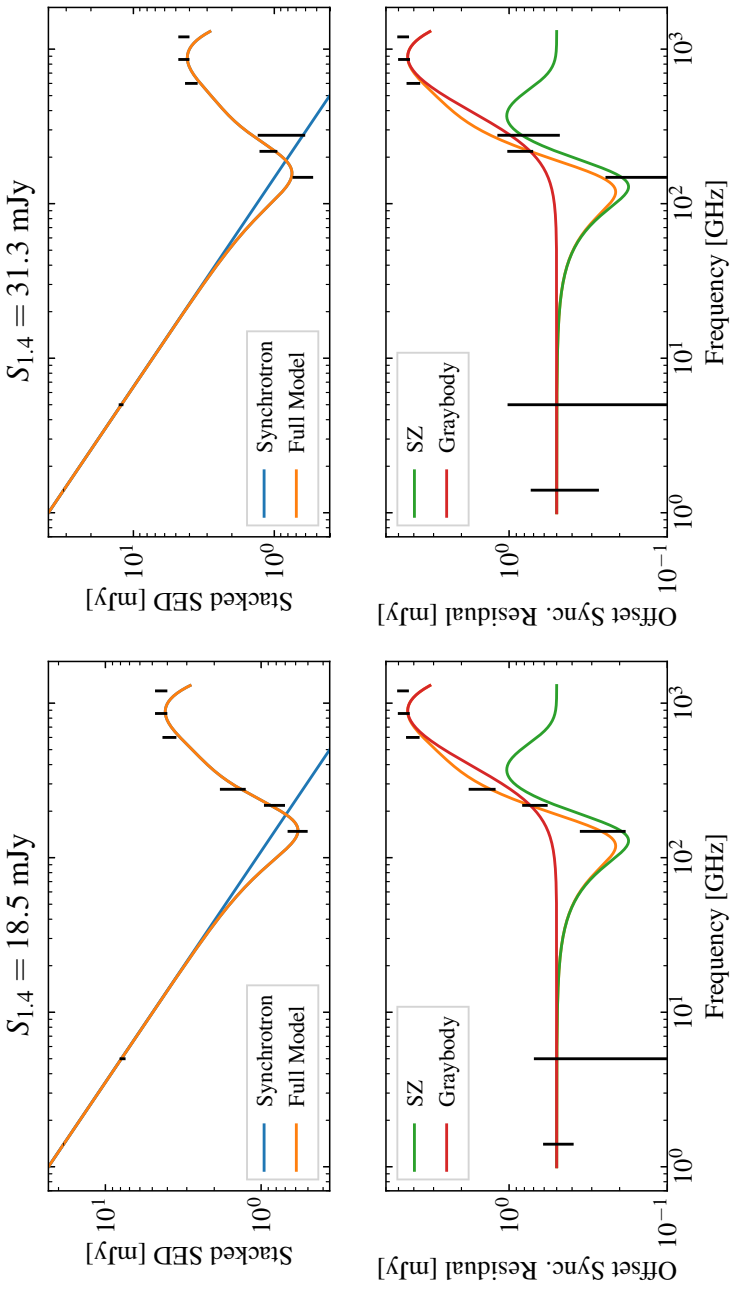

Figure 2.4: Individual stacked SEDs for two different 1.4 GHz flux density bins (left and right). For each of these bins, we plot on the top row: The PMN/GBT, ACT and *Herschel*-SPIRE stacked flux densities along with the best-fit model curve and synchrotron component. On the bottom row: The residual stacked SEDs after subtracting the best-fit synchrotron spectrum (offset from zero by 0.5 mJy for visualization purposes). Overlayed with these residuals are the best-fit SZ and graybody dust components of the model. All data shown are listed in Table 2.1. Figure 2.5 shows these same data (sans the *Herschel*-SPIRE bands) and model components for all 1.4 GHz flux density bins simultaneously.

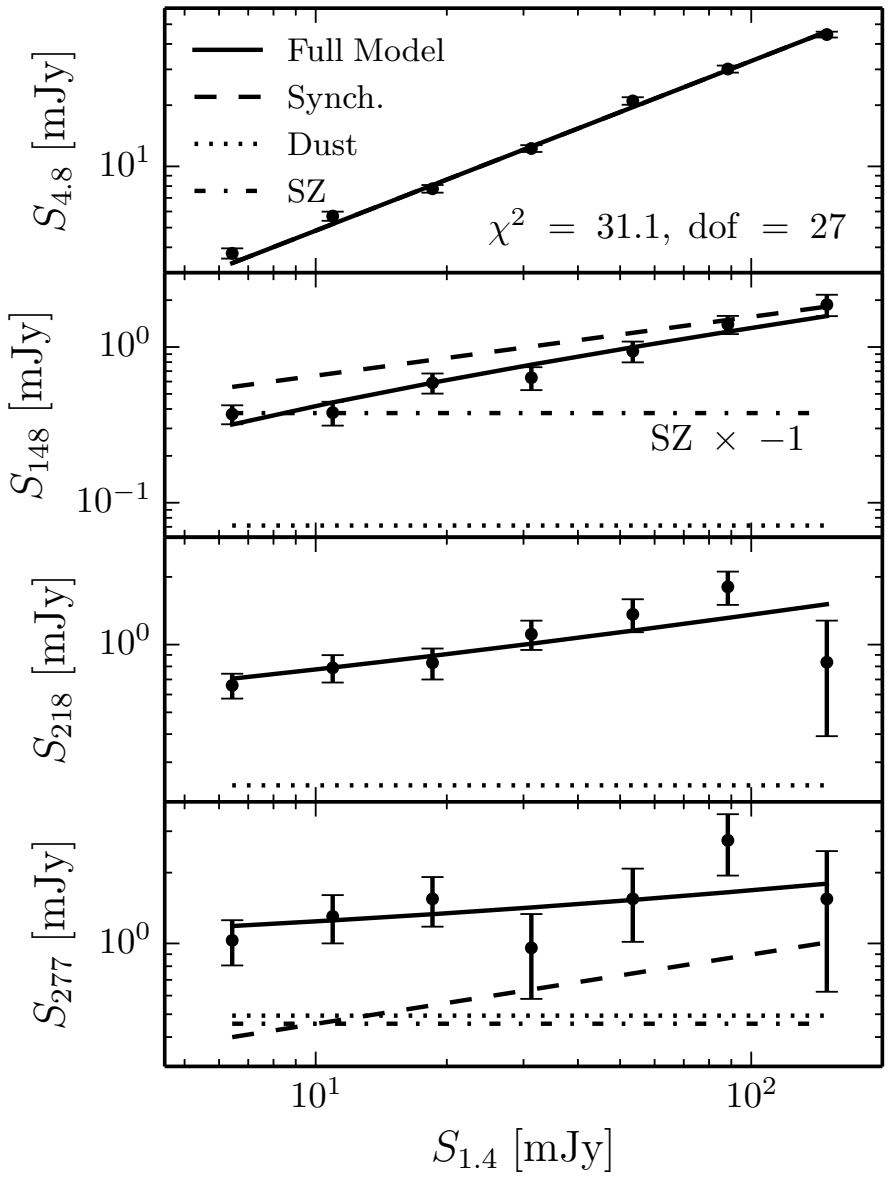

Figure 2.5: The PMN/GBT stacked flux densities at 4.8 GHz and the ACT stacked flux densities at 148 GHz, 218 GHz and 277 GHz. The curves corresponding to the best-fit model and its components overlaid. The dashed line represents the AGN emission and the dotted line represents the contribution from dust emission. The dot-dashed line shows the SZ effect contribution of the halos hosting the AGN ($A_{\rm SZ}$), which is negative for ν<218 GHz. The solid line displays the sum of the AGN emission, the SZ effect and the dust contribution which is well fit by the data. All data are listed in Table 2.1.

2.4 Modeling AGN emission

The models we construct to fit the stacked radio-AGN SEDs consist of components for the observed flux corresponding to synchrotron emission, SZ effect and dusty graybody emission. Figure 2.4 shows an example of what one of these best fit composite models looks like for individual flux bins.

The synchrotron component of the flux density is modeled assuming a power-law spectral index, the expected emission for a population of electrons with a power-law energy distribution. The form of this contribution for the observed flux density in 1.4 GHz flux bin i is

$$S_{i,\nu,\mathrm{sync.}} = S_{i,1.4\,\mathrm{GHz}} \left(\frac{\nu}{1.4\,\mathrm{GHz}} \right)^{-\alpha_i}, \tag{2.1}$$

where $\langle S_{1.4\,\mathrm{GHz}} \rangle_i$ is the average 1.4 GHz flux in that bin (derived from NVSS measurements). In the fiducial model (which we will attempt extensions to in Section 2.5), the spectral index α_i is fixed as a function of observed frequency, ν but we allow for evolution of the spectral index as a function of 1.4 GHz flux. This evolution is found to be empirically necessary in order to provide an accurate fit for the data, see Figure 2.7. We parameterize this evolution with

$$\alpha_i = \alpha_0 + \alpha_1 \log_{10}(S_{i,1.4\,\mathrm{GHz}}/S_{\mathrm{pivot}}), \tag{2.2}$$

where α_0 and α_1 are fit as a function of $S_{i,1.4\,\mathrm{GHz}}$ and choose the normalization, $S_{\mathrm{pivot}} = 149.1\,\mathrm{mJy}$ corresponding to the average 1.4 GHz flux density for the highest flux bin, so as

to minimize degeneracy between α_0 and α_1. Since the AGN population is characterized by a joint distribution of both flat-spectrum and steep-spectrum sources (de Zotti et al., 2010; Massardi et al., 2011, e.g.), this evolution in flux likely encodes the varying contributions of these two source populations as a function of 1.4 GHz flux.

For the tSZ component, we use the non-relativistic tSZ spectrum, $g(\nu)$ described in Equation 1.36. To parameterize this contribution, we normalized this spectrum to 1 mJy at 148 GHz such that the contribution in each 1.4 GHz flux bin i, is

$$S_{i,\nu,\mathrm{tSZ}} = -A_{\mathrm{SZ}}\, g(\nu)/g(148\,\mathrm{GHz}) f_\nu^{-1}. \tag{2.3}$$

Here f_ν is a bias correcting factor which accounts for the band dependent interaction of the on-sky angular profile of the SZ signal with the ACT point source matched filter, as discussed in Section 2.6.2. We keep A_{SZ} constant across flux density bins as, should this signal be purely mass dependent as is the case of a purely gravitationally heated halo, the distribution of radio luminosities has been shown not strongly correlate with host mass or cluster velocity dispersion (Best et al., 2005, 2007). Additionally, we empirically see that the SZ effect in the model accounts for an observed offset in the expected emission subtracted flux residual which is roughly constant as a function of $S_{i,1.4\,\mathrm{GHz}}$ (as can be seen in the lower panel of Figure 2.7).

For the dust component we assume a graybody spectrum with a fixed temperature, T, and emissivity index, β. The observed flux density for a source in 1.4 GHz flux bin i, at

redshift z is parameterized as,

$$S_{i,\nu,\mathrm{dust}} = \frac{L_{\mathrm{IR}}}{4\pi D_{\mathrm{L}}^2(z)} \frac{(\nu(1+z))^{\beta} B_{\nu(1+z)}(T)}{\int (\nu')^{\beta} B_{\nu'}(T)\,\mathrm{d}\nu'} \tag{2.4}$$

where the limits of the normalizing integral are taken to be 300 to 2.1×10^4 GHz such that L_{IR} represents the observed bolometric luminosity of the source within that observed far-infrared frequency range. The blackbody spectrum $B_\nu(T)$ is taken to be that of a 20 K source for all objects, and we choose to use an emmissivity index $\beta = 1.8$. Such a spectrum is typical of *Herschel* observations of a subset of a similarly selected sample of AGN with available SDSS spectroscopy (Hardcastle et al., 2013). We explore the affect on the results of varying these parameters below.

In modeling the flux densities of our sources, we require redshift information of our sample. As this is not a spectroscopic sample for which redshifts are available for each source, we make use of an estimate of redshift the distribution of the entire sample in constructing our models for the average observed flux densities. For this purpose, we make use of the redshift distribution based on data from Brookes et al. (2008) with the parametric form given by de Zotti et al. (2010) and plotted in Figure 2.2.

This redshift distribution enters the model in the construction of the composite gray body spectrum (Equation 2.4) and in the angular shape of the average SZ pressure profile, which affects how the SZ signal is sampled by the filter as discussed in Sections 2.4 and 2.6.2. For this assumed redshift distribution, the measured SZ effect at 277 GHz is 12%

lower than that inferred by the spectral behavior (Equation 1.36) and the SZ effect amplitude at 148 GHz. This correction factor is included in the construction of the model, which is parameterized by the SZ effect amplitude at 148 GHz, $A_{\rm SZ}$. The fiducial synchrotron model is not depended on the redshift distribution of the sample as it is modeled as a simple power-law.

To constrain the free parameters of our model, we employ an MCMC analysis to estimate the posterior distribution of $\alpha_0, \alpha_1, A_{\rm SZ}$ and $\log_{10}(L_{IR}/L_\odot)$. We assume uniform priors for these parameters throughout. For the likelihood function, we assume a composite Gaussian likelihood with covariance matrices C_i that account for the independent statistical uncertainties in the data as well as the correlated calibration uncertainities inherent in each dataset: (See Sections 1.4 and 1.5)

$$\ln \mathcal{L} = -\frac{1}{2}\sum_{i}^{\rm Bins} (\vec{d}_i - \vec{S}_i)^{\mathsf{T}} \mathsf{C}_i^{-1} (\vec{d}_i - \vec{S}_i) \tag{2.5}$$

Here $\vec{d}_i$ is the vector of stacked flux densities in each band for 1.4 GHz flux bin i. Similarly, $\vec{S}_i$ represents the vector of total model contributions in each band for each flux bin b and is a function of the free model parameters $\alpha_0, \alpha_1, A_{\rm SZ}$ and $\log_{10}(L_{\rm IR}/{\rm L}_\odot)$. This total model is taken as the average over the source population in a bin assuming they are drawn from the approximate redshift distribution discussed above.

Figures 2.5 and 2.4 show the models evaluated for the best fitting parameters along with the data. In Figure 2.5 we show all 1.4 GHz flux bins simultaneously whereas Figure 2.4 shows fits for two individual flux density bins. Figure 2.6 shows the resulting parameter

distributions for the main parameters of interest. All chains show good convergence, with Gelman-Rubin R - 1 parameter < 0.005. The best fit model has a $\chi^2 = 31.1$ with 27 degrees of freedom (PTE=0.27), indicating that the model is a good fit to the data.

The parameter constraints we obtain are informative for both the emission spectrum and the SZ effect associated with these systems. We detect the SZ signal parameterized as $A_{\rm SZ} = 0.306 \pm 0.052$ mJy with 5σ confidence. This signal, which had not been previously detected, is interpreted further in Section 2.6.2. While such a signal could be driven by energy injected through feedback processes, we find that the observed level of SZ signal is consistent with expectations given other SZ measurements of low mass systems when combined with the estimated mass of the host halos of AGN. This is indicative of an SZ contribution source only through gravitational heating of the ionized hot halos.

2.5 Interpretation of the Synchrotron and Dust Component

We detect a contribution from a dusty graybody emission with bolometric luminosity $\log_{10}(L_{\rm IR}/{\rm L}_\odot) = 9.96 \pm 0.08$ which predominantly arises from the fitting the *Herschel*-SPIRE data points. As can be seen in Figure 2.5, the emission associated with this model component does not significantly contribute to bands at the millimeter and lower frequencies where the SZ and synchrotron components dominate.

When we explore models where we vary the dust temperature, T, and emissivity, β, of

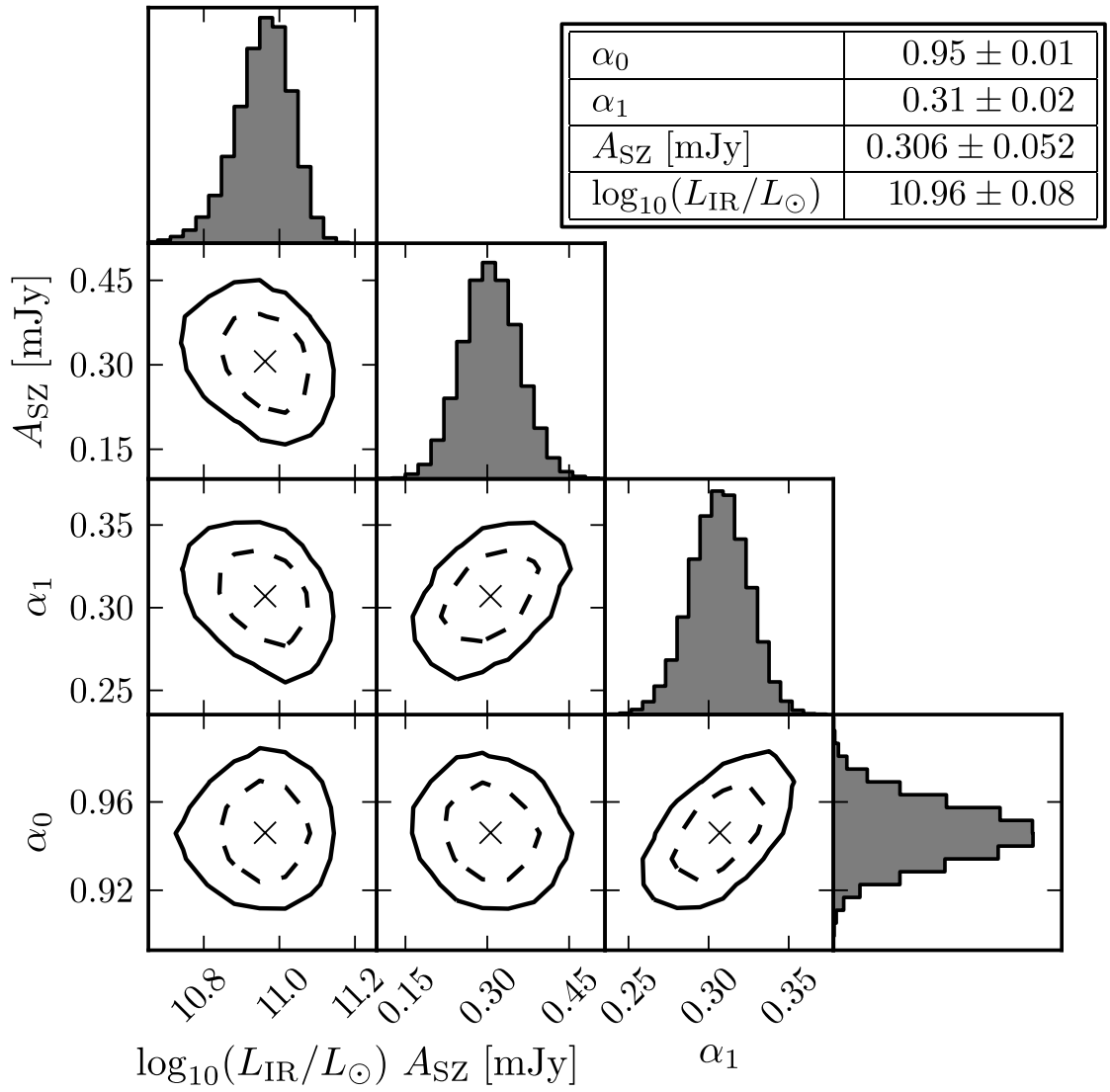

Figure 2.6: The marginalized posterior distributions of the model parameters, with best fit values listed in the inset table. The histograms show the single-parameter marginalized distributions for each parameter. The dashed lines show the 68% confidence regions, and the solid lines show the 95% confidence regions. The parameters correspond to the effective AGN spectral index at the highest 1.4 GHz flux density (α_0), the logarithmic slope of the AGN spectral index (α_1), the amplitude of the SZ from ionized gas in AGN dark matter halos ($A_{\rm SZ}$), and the bolometric IR luminosity ($\log_{10}(L_{IR}/L_\odot)$).

the graybody dust model beyond the fiducial values of $T = 20\,\mathrm{K}$ and $\beta = 1.8$ we assumed, we find that our results are robust for most choices. For each combination of $\beta = 1.5, 1.8$ or 2.0 and $T = 10, 15$ or $20\,\mathrm{K}$, the constraints on all our model parameters, except for $\log_{10}(L_{\mathrm{IR}}/\mathrm{L}_{\odot})$ which by definition changes under a different spectrum, vary at less than the 1σ level. Additionally, in terms of goodness of fit, we find that our data strongly disfavor models with a significantly lower dust temperature as the χ^2 is found to increase by > 13 for $T = 15, 10\,\mathrm{K}$ models compared to the $T = 20\,\mathrm{K}$ model for all emissivity indices.

We find that the average effective spectral index from 1.4 to 4.8 GHz, ($\alpha_{1.4-4.8\,\mathrm{GHz}}$) is consistent with the spectral index from 1.4 to 218 GHz ($\alpha_{1.4-218\,\mathrm{GHz}}$) for all 1.4 GHz flux density bins as demonstrated in Figure 2.7. As there is no significant SZ contribution at 218 GHz, due to this band coinciding with the null point of the SZ spectrum, the consistency of these indices is an important verification of our model. The agreement of these indices is indicative of the fact that, aside from the SZ contribution, the emission in the millimeter has negligible dust contribution and is well modeled by synchrotron spectrum extrapolated from 1.4 GHz. Additionally, these data are consistent with a single average spectral index which varies as a function of $S_{1.4\,\mathrm{GHz}}$, as we have assumed in our model. The effective indices are calculated for a given 1.4 GHz flux density bin, i by solving, for example in the case of $\alpha_{1.4-218\,\mathrm{GHz}}$, $S_{i,218\,\mathrm{GHz}} = S_{i,218\,\mathrm{GHz}}(218/1.4)^{-\alpha}$ for α.

The parameters describing the dependence of the AGN spectral index on $\langle S_{1.4\,\mathrm{GHz}}\rangle$, α_0, and α_1, are predominantly constrained by the intermediate to high $\langle S_{1.4\,\mathrm{GHz}}\rangle$ flux density bins where the SZ effect is less relevant to the overall flux denity observed in the millimeter

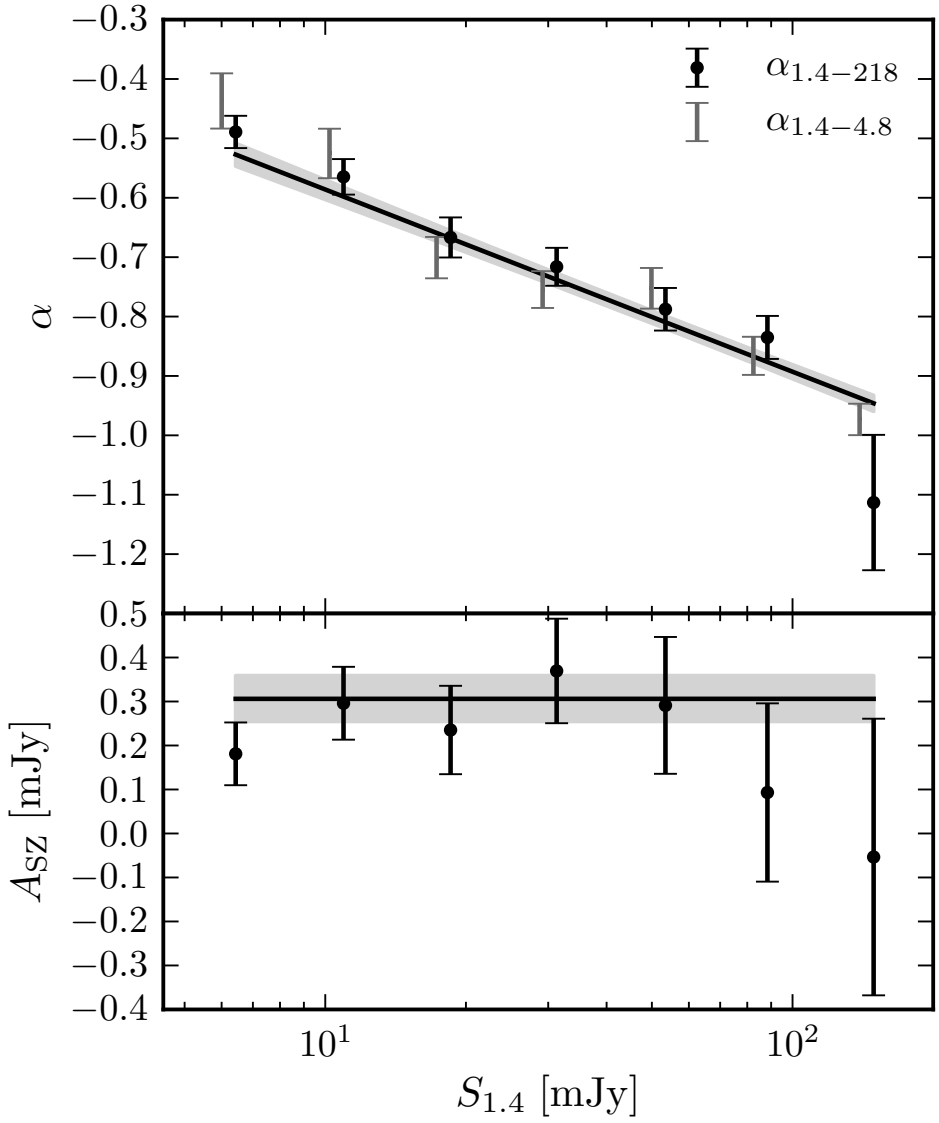

Figure 2.7: Top: the effective 1.4 to 218 GHz and 1.4 to 4.8 GHz spectral indices for each 1.4 GHz flux density bin (error bars), derived from taking the ratios of the logarithms of these data. The results effective indices are compared to the best-fit synchrotron model index, α (solid line), for which the slope and normalization are fit. Bottom: the amplitude of the inferred SZ signal in each bin compared to the best-fit model, which is fit equally with a constant with across all 1.4 GHz flux density bins. The gray regions represent the 68% confidence intervals of the best-fit model. The data points shown in the bottom plot are calculated as the emission residual when comparing the 148 GHz data to the predictions of a model with no SZ contribution.

bands. The effective AGN spectral index in the highest flux density bin, $\alpha = 0.95 \pm 0.01$ is consistent with expectations for optically thin "steep spectrum" synchrotron sources. However, the positive value of $\alpha_1 = 0.31 \pm 0.02$ is indicative of significant evolution of the effective AGN spectral index as a function of 1.4 GHz flux density, tending towards and effective index of $\alpha = 0.5$ at the lowest flux density bin. This is consistent with a trend towards a source population composed of a mixture of both flat and steep spectrum sources at these lower 1.4 GHz flux density ranges.

As the sources used in this study were radio-selected, we can check this hypothesis against population models for low-frequency radio-selected sources. Massardi et al. (2011) model source populations selected from 1–5 GHz bands. Similar to the results found in de Zotti et al. (2010), they find steep spectrum sources to be the dominant contributor to the source population at all 1.4 GHz flux density levels. However, BL Lac sources, which have a characteristically flat spectrum, are found to be increasingly prevalent at low flux densities ($\lesssim 10$ mJy). Additionally flat spectrum radio quasars are found to contribute increasing at high flux densities ($\gtrsim 500$ mJy). While these studies are based on lower frequency observations, this behaviour is broadly consistent with the evolution favored in our modeling of the average synchrotron spectral index, assuming these spectral indexes are comparable at millimeter bands.

In addition, to be conservative about whether our expectations for these spectral indices hold at the higher frequencies relevant to the SZ signal, we also evaluate whether the observed high frequency flux densities could be explained by electron aging or another

physical process by which the synchrotron spectral index might steepen, such that the millimeter signal is lower than that extrapolated from a constant spectral slope. Some models predict such steepening effects in the millimeter bands for only the brightest sources (e.g. Ghisellini et al., 1998) but there are a broad range of references supporting or opposed to these effects found in e.g. de Zotti et al. (2010). In order to empirically test for steepening effects in our data, or equivalently a contribution from a flat spectrum source population not captured by our fiducial two parameter spectral index evolution mode, we introduce an additional parameter, C_α, defined such that $\alpha(\nu > \nu_{break}) = C_\alpha \alpha(\nu < \nu_{break})$, where C_α is allowed to vary from -10 to 10 (and is therefore able to capture both a a steepening, flattening, or inverted spectrum). We introduce a parameter for the location of the break in the synchrotron spectrum, ν_{break} where this transition occurs.

We show the MCMC paramter contours for this model in Figure 2.8. While the location of the break in this spectrum is not well constrained it tends towards the millimeter bands. However, importantly for our purposes, including this additional flexibility in the synchrotron spectrum modeling does note affect the SZ amplitude $A_{\rm SZ}$ becomes 0.304 ± 0.057 mJy (5σ significance). When including the entire sample, from low 1.4 GHz flux densities to high, the best fit value for this new parameter is $C_\alpha = 1.05 \pm 0.30$. The χ^2 value for the fit is 31.0 for 25 degrees of freedom (PTE = 0.19), so the fit is not significantly improved by the addition of this parameter. If we only model the sources with $S_{1.4} < 10$ mJy, the value for C_α does not change significantly. The emergence of a population of flat-spectrum sources could in principle contribute to the term in our model at-

tributed to the SZ effect at low 1.4 GHz flux densities, but this scenario is not preferred by our data when we introduce C_α. If we completely replace the SZ effect parameter from the model by this C_α parameter, the resulting $\chi^2 = 55.3$, with 26 degrees of freedom — a significantly worse fit. Finally, we saw in Section 2.4 that for the model in which we include an SZ effect parameter, the average spectral index from 1.4 GHz to 4.8 GHz agrees well with the average spectral index from 1.4 GHz to 218 GHz for each 1.4 GHz flux density bin, implying that the simpler model without spectral steepening adequately describes the data (see Figure 2.7).

2.6 Interpretation of the SZ signal

Our modeling described above indicates a strong, 5σ, preference for an SZ contribution parameterized empirically through its amplitude at 148 GHz. In the subsequent sections we evaluate systematic effects in connecting this observed amplitude to expectations for the integrated SZ signal for AGN hosts and interpret the signal in the context of expectations based on gravitational heating.

2.6.1 Galaxy Groups and Clusters

For this work we're interested in the SZ signal associated with the typical host halos of radio-selected AGN. However, some fraction of these objects are likely hosted by massive galaxy clusters or groups whose larger SZ signals might dominate the typical signal of indi-

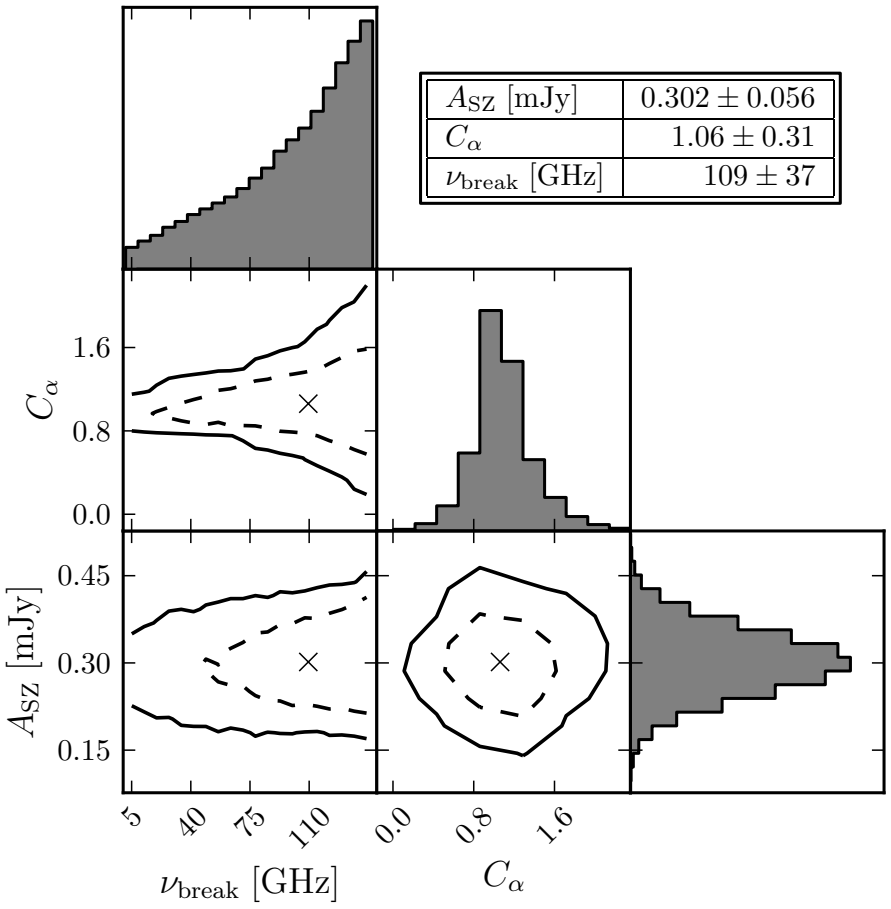

Figure 2.8: The marginalized posterior distributions of the parameters for the model where spectral steepening is allowed, with best fit values listed in the inset table. The histograms show individual parameter marginalized distributions. The dashed lines represent the 68% confidence regions while the solid lines show the 95% confidence regions. The parameters correspond to the amplitude of the SZ from ionized gas in AGN dark matter halos ($A_{\rm SZ}$), the amount by which the synchrotron spectrum index steepens (C_α), and the break frequency at which the spectrum steepens (ν_{break}). This break frequency, ν_{break}, is not well constrained by our data and tends to prefer a location for the steepening above the lowest ACT band in the millimeter. The amplitude of the SZ effect is significantly non-zero even for models in which steepening is allowed, demonstrating that this type of modified synchrotron emission does not negate the need for an SZ contribution.

vidual AGN host halos. To check whether this is the case, before interpreting our observed signal futher, we identify sources which are likely associated with optically selected galaxy clusters and determine the affect of removing such sources from our sample on the resulting stacked flux densities. It should be noted that our catalog has already had sources with negative 148 GHz flux density more than 3 times greater in amplitude than the map noise level, which implicitly excludes sources associated with galaxy clusters detected through the SZ effect.

For this additional check we make use of the Gaussian Mixture Brightest Cluster Galaxy (GMBCG) catalog[5] (Hao et al., 2010) that contains more than 55,000 optically-selected galaxy clusters in SDSS Data Release 7 with redshift range $0.1 < z < 0.55$.

While the redshift distribution of our sample extends to higher redshifts than this sample (Figure 2.2), the number of radio sources per cluster mass has been found to not evolve strongly with redshift (Gralla et al., 2011). This, combined with the fact that the number density of radio sources does increase with redshift, implies that the fraction of radio loud AGN in clusters at redshifts above $z \sim 0.5$ is likely lower than today. Therefore a significant fraction of any potential SZ contamination from sources hosted in the most massive systems should be captured by investigating these low to intermediate redshift clusters.

Within the area of overlap between the ACT and FIRST surveys, there are 1,903 GMBCG clusters. Comparing this subset with our 1.4 GHz sample, there were 405 sources within a $1'$ projected radius of a GMBCG cluster (out of 4,344 total sources in the sample).

[5] `http://home.fnal.gov/~jghao/gmbcg_sdss_catalog.html`

Of these, only 192 would have been included in the stacking analysis with others being excluded because of multiple overlapping radio sources. Excluding the sources near clusters from the analysis is found to change the observed $S_{148\,\mathrm{GHz}}$ stacked flux densities by $< 5\%$, which is small compared to the statistical errors. The model parameters (Section 2.4) are not significantly affected by the exclusion of sources that are near clusters, indicating that the A_{SZ} term is not dominated by the richest systems and is instead representative of the typical SZ contribution of AGN host halos.

2.6.2 The SZ effect of Radio Source Host Halos

As presented in Sections 2.3 and 2.4, there is evidence for the SZ effect from the hot atmospheres associated with the halos hosting the radio-loud AGN at 5σ level for our radio loud sample selected from Kimball & Ivezić (2008). In order to compare our results to other measurements of the SZ effect in the literature, we must convert the detected SZ amplitude to an integrated SZ signal describing the average SZ effect of the halos hosting the radio AGN. This conversion requires an assumed angular shape of the SZ effect in order to account for its convolution with the ACT beam as well as an accounting for the approximate redshift distribution of the sources as is used in Section 2.4.

Our measured deviation in the ACT 148 GHz flux densities of radio AGN due to the SZ effect A_{SZ} is described by the equation

$$A_{\mathrm{SZ}} = 2\pi I_0 \mid g(148\ \mathrm{GHz}) \mid \int \Phi(\theta)\hat{y}(\theta)d\theta, \tag{2.6}$$

where I_0 is the CMB intensity, $g(\nu)$ is the SZ distortion spectrum (Equation 1.36), and $\Phi(\theta)$ is the matched filter, all corresponding to the 148 GHz band. Spherical symmetry of the projected SZ effect has been assumed. The function $y(\theta)$ is the dimensionless Compton parameter as a function of angular distance from the center of the halo on the line of sight. The hat indicates it has been modified to account for the effects of the ACT beam and pixelization. This profile is related to the electron pressure profile $P_{\rm e}(r)$ through the line of sight projection according to

$$y(\theta) = \frac{\sigma_{\rm T}}{m_{\rm e}c^2} \int P_{\rm e}\left(\sqrt{l^2 + (R_{500}\theta/\theta_{500})^2}\right) {\rm d}l, \tag{2.7}$$

where σ_T is the Thomson cross section, $m_e c^2$ is the rest mass energy of the electron, and R_{500} and θ_{500} refer to the radius and angle, respectively, within which the average density of the dark matter halo is 500 times the critical density, $\rho_{\rm c}(z)$. Though we report quantities in this work referenced to the larger radius R_{200}, characteristic of the halo's virial radius, we adopt the R_{500} scaling for $P_{\rm e}(r)$ because we have chosen to model the pressure according to the "universal pressure profile" (UPP) of Arnaud et al. (2010). The UPP is derived from X-ray observations of clusters, for which R_{500} is a more natural scale. Sun et al. (2011) show that an average pressure profile for galaxy groups agrees well with the UPP. This profile is also used by Planck Collaboration et al. (2013b) to model the SZ effect of the halos hosting local bright galaxies which are similar in mass scale to the halos we probe here.

To estimate a characteristic R_{500} for the radio AGN, we use the lensing mass esti-

mate from Mandelbaum et al. (2009) ($M_{200} = 2.3 \pm 0.6 \times 10^{13}\ h_{70}^{-1}\mathrm{M}_{\odot}$). For R_{500} and other relevant quantities (e.g., angular diameter distance), we calculate means based on the redshift distributions shown in Figure 2.2. To use the mass estimate from Mandelbaum et al. (2009) with the UPP R_{500}-scaled profile, we convert M_{200} to $M_{500} \approx 1.5 \times 10^{13}\ h_{70}^{-1} M_{\odot}$ assuming the dark matter follows a Navarro et al. (1997) (NFW) profile, using the concentration−mass relation from Duffy et al. (2008). Estimated in this way, $R_{500} = 0.25\ h_{70}^{-1}\mathrm{Mpc}$ ($\theta_{500} = 0.64'$) for the radio-selected sample from Kimball & Ivezić (2008). While the redshift distribution of halos for which Mandelbaum et al. (2009) estimated a mean M_{200} is considerable lower redshift than the sample used here, lacking a better mass estimate for radio AGN-hosting halos we assume it holds true for this sample. As halos of higher mass are increasingly rare at higher redshift, this is likely an overestimate for the typical halo mass of host halos for AGN in this sample. However, other systematic effects (including the assumed redshift distribution) enter into the below calculations to a degree that using this approximate mass estimate is sufficient for these purposes.

Unfiltered brightness profiles proportional to $y(\theta)$ together with the ACT 148 GHz and 277 GHz beams are shown in Figure 2.9. Since the ACT data were filtered to optimally recover point source flux, we must correct for the bias arising from the interaction of the extended SZ intensity profile with the matched filter which is designed to optimally recover sources much smaller in angular extent than the beams. While it is the case that the emission effects modeled in 2.4 are emitted in regions of much smaller angular extent where the matched filter is appropriate, in general, the measured SZ amplitude A_{SZ} will

be lower than the total "SZ flux density" as this signal arises from the extended angular profile of the diffuse gas associated with the SZ host halos. To estimate the bias correction, we apply the same filter kernels to maps containing beam convolved simulated pressure profiles, input with known amplitude, and examine the resulting output amplitudes. Using simulated profiles placed according to the redshift distributions assumed for each sample, we can construct the estimated distribution of multiplicative factor f_ν required to correct for this bias. This bias factor allows us to write $A_{\rm SZ}$, as in Equation 2.6, in terms of the integrated Compton Y parameter, Y_{200}, defined as the Compton $y_{gas}(\theta)$ integrated to θ_{200}:

$$A_{\rm SZ} \approx I_0 \mid g(148\ {\rm GHz}) \mid f_\nu^{-1} Y_{200} \tag{2.8}$$

For the full sample of Kimball & Ivezić (2008) the mean corresponding factors are 1.23 and 1.37 for the ACT 148 and 277 GHz bands respectively. The ratio of the 148 GHz to 277 GHz bias correction factors was used in the modeling in Section 2.4 with a value of 12% for the mean SZ effect so that the shape of the modeled SED was not biased by these slightly band dependent factors. In the remainder of this section, we use the bias correction at 148 GHz to relate $A_{\rm SZ}$ (which is defined with respect to the 148 GHz flux density for the AGN sample) to estimates of Y_{200} with which we can compare to the literature. These assumptions yield an integrated $E(z)^{-2/3} D_A(z)^2 Y_{200} = 5.4 \pm 1.2^{stat} \times 10^{-8} h_{70}^{-2}$ Mpc^2 where D_A is the angular diameter distance and the uncertainties quoted are statistical only.

In order to characterize the level of additional systematic uncertainties in constructing these values, we varied the assumptions made in this calculation about the radio source

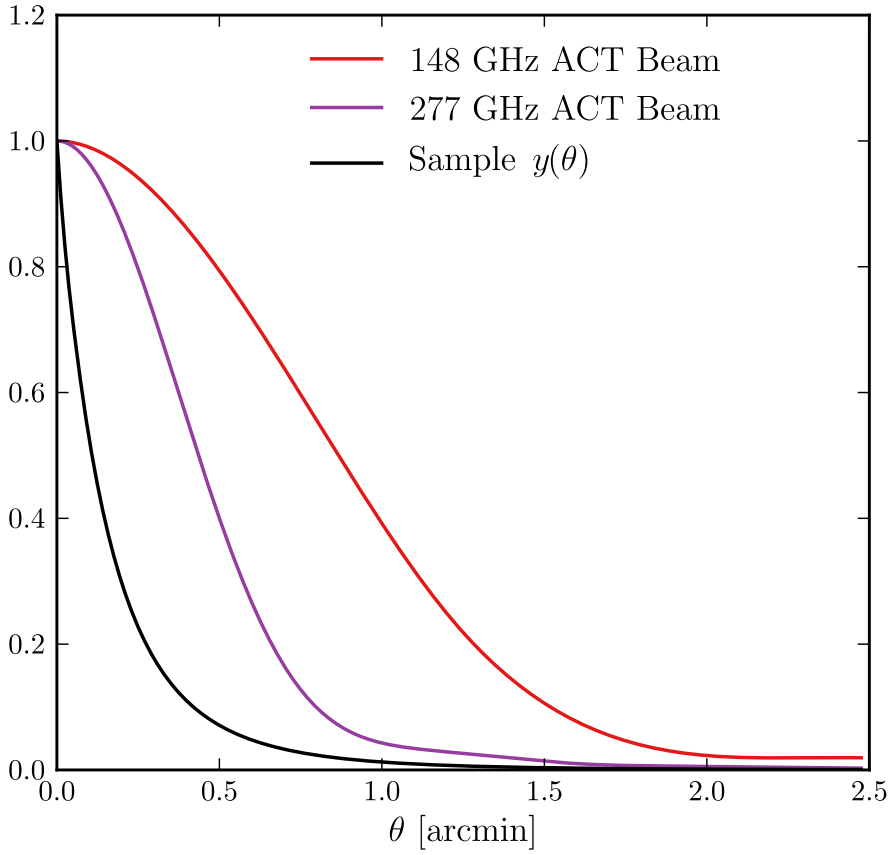

Figure 2.9: The angular profiles of the projected SZ effect from the assumed radial pressure profile alongside profiles of the ACT beams. The black line shows the profile assumed for the sample from Kimball & Ivezić (2008) (with angular extent assuming a source at the median $z = 1.06$). The red line shows the ACT 148 GHz beam profile, and the purple line shows the ACT 277 GHz beam profile. As shown, the angular extent of the SZ signal is seen to subtend a non-negligible fraction of the beams. When interpreting the SZ ampltitude, we correct the point source matched filtered data for this effect as described in Section 2.6.2.

redshift distribution, the typical pressure profile and the typical halo concentration (which is used to convert between M_{200} and M_{500} values). To estimate the systematic uncertainty contributed by each of these assumptions, we calculate the difference between the values given the alternative models described below and the values calculated using our fiducial model. To calculate an approximate total systematic uncertainty for each sample, we add these systematic uncertainties in quadrature. If we adopt the redshift distribution of the radio sources given by Ho et al. (2008), the value for the Kimball & Ivezić (2008) sample becomes $E(z)^{-2/3}D_A(z)^2Y_{200} = \ 4.5 \pm 1.0 \times 10^{-8}\ h_{70}^{-2}$ Mpc^2, which is in agreement with the value calculated above for the redshift distribution as reported by de Zotti et al. (2010). Adopting the halo concentration–mass relation from Neto et al. (2007) instead of the of Duffy et al. (2008), we find $E(z)^{-2/3}D_A(z)^2Y_{200} = 5.7 \pm 1.3 \times 10^{-8}\ h_{70}^{-2}$ Mpc^2. Finally, if we adopt the best-fit profile of Planck Collaboration et al. (2013a), who measured the SZ pressure profiles of 62 massive, low redshift clusters, we find a resulting value of $E(z)^{-2/3}D_A(z)^2Y_{200} = 8.7 \pm 2.0 \times 10^{-8}\ h_{70}^{-2}$ Mpc^2. This pressure profile parameterization is more extended than the fiducial Arnaud et al. (2010) profile, so a given estimate of the amplitude of the signal yields a larger value for the integrated Y parameter. Changing the pressure profile assumed represents the largest systematic shift in this value.

In summary, we find an integrated $E(z)^{-2/3}D_A(z)^2Y_{200} = 5.4 \pm 1.2^{stat} \pm 3^{sys} \times 10^{-8} h_{70}^{-2}$ Mpc^2 where we now include our approximate systematic uncertainty in the error budget.

To contextualize this result, in Figure 2.10, we plot the SZ amplitude signal determined as a function of mass along with the expected self-similar $Y - M$ scaling relation fit to mea-

surements of locally-bright galaxies with *Planck* data (Planck Collaboration et al., 2013b) as well as, at the highest masses, individually detected SZ clusters. This study represents a significant advance with respect to pushing the lower bound of the mass range at which the SZ effect has been observed with contemporaneous studies targeting $\sim 10^{14}\,\mathrm{M}_{\odot}$ systems (Hand et al., 2011; Planck Collaboration et al., 2011, 2013b; Sehgal et al., 2013).

However, the results are found to be broadly consistent with self-similar, purely gravitational expectations for the SZ amplitude which, in addition to the significant statistical and systematic uncertainties in this result, make it difficult to draw conclusions about the influence of the AGN on their host halos, despite the large amounts of mechanical and radiative energy these objects could potentially supply to their host halo gas.

Additionally, in Gralla & Crichton et al. (2014), we explore a similar stacked model of a subsample of radio galaxies with available spectroscopic redshifts from the catalog of Best & Heckman (2012). This subsample consists of 667 objects centered at a much lower redshift of $z \sim 0.3$ than is expected for the full sample (See Figure 2.2). This sample was found to have an SZ signal of $E(z)^{-2/3} D_A(z)^2 Y_{200} = 1.4 \pm 0.5^{stat} \pm 0.6^{sys} \times 10^{-7} h_{70}^{-2}\ \mathrm{Mpc}^2$. This result, while less significant of a detection than that of a the full sample, is greater in magnitude, than the results discuss above. This likely due to the fact that the masses of the host halos of these objects are, on average, expected to be greater than the much higher redshift halos of the full sample. The Mandelbaum et al. (2009) mass estimate, $M_{200} = 2.3 \pm 0.6 \times 10^{13}\ h_{70}^{-1} \mathrm{M}_{\odot}$, which is constrained with optically confirmed radio-loud AGN, and is the assumed mass we use for these systems throughout, is likely much more

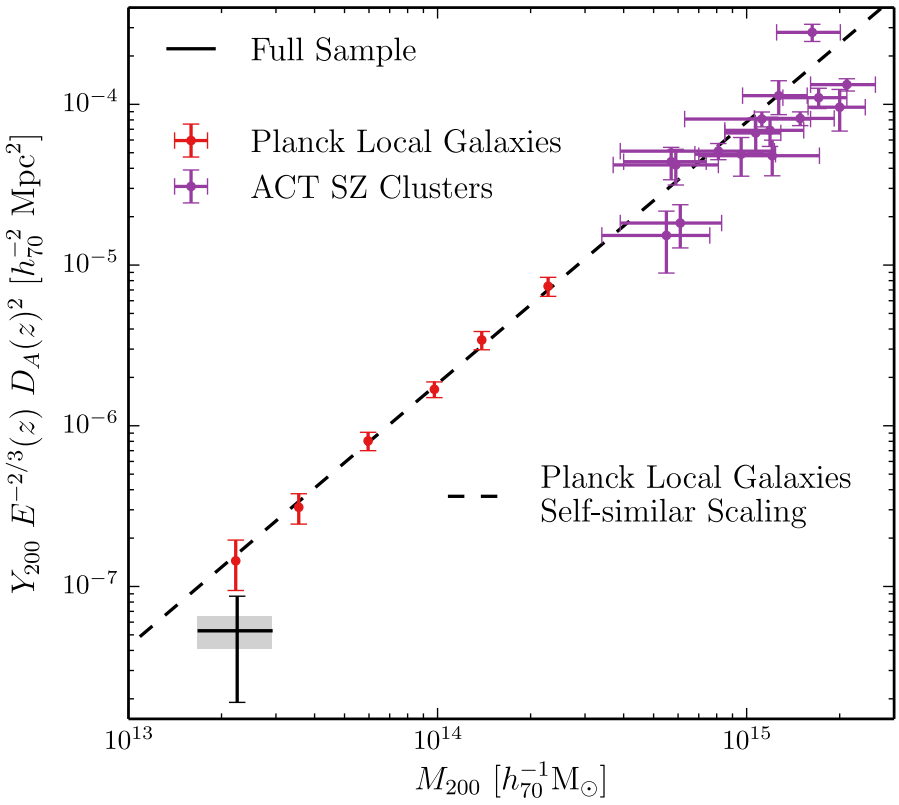

Figure 2.10: The SZ observable versus mass. The black point corresponds to the estimated integrated Y parameter that describes the SZ effect of halos hosting radio sources in the model that best fits our data. The mass value of the black point corresponds to the average mass of halos hosting similarly selected radio sources as determined from their weak lensing signal in Mandelbaum et al. (2009). The gray region indicates the statistical uncertainty on the SZ measurement, and the black error bar corresponds to the systematic uncertainty as estimated in Section 2.6.2. The purple data represent measurements for ACT SZ-detected galaxy clusters with dynamical mass measurements (Sifón et al., 2013). The red data indicate results from Planck Collaboration et al. (2013b) from measuring the SZ effect of local bright galaxies through stacking analyses, and the dashed line indicates the scaling relation derived in that study.

relevant for this spectroscopic sample, whereas, for our larger sample, it should be treated as an approximate upper limit in lieu of a more appropriate estimate.

2.7 Conclusion

Through a stacking approach using data from ACT and *Herschel*-SPIRE, we have measured the average radio to far-infrared SEDs of radio galaxies. The catalog, selected at 1.4 GHz from the FIRST and NVSS catalogs, comprises a large sample of radio sources spanning a broad redshift range out to $z \lesssim 4$. Empirically we find that the expected synchrotron spectrum of these sources (decreasing in flux as a function of frequency), is seen to display a spectral inversion in the millimeter and higher frequencies. We simultaneously modeling for synchrotron and dusty emission associated with these sources

Over and above this modeled emission, to explain the observed spectral inversion of the SEDs, we find evidence for the necessity of an additional component: the Sunyaev-Zel'dovich effect which we detect at the 5σ level for the first time in these systems. This spectral distortion of the CMB by intravening hot plasma, directly probes the thermal energy content of the ionized gas in the AGN host halos. In the context of physical models through which the accreting AGN shares and imparts energy upon the same gas that fuels star formation, measuring the impact of these systems on the thermodynamic state of their halo gas would be of great use to improving the empirical foundation of modern galaxy formation models. However, we find the amplitude of the SZ signal to be broadly con-

sistent with self-similar expectations from purely gravitational heating within the typically massive ($\sim 1 \times 10^{10}\,M_{\odot}$) AGN host halos, with no room to make statements about potential feedback effects within the statistical and systematic errors of this approach.

Chapter 3

The SZ Effect Associated with Quasar Feedback

Quasar feedback is a compelling means of sufficiently inhibiting star formation, bringing galaxy formation models into agreement with the observed decline of the bright end of the galaxy luminosity function (Croton et al., 2006; Thoul & Weinberg, 1995), as well as reheating the intracluster medium (e.g., Rawlings & Jarvis, 2004; Scannapieco & Oh, 2004). This picture is corroborated by the discovery that the masses of supermassive black holes (even outside of actively accreting scenarios) show significant correlations with the properties of the stellar bulges of their hosts (Ferrarese & Merritt, 2000; Gebhardt et al., 2000; Magorrian et al., 1998). An additional clue is the distinct similarity in the cosmic history of both star formation and black hole accretion rates (Boyle & Terlevich, 1998; Hopkins et al., 2008), which both peak at $z \sim 2$, before rapidly declining. Together these

observations suggest a scenario in which energy emitted by accreting black holes is able to energetically couple with the gas from which stars form (Hopkins et al., 2006). As this is likely the same gas which fuels the accretion of the black hole, such a process could additionally be self-regulating.

While radio-quiet quasars do not appear to have the same, mechanically powerful jets observed in radio galaxies, they can physically influence their surroundings through the extreme radiation pressure exerted on the accreting material (Murray et al., 1995; Proga et al., 2000). This material is rapidly accelerated into the surrounding medium, influencing the larger scale environment of the accreting system (Faucher-Giguère & Quataert, 2012; Nims et al., 2015; Zubovas & King, 2012). While the most central radiatively driven outflows are widely observed in radio-quiet quasars (Crenshaw et al., 2003; Gallagher et al., 2007; Reichard et al., 2003; Turnshek, 1984; Weymann et al., 1981), only in more modern studies have the larger scale, galaxy-wide outflows been detected (e.g. Arav et al., 2008; Greene et al., 2011; Liu et al., 2013a,b; Zakamska & Greene, 2014).

These winds are often modeled as a hot volume-filling plasma permeating through pockets of higher density material (Faucher-Giguère & Quataert, 2012; Zubovas & King, 2012). While the high density clumps are observed through emission lines, if sufficiently warm, the low-density, volume-filling component is more challenging to observe directly through emission. However, the Sunyaev-Zel'dovich effect is a promising avenue for constraining the influence this component on galactic scales. This effect, whose magnitude is proportional to the total thermal energy of the ionized gas along a line of sight (See

Section 1.3.1), allows us to constrain the thermal energetic output of these systems, which is not measurable otherwise. Additionally, in contrast with methods based on emission, as the SZ effect does not suffer from cosmic surface brightness dimming, we are able to efficiently probe systems out to high redshift.

In this study, we statistically search for the SZ effect of hot halos around a sample of radio-quiet quasars drawn from the Sloan Digital Sky Survey (SDSS, Eisenstein et al., 2011; Pâris et al., 2014; Schneider et al., 2010; York et al., 2000). Using millimeter to far-infrared data from ACT and *Herschel*-SPIRE (descibed in Sections 1.4 and 1.5), we detect the SZ signal with 3–4σ significance and find compelling indications for the feedback origin of this signal. This work is published in Crichton et al. (2016).

3.1 The SDSS Quasar Catalog

For this study we use the SDSS optical quasar catalogs derived from the spectroscopic quasar samples in Data Release 7 (DR7; Schneider et al., 2010) and Data Release 10 (DR10; Pâris et al., 2014). We select all quasars within the ACT equatorial survey, including any object present in both DR7 and DR10 only once. This combined catalog spans a wide range of redshift out to $z \sim 7$. As we will be performing a statistical analysis on this sample, we cut the catalog to lie within the well populated redshift range $0.5 < z < 3.5$, where 95% of the quasars are found. Due to the statistical nature of this work, the primary benefit of using a spectroscopic catalog is not the redshift precision it provides but

the robust identification of objects as quasars which the SDSS spectroscopic classification pipeline enables. We further cut this catalog by excising all quasars that lie within $2'$ of sources detected with significance $> 5\sigma$ in the ACT millimeter data. Detected ACT sources are typically extremely luminous blazars, local ($z \ll 1$) star-forming galaxies, or high-z lensed dusty star-forming galaxies (Marsden et al., 2014b). Due to their high millimeter fluxes and the manner in which the ACT maps are filtered, these objects may significantly contaminate the measured fluxes of nearby quasars. However, we find that neglecting this cut alters the stacked fluxes (see Section 3.2) by no more than 1σ. Extending the mask to $5'$ around detected sources produces a change in the stacked signal much smaller than the statistical uncertainties on these data.

The catalog obtained after these cuts contains 17,468 quasars (8,642 from DR7 and 8,826 from DR10). A subset of 3,833 of these objects additionally overlap with the *Herschel*-SPIRE HerS region. Figure 3.1 shows the redshift distribution of this quasar sample as well as the redshift distribution of those quasars that additionally overlap with the *Herschel*-SPIRE HerS region. The sharp increase in sources at $z > 2$ shown in Figure 3.1 is due to the BOSS selection in DR10. This evident non-uniformity of the sample's selection is mitigated in our results by binning in redshift as described in Section 3.2. We additionally construct estimates for the optical bolometric luminosity of each quasar in the sample by applying the bolometric correction from Richards et al. (2006b) as described in Section 3.5.1.

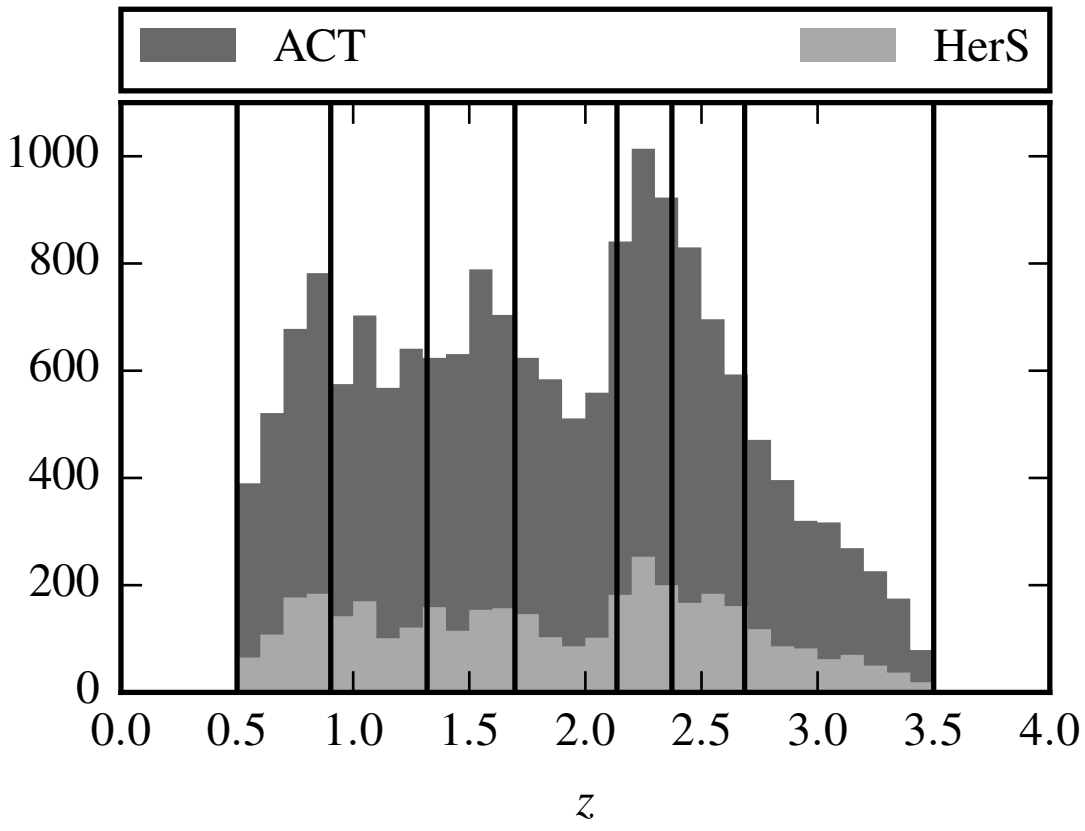

Figure 3.1: The redshift distribution of the combined SDSS DR7 and DR10 spectroscopic quasar sample falling within the ACT equatorial region ($-55^\circ \leq$ R.A. $\leq 58^\circ$, $-1.^\circ 5 \leq$ Dec. $\leq 1.^\circ 5$) after the radio loud cut has been applied. The histogram of the entirety of this sample is shown in dark gray and the subset which lies within the HerS region is shown in light gray. The vertical black lines denote the boundaries of the redshift bins we use for the stacking analysis.

3.1.1 Radio Loud Cut

As we are investigating the SZ effect associated with these sources, which is most prominent at millimeter wavelengths, we further cut this catalog to exclude potentially radio-loud quasars whose synchrotron emission could contaminate this signal. In Gralla & Crichton et al. (2014) (Chapter 2), this synchrotron emission dominated our modeled emission as the catalog in that study was selected from radio emission. In optically selected quasars synchrotron emission is expected to be significantly less luminous but none the less we narrow our selection to a radio-quiet sample. To do so, we perform a radio-quiet classification based on the methods of Xu et al. (1999). This study found a bimodal distribution in the ratio of AGN radio luminosity at 5 GHz and [OIII] 5007 Å line luminosity (an orientation insensitive measure of the AGN intrinsic luminosity) and defines a cut based on this bimodality. We derive an empirical proxy for the [OIII] 5007 Å line luminosity, $L_{[\mathrm{OIII}]}$, required for this cut by using the the mean relation found in Reyes et al. (2008) between $\mathcal{M}_{2500}$, the absolute magnitude at the rest-frame wavelength of 2500 Å, and $L_{[\mathrm{OIII}]}$. Here, as in Reyes et al. (2008), we use the SDSS i band absolute magnitude $\mathcal{M}_I(z=2)$ (Richards et al., 2006a) as a proxy for $\mathcal{M}_{2500}$, which is valid for $z \sim 2$. To determine the radio luminosities, we use the matched 1.4 GHz fluxes obtained from the Faint Images of the Radio Sky at Twenty-cm (FIRST; Becker et al., 1995) survey that are included in the DR7 and DR10 quasar catalogs. These 1.4 GHz radio fluxes are related to $L_{5\mathrm{GHz}}$ using the catalog redshifts and assuming a synchrotron spectrum, $L_\nu \propto \nu^{-1}$. This radio-loud cut shifts the stacked fluxes (as described in Section 3.2) in the 148 and 218 GHz ACT bands by at most

1σ in any redshift bin and reduces the sample size by 412 (2%). This cut removes the majority of sources that are detected by the FIRST survey. Applying stricter and less model dependent cuts on the radio luminosities is found to have a negligible effect (to within the statistical errors) on our results.

3.2 Stacked Quasar Spectral Energy Distributions

The typical submillimeter and far-infrared flux densities of optically selected quasars are found to be significantly less than the detection limits of the ACT and *Herschel*-SPIRE data. We therefore employ a stacking analysis to measure the ensemble flux densities associated with the quasars. Stacking can be shown to be an unbiased maximum likelihood estimator of the mean flux density of a catalog in both the case of a Gaussian noise background, as is the case for the point source-filtered ACT data, or for confusion-limited data such as the *Herschel*-SPIRE data employed in this work (Marsden et al., 2009; Viero et al., 2013, and Appendix A).

Due to both the non-uniform selection of our sample in redshift and the strong redshift dependence of our estimated bolometric luminosities (See Figs 3.1 and 3.6), we choose to bin the quasar catalog by redshift prior to stacking. This additionally allows us to account for the redshift dependence of the parameters of the models to be fit. We choose these bins such that they each contain approximately equal numbers of sources. For the seven redshift

bins thus chosen, we have approximately 2430 quasars per bin. The boundaries of these bins are shown as the vertical lines in Figures 3.1 and 3.6. As the catalog was selected to lie within the ACT equatorial region all of these objects contribute to the stacks for the 148, 218 and 277 GHz bands. For the 600, 857 and 1200 GHz *Herschel*-SPIRE bands the number of quasars that contribute is further diminished by the band dependent masks which account for varying sky coverage of the data. The smaller sky coverage of the HeRS survey results in 506–574 quasars per bin with submillimeter data.

For each of the redshift bins, we construct the stacked signal in a band by taking the inverse variance weighted average of the measured flux density corresponding to each source in the bin:

$$\bar{d}_{\nu}^{b} = \frac{\sum_{i}^{N^b} w_{i,\nu} d_{i,\nu}}{\sum_{i}^{N^b} w_{i,\nu}}. \tag{3.1}$$

This yields the stacked signal $\bar{d}_{\nu}^{b}$ of the redshift bin b containing N^b sources, each contributing flux density $d_{i,\nu}$ in the band corresponding to a frequency ν. The inverse variance weights $w_{i,\nu}$, which vary from source to source and between bands, are determined from the error maps for each data set. For the *Herschel*-SPIRE data, these error maps are derived from the diagonal component of the pixel-pixel covariance matrices that are a product of the map making pipeline (Patanchon et al., 2008). For the matched filtered ACT data, we take the variance in a pixel for a given band to be inversely proportional to the value of that band's hits-count map at that location. The flux density contributions $d_{i,\nu}$ of each source are taken from the pixel values at the location of each object in our catalog. These values are corrected for the averaging effects of each map's pixelization scheme.

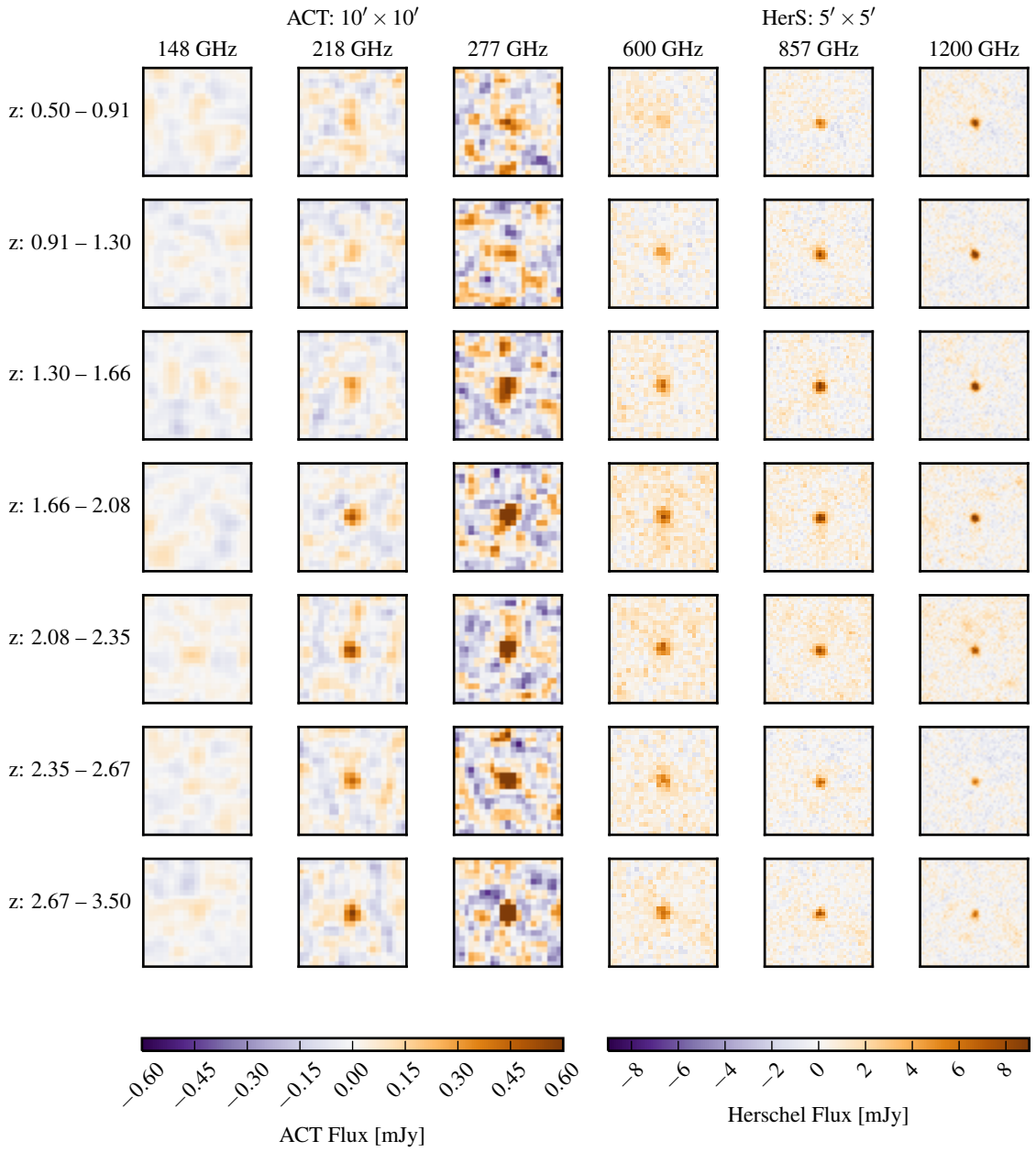

Figure 3.2: Weighted average thumbnail images around the quasar positions in $10' \times 10'$ stamps for the matched filtered ACT data (left three columns) and $5' \times 5'$ stamps for the *Herschel*-SPIRE data (right three columns). The observed signal is dominated by the dust emission associated with quasars. Since no background aperture has been subtracted from the *Herschel*-SPIRE data here, large scale excess positive signal, associated with correlated cosmic infrared background emission, is visible.

The uncertainties on the stacked flux densities, σ_ν^b ,are determined through a bootstrap analysis which resamples, with replacement, the sources contributing to each bin. We then calculate the uncertainties by taking the standard deviation of the stacked flux densities measured for each of the resamples. The bootstrapped uncertainties thus determined are found to be within 10% of the standard errors on the mean of each of the binned catalogs. Table 3.1 shows the resulting stacked flux densities in each band and redshift bin. Thumbnail images of each of these stacks are shown in Figure 3.2.

We perform null tests on the stacked signal by randomly drawing catalogs using positions uniformly distributed over the sky coverage of the ACT equatorial data. The stacking procedure is otherwise left unchanged with identical masks applied, producing similar numbers of null sources with *Herschel*-SPIRE data as we have in our quasar catalog. We run 500 of these null stacks, each using a catalog of the same size as a single one of our redshift bins. The mean stacked fluxes of these null tests are found to be consistent with zero with no detectable bias across all bands. Testing against the hypothesis of no stacked signal, we obtain a $\chi^2 = 6.2$ with 6 degrees of freedom (one for each band) yielding a probability to exceed (PTE) of 0.40.

Stacking analyses are subject to bias undetectable through null tests if there exist sources in the data that are significantly correlated with the catalog that is being used for the stack. Wang et al. (2015) have detected a correlation between SDSS optically selected quasars and the cosmic infrared background over the same redshift range as the sample we are studying using *Herschel*-SPIRE data. Additionally, some excess large scale emission is

Table 3.1: Stacked quasar flux densities for the ACT (148–277 GHz) and *Herschel*-SPIRE (600–1200 GHz) data.

Bin	z range	N^{b} †	$\bar{d}^{b}_{148\ \mathrm{GHz}}$ (mJy)	$\bar{d}^{b}_{218\ \mathrm{GHz}}$ (mJy)	$\bar{d}^{b}_{277\ \mathrm{GHz}}$ (mJy)	$\bar{d}^{b}_{600\ \mathrm{GHz}}$ (mJy)	$\bar{d}^{b}_{857\ \mathrm{GHz}}$ (mJy)	$\bar{d}^{b}_{1200\ \mathrm{GHz}}$ (mJy)
1	0.50–0.91	2432 (545)	0.06 ± 0.04	0.26 ± 0.07	0.6 ± 0.16	1.4 ± 0.8	5.7 ± 0.7	10.2 ± 0.8
2	0.91–1.30	2435 (518)	0.03 ± 0.04	0.22 ± 0.07	0.4 ± 0.16	4.0 ± 0.9	7.2 ± 0.8	10.0 ± 0.9
3	1.30–1.66	2431 (506)	0.09 ± 0.04	0.33 ± 0.07	0.8 ± 0.16	5.9 ± 0.9	9.9 ± 0.9	13.1 ± 1.0
4	1.66–2.08	2434 (482)	0.05 ± 0.04	0.51 ± 0.07	1.3 ± 0.16	7.6 ± 0.9	9.5 ± 0.8	10.5 ± 0.9
5	2.08–2.35	2432 (546)	0.11 ± 0.04	0.57 ± 0.07	1.3 ± 0.17	5.0 ± 0.8	6.9 ± 0.8	6.8 ± 0.7
6	2.35–2.67	2436 (574)	0.07 ± 0.04	0.44 ± 0.07	1.2 ± 0.17	4.5 ± 0.7	6.2 ± 0.7	6.6 ± 0.7
7	2.67–3.50	2434 (564)	0.12 ± 0.05	0.59 ± 0.07	1.8 ± 0.17	5.1 ± 0.7	7.3 ± 0.7	6.5 ± 0.8

† Numbers in parentheses are the bin counts which overlap the HerS region.

clearly visible in the *Herschel*-SPIRE stacked data shown in Figure 3.2. To reduce the bias arising from this contaminating emission in these bands we perform an aperture photometry background subtraction using the mean flux in a tight annular aperture with inner and outer diameters of 2 and 3.2 beam FWHM, respectively, for each of the 600, 857 and 1200 GHz bands. This subtraction amounts to an average correction of $\lesssim 1$ mJy (10–25%) for the *Herschel*-SPIRE stacked fluxes. An analogous background subtraction is effectively provided by the matched filter applied to the ACT data.

3.3 Modeling for Quasar Emission

The far-infrared SEDs of quasars hosts are thought to be dominated by dusty graybody emission produced from the re-radiated thermal emission of dust grains heated by contributions from both the luminous quasar itself and ongoing star forming activity within the quasar hosts (e.g. Kirkpatrick et al., 2012). We therefore construct an SED model for the quasars with a component from both this emission and a contribution from the SZ effect which we are attempting to detect. In contrast with the study of radio selected objects in Chapter 2 (Gralla & Crichton et al. (2014)), we do not model for the synchrotron emission. As we have selected a radio-quiet sample, such emission should be subdominant ($<< 1\,\mathrm{mJy} \cdot (150\,\mathrm{GHz}/1.4\,\mathrm{GHz})^{-1} \approx 0.01\,\mathrm{mJy}$) in the millimeter at the $\sim$0.1 mJy scale flux densities we are sensitive to.

3.3.1 Constructing Stacked Models of the Quasar SED

Our model for the stacked quasar spectral energy distribution (SED) has two components: a graybody dust spectrum and a contribution from the SZ effect. We parameterize the mean quasar dust spectrum in terms of the rest frame frequency ν as

$$S_{\rm dust}(\nu, z, L_{\rm ir}, \beta, T_{\rm d}) = \frac{L_{\rm ir}}{4\pi D_{\rm L}^2(z)} \frac{((1+z)\nu)^\beta B_{(1+z)\nu}(T_{\rm d})}{\int \nu'^\beta B_{\nu'}(T_{\rm d}) {\rm d}\nu'}, \tag{3.2}$$

representing a modified (optically thin) blackbody spectrum at a temperature $T_{\rm d}$ with emissivity β. The integral in the denominator is taken from 300 to 21 THz (14 μm to 1000 μm) in the rest frame such that $L_{\rm ir}$ is representative of the infrared bolometric luminosity of the quasar. We use the quasar's redshift and corresponding luminosity distance, $D_{\rm L}(z)$, to derive the model SED in terms of the observed-frame flux density.

In contrast to the simple empirical amplitude, $A_{\rm SZ}$ at 148 GHz, used to parameterize the SZ signal in Gralla & Crichton et al. (2014) and as discussed in Section 2.4, here we model the contribution of the SZ effect in terms of the volume integrated thermal pressure of the electron gas, $\int p {\rm d}V = \int n_{\rm e} T_{\rm e} {\rm d}V$. Integrated over the solid angle of a source, the SZ effect makes a contribution to the observed flux density with the form (see Section 1.3.1)

$$S_{\rm SZ}(\nu, z, \int p {\rm d}V) = I_0 g(\nu) \frac{\sigma_{\rm T}}{m_{\rm e} c^2} \frac{\int p {\rm d}V}{D_{\rm A}^2(z)}. \tag{3.3}$$

Here, $I_0 = 2(k_{\rm B}T_{\rm CMB})^3/(hc)^2$ and the SZ spectral function is

$$g(x \equiv h\nu/k_{\rm B}T_{\rm CMB}) = \frac{x^4 e^x}{(e^x-1)^2}\left(x\frac{e^x+1}{e^x-1}-4\right), \tag{3.4}$$

the non-relativistic form of the SZ spectrum. With the levels of SZ measured in this work, the associated temperature for a thermalized medium is approximately 1 keV which would lead to relativistic corrections of 1–2 percent (Fabbri, 1981; Rephaeli, 1995). Additional SZ signal could originate from a smaller, hot relativistic plasma that is not in thermal equilibrium with the larger circumgalactic medium, however, the sensitivity and spectral resolution of our measurements do not allow us to explore this possibility.

The quantity $\int p{\rm d}V$ used here represents only the volume integrated thermal pressure of the electron gas that can be directly related to the total thermal energy through

$$E_{\rm th} = \frac{3}{2}\left(1+\frac{1}{\mu_{\rm e}}\right)\int p{\rm d}V, \tag{3.5}$$

where we take the mean molecular weight per free electron to be $\mu_{\rm e} = 1.14$.

These dust and SZ contributions are combined to form the full model SED for each quasar,

$$S_{\rm tot} = S_{\rm dust}(\nu, z, \beta, L_{\rm ir}, T_{\rm d}) + S_{\rm SZ}(\nu, z, \int p{\rm d}V). \tag{3.6}$$

For each quasar i in a redshift bin b we use the inverse-variance weights from the data

to construct the stacked model SED,

$$\bar{S}_\nu^b = \frac{\sum_i^{N^b} w_{i,\nu}\, S_{\rm tot}(\nu, z_i, \int p\mathrm{d}V_i, \beta, L_{\rm ir}^b, T_{\rm d})}{\sum_i^{N^b} w_{i,\nu}}. \tag{3.7}$$

The graybody parameters may exhibit significant redshift evolution. We fit for $L_{\rm ir}$ independently in each redshift bin b while $T_{\rm d}$ and β are fit globally, each with a single value across all the redshift bins. We find that allowing $T_{\rm d}$ to vary independently across the bins results in consistent temperatures for all bins and tends to produce χ^2 values which are indicative of overfitting. We address other approaches for modeling dust emission in Section 3.5.3.

We use two approaches for modeling the SZ effect. The first approach uses $\int p\mathrm{d}V$ directly as a parameter, with a single value fit across all of the redshift bins such that $\int p\mathrm{d}V_i$ takes on the same value for each quasar. This method produces an estimate for the average thermal energy in ionized gas associated with quasars across our entire redshift range. This model will be referred to as the "$\int p\mathrm{d}V$ model." Our second approach is motivated by the hypothesis that such a signal would be dominated by energy injected into the surrounding medium by quasar feedback. In this scenario, assuming that cooling is negligible over the time scales in question, the thermal energy output from quasar feedback is

$$E_{{\rm th},i} = f L_{{\rm bol},i} \tau. \tag{3.8}$$

Here $L_{{\rm bol},i}$ is the optically-derived bolometric luminosity of the ith quasar (determined as

described in Section 3.5.1) and f is the efficiency with which this radiative energy is able to thermally couple to the surrounding gas over the period of active quasar activity prior to observation, τ. We then fit the efficiency f as a parameter in the model and use this to scale the value of $\int p \mathrm{d}V_i$ used to generate the SED for each quasar (given its $L_{\mathrm{bol},i}$) in Equation 3.6 by making use of Equation 3.5. As this efficiency is degenerate with τ in determining $\int p \mathrm{d}V_i$, we normalize τ to a fiducial active period of $\tau = \tau_8 \times 10^8$ yr and report our value for the efficiency f in units of τ_8^{-1} percent. We refer to this model as the "quasar feedback" model.

3.3.2 Results of Modeling the Quasar SED

To constrain the parameters in the models described in Section 3.3, we construct a Gaussian likelihood function,

$$\ln \mathcal{L} \propto -\frac{1}{2} \sum_b (\vec{d}^b - \vec{S}^b)^{\mathrm{T}} \mathsf{C}_b^{-1} (\vec{d}^b - \vec{S}^b). \tag{3.9}$$

Here, $\vec{d}^b$ an $\vec{S}^b$ are vectors of the stacked data and model fluxes respectively with each element corresponding to a separate band. The covariance matrices C_b are determined by combining the bootstrapped stacked flux uncertainties, σ_ν^b, with the calibration uncertainties and covariances for the individual data bands discussed in Sections 1.4 and 1.5.

This likelihood is then maximized using an affine invariant Markov chain Monte Carlo (MCMC) ensemble sampler algorithm (EMCEE, Foreman-Mackey et al., 2013). We choose

Table 3.2: Marginalized parameter constraints for the quasar feedback model

z range	$\log_{10}(L_{\rm ir}^b/L_\odot)$	$T_{\rm d}$ (K)	β	f (τ_8^{-1} percent)
0.50–0.91	11.40 ± 0.06	$40.68^{+3.17}_{-2.70}$	$1.12^{+0.13}_{-0.12}$	$14.5^{+3.3}_{-3.1}$
0.91–1.30	11.66 ± 0.05			
1.30–1.66	11.95 ± 0.05			
1.66–2.08	12.06 ± 0.04			
2.08–2.34	12.05 ± 0.04			
2.35–2.67	12.04 ± 0.05			
2.67–3.50	12.19 ± 0.05			

to use unbounded uniform priors for the parameters, $L_{\rm ir}^b$ and $T_{\rm d}$. For the parameters β, $\int p{\rm d}V$ and f we again use uniform priors but restrict these parameter values to be strictly positive in order to avoid unphysical degeneracies. We test for convergence of the chains to the posterior distribution by evaluating their autocorrelation times relative to the length of the sampled chain. All best-fitting parameter constraints are reported as their 50th percentiles when marginalized over all other parameters in the posterior distribution. The uncertainties are determined by the marginalized 68 percent credible regions around these values. We calculate χ^2 values as $-2\ln\mathcal{L}_{\rm max}$ where $\ln\mathcal{L}_{\rm max}$ is calculated with a conjugate-gradient optimization algorithm initialized at the best-fitting parameter locations from the MCMC chains.

Using the models outlined in Section 3.3.1, we fit the parameters β, $L_{\rm ir}^b$, $T_{\rm d}$ and either $\int p{\rm d}V$ or f, where the b index labels each of our seven redshift bins.

For the $\int p{\rm d}V$ model, we find that the data are fit well with $\int p{\rm d}V = (2.2 \pm 0.6) \times 10^{60}$ erg, which corresponds to a total thermal energy of $E_{\rm th} = (6.2 \pm 1.7) \times 10^{60}$ erg (using Equation 3.5). The fit yields χ^2 = 36.3 for 32 degrees of freedom, resulting in a PTE

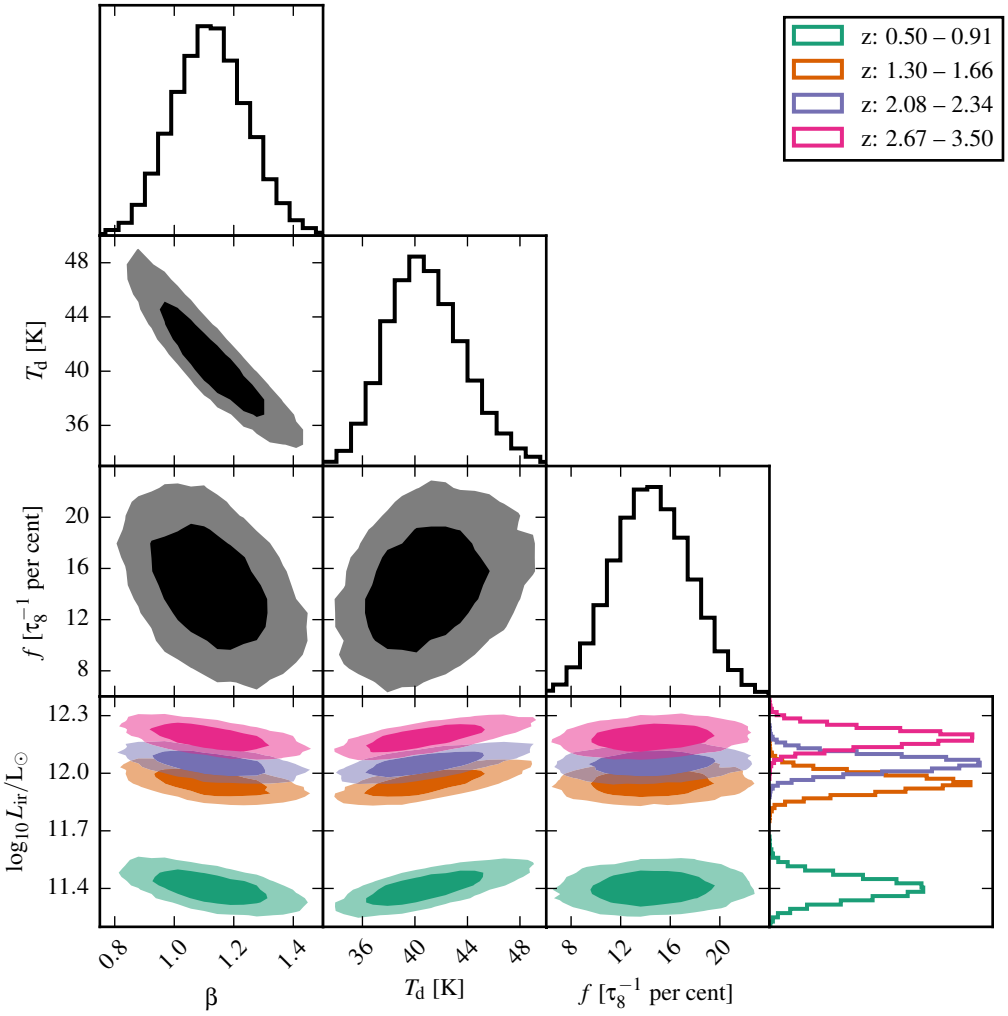

Figure 3.3: Contours of the 68 and 95 percent credible intervals of the parameters for the quasar efficiency model in dark and light shades respectively. The histograms display each parameter's marginalized posterior distribution. Parameters f, β and T_d are fit globally across all redshift bins. For the other parameters each color indicates the constraints from a single redshift bin. For clarity, we show the bin dependent parameters for a subset of the redshift bins used.

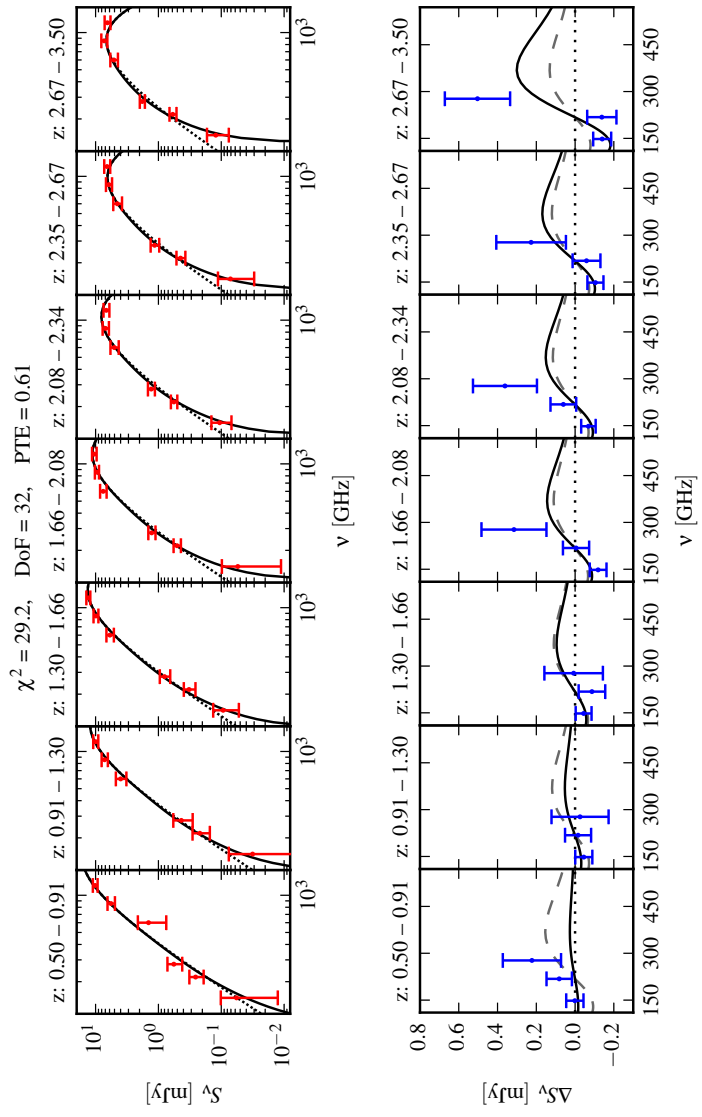

Figure 3.4: Top: stacked millimeter to infrared SEDs. Red data points represent the stacked data in our bands spanning 148–1200 GHz. The best-fitting stacked SEDs for the quasar feedback model for each redshift bin are shown in the solid black lines. The dotted black lines show the stacked model with no SZ effect. Bottom: dust subtracted millimeter SEDs highlighting the fit to the SZ component. The dust subtracted data are shown as the blue data points and the solid black lines represent the SZ component of the quasar feedback stacked model. The dashed gray lines show the best-fitting SZ component when parameterized using the $\int pdV$ formalism. The $\Delta S_\nu = 0$ line, corresponding to a dust only signal is shown as the dotted black line. All errorbars shown here are statistical only and do not include the calibration uncertainties and covariances that are accounted for in the modeling.

of 0.28. For the quasar feedback model, we find $f = (14.5 \pm 3.3)\tau_8^{-1}$ percent with χ^2 = 29.2 for 32 degrees of freedom, corresponding to a PTE of 0.61. Both of these models produce consistent best-fitting values for all the other parameters. For the quasar feedback model, the 68 and 95 percent credible intervals for all the fit parameters are shown in Figure 3.3 and their marginalized constraints are summarized in Table 3.2. The numbers in this table refer to the median of the marginalized parameter posteriors and the boundaries of their 68 percent credible intervals. The maximum likelihood stacked SEDs from this model are shown along with the data in Figure 3.4. In the lower plot of Figure 3.4 we show the ACT data residuals, after subtracting the modeled dust SED. Overplotted is the best-fitting modeled SZ component. Both the $\int p\mathrm{d}V$ and quasar feedback models are shown. In Figure 3.5 we show the ACT data after subtracting the best fit dust emission model combined over all the redshift bins so that the significance of the SZ detection is more easily visualized than in Figure 3.4.

These fits provide evidence for the presence of hot thermalized gas associated with these systems manifesting itself through an SZ distortion at millimeter wavelengths. A fit to the data explicitly neglecting the SZ component is formally worse than both of the above models with χ^2 = 51.0 and 33 degrees of freedom. We therefore observe a $\Delta\chi^2$ improvement of 14.7 for the $\int p\mathrm{d}V$ model and 21.8 for the quasar feedback model, both of which add one additional parameter. This corresponds to 3σ evidence for the presence of associated thermalized gas or, assuming the quasar feedback scenario, 4σ evidence for the thermal coupling of quasars to their surrounding medium.

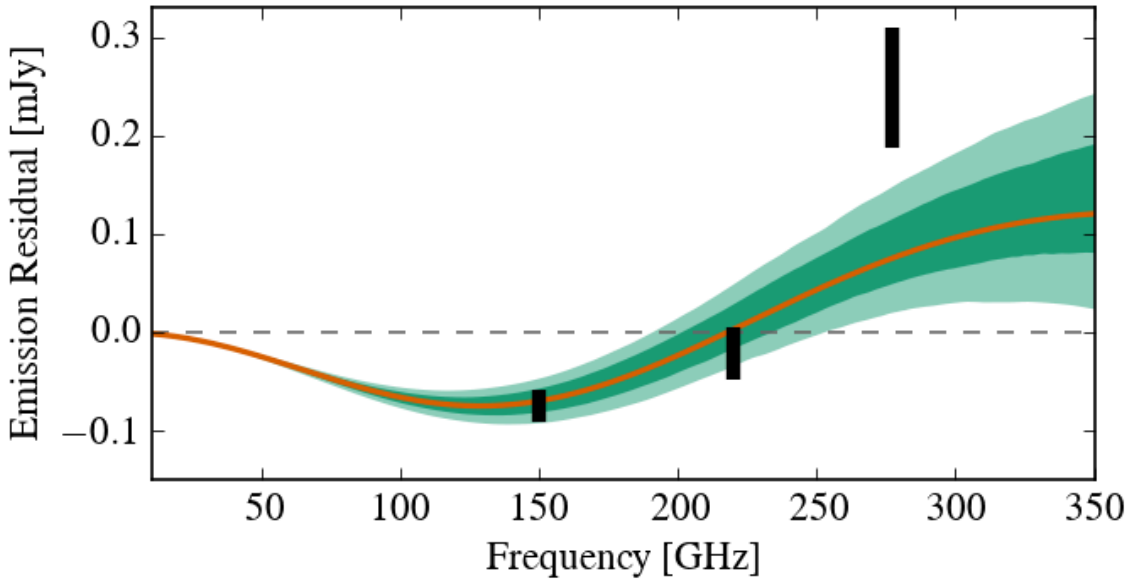

Figure 3.5: The residual millimeter signal after subtracting the best fit dust emission model. The black data points show the stacked ACT data after subtracting the best fit emission signal and averaging over all redshift bins and their statistical uncertainties. The orange line shows the best fit SZ signal spectrum while the dark and light green regions represent the 68 and 95% uncertainties in the dust subtraction propagated from the posterior distribution of dust model parameters in the MCMC chains. The errorbars shown are statistical only and do not include the calibration uncertainties and covariances that are accounted for in the modeling.

We find the best-fitting models require significant evolution of $L_{\rm ir}$ across the redshift range we probe, spanning the range $10^{11.4-12.2}$ $L_\odot$. The implications of this measurement are discussed in Section 3.3.3. Fitting for a single temperature across all redshift bins, we find $T_{\rm d} = 40 \pm 3$ K. Allowing the dust temperatures to vary independently for each redshift bin yields values all consistent with this globally fit temperature and shows no detectable sign of redshift evolution.

The best fitting value of the dust emissivity index β is found to be 1.12 ± 0.13. Such a low value of the dust emissivity index is not precluded from the theoretically allowed range of $1 < \beta < 2$ but is approaching the low end of indices commonly observed in galactic and extragalactic emission. We further discuss this result in Section 3.3.4. The combination of this observation and the systematic dependence of our results on the chosen form of the dust model leads us to explore a range of alternative dust models described extensively in Section 3.5.3. These include dust models with values of β fixed to values more commonly seen in the literature, as well as composite two temperature models and models with an optically thick dust spectrum. In summary, we find that a model with β fixed to 1.6 produces an acceptable fit (PTE=0.16) to the data with 3σ evidence for the SZ effect. A model with β fixed to 1.8 does not fit the data well (PTE=0.01). Motivated by increasing evidence that high redshift dusty galaxies are characterized by an optically thick dust emission (Huang et al., 2014; Riechers et al., 2013), we evaluate a model with an optically thick dust component. This optically thick model fits the data (PTE=0.69) with $\beta = 1.3 \pm 0.3$ and 4σ evidence for SZ. A two-temperature model adequately fits the data (PTE=0.35)

with $\beta = 1.4 \pm 0.1$ (for both graybody components) and no SZ component. However, this model comes at the cost of significant additional model complexity in the form of seven additional parameters.

Our data and modeling results establish that the far-infrared and millimeter SEDs of radio-quiet quasars are dominated by dust emission and require at the 3–4σ level an SZ distortion for most dust emission models. In the subsequent sections we physically interpret the results of this modeling.

3.3.3 Infrared Luminosity and Star Formation Rates of Quasars

Our models provide estimates of the far-infrared luminosity of quasars through the $L_{\rm ir}^{b}$ parameters fit to our data in each redshift bin. The far-infrared emission associated with quasars originates from warm dust that is heated by ultraviolet radiation from young stars as well as the quasar itself. In the absence of detailed mid-infrared data, these contributions are difficult to separate. In a previous study, Kirkpatrick et al. (2012) quantify the percentage contribution due to star formation in these systems, finding 21 and 56 percent of the far-infrared bolometric luminosity is due to star formation at $z \sim 1$ and 2, respectively. We do not try to separate the contributions from star formation and the quasar emission here, estimating only upper limits on the star formation rates of quasar hosts based on assuming all the far-infrared bolometric luminosity is associated with star formation. To estimate

the total infrared luminosity of star formation, $L_{\rm ir}^{\rm SF}$, we use the relationship between total $L_{\rm ir}^{\rm SF}$ and rest-frame 160 µm luminosity, L_{160} from Symeonidis et al. (2008). For the redshift range we probe, this rest-frame frequency falls within the frequency coverage of our data. Using total $L_{\rm ir}^{\rm SF}$ calculated from L_{160} values derived from the best-fitting SED models for each redshift bin, we obtain average star formation rates using the relation from Bell (2003). Our modeled far-infrared SEDs are consistent with the average star formation rates of quasar hosts being at most $\sim 60,\ 250$ and 400 $\mathrm{M}_{\odot}/\mathrm{yr}$ for $z \sim$1, 2 and 3, respectively.

3.3.4 Dust Emission Models

As discussed, for both SZ models, we find best-fit values of the dust emissivity for the fiducial optically-thin dust model to be $\beta = 1.12 \pm 0.13$ with a dust temperature (found to be insensitive to redshift bin) of $T_{\rm d} \approx 40$ K. While this temperature is consistent with other observations (Beelen et al., 2006; Dai et al., 2012), the dust emissivity index is lower than the values of $\beta \gtrsim 1.5$ typically observed in galactic and extragalactic dust emission. While these observations find β to differ among galaxies between the theoretical bounds ($1 \leq \beta \leq 2$, Bohren & Huffman, 1983), with observations peaking at $\beta = 1.5$ (Carico et al., 1992; Lisenfeld et al., 2000), leading to a common assumption for fitting *Herschel* data of $\beta = 1.5$ (e.g. Kirkpatrick et al., 2012). In perhaps the most relevant comparison with our work Beelen et al. (2006) find $\beta = 1.6 \pm 0.1$ in submillimeter studies of quasars.

Given the dependence of our results on accurate modeling of the dust emission, this warrants further investigation. In Section 3.5.3, we evaluate fits with alternative dust emis-

sion models with fixed emissivity, with optically thick emission, and with two dust components at different temperatures. We find that all models require a component with temperature $T_{\rm d} \approx 40$ K. However the dust emissivities of these alternative models tend toward higher values than our fiducial model, giving 68 percent credible regions with $\beta \lesssim 1.6$ and 95 percent credible regions with $\beta \lesssim 1.8$. There is observational evidence that the SEDs of high-z dusty star forming-galaxies are indicative of optically thick dust (Huang et al., 2014; Riechers et al., 2013). The precise origin of the dust emission of the quasar hosts is difficult to ascertain and the implicit assumption of dust optical depth $<< 1$ in our fiducial dust models may not be fully justified. Allowing for an optically thick graybody spectrum has the effect of broadening the dust peak and would manifest itself as an artificially lower β index when not accounted for. We explore this particular case in Section 3.5.5. We additionally note that values of $\beta = 1.3$, are observed by *Planck* in local star-forming galaxies (Negrello et al., 2013), consistent with spectral indices inferred by SPT in their high-z dust dominated source population (Mocanu et al., 2013). These observations are broadly consistent with the emissivity index we observe in our fiducial model.

3.4 Implications for Feedback Interpretation

In Section 3.3.2, we show that the data favor (at the 3–4σ level for most dust models) SED models for the stacked quasar sample with a thermal SZ contribution. We find that scaling this signal by the quasar bolometric luminosities, as expected if this energy is

sourced by quasar feedback, provides a good fit to the data and yields a quasar feedback heating efficiency of $f = (14.5 \pm 3.3)\tau_8^{-1}$ percent. Formally, this percentage is an upper limit because some of the thermal energy responsible for the SZ effect is due to simple virialization, which is not included in the feedback model. However in the following we argue that most estimates of quasar host halo masses imply that the contribution from virialization is subdominant. Furthermore we cannot separately constrain the heating efficiency f and the period of quasar activity τ. Quasar lifetimes are not well constrained (Martini, 2004), but we can use theoretical and observational estimates of quasar lifetimes from the literature to normalize our result to a fiducial value. Earlier observational estimates favored $\tau \lesssim 10^8$ yr (Gonçalves et al., 2008; Jakobsen et al., 2003; Martini & Weinberg, 2001; Schirber et al., 2004; Shen et al., 2007; Trainor & Steidel, 2013; Worseck et al., 2007) while more recent ones suggest $\tau \gtrsim 10^8$ yr (DiPompeo et al., 2014, 2015; Marconi et al., 2004), with values $\sim 10^8$ yr commonly suggested by models of galaxy formation (Hopkins et al., 2005a,b). As, on average, we should observe a given quasar halfway through its active lifetime, the period of activity prior to observation should be estimated as the typical quasar lifetime divided by two. In addition to being systematically dependent on this quasar lifetime estimate, the efficiency values we derive also depend on the accuracy of our estimates of the optical bolometric luminosities for the sample. The bolometric corrections used to derive these values (see Section 3.5.1) are uncertain at the 40 percent level. The luminosity scaling of this signal is further explored in Section 3.5.2.

In the literature, values of ∼5–7 percent efficiency in thermalizing quasar radiative

energy into the gas immediately around the accretion system are typically used in galaxy formation and evolution models (e.g., Hopkins et al., 2006; Springel et al., 2005). Feedback in this form and, with these efficiency values, has been shown to bring both simulated and semi-analytic models of self-regulating quasar feedback in line with the observed $M_{\rm BH}$–σ relation and quasar luminosity function (Di Matteo et al., 2005; Wyithe & Loeb, 2003). However, the thermalization efficiency obtained from such simulations depends acutely on the details of the feedback implementation (Choi et al., 2012; Ciotti & Ostriker, 2001; Novak et al., 2011). None the less, the modeled value of $f = (14.5 \pm 3.3)\tau_8^{-1}$ percent is approaching the values found in these studies and is broadly consistent with this paradigm.

While the quasar feedback model provides a compelling explanation for this SZ signal we also consider the possibility that this signal results in whole or in part from hot gas in virial equilibrium with the quasar host halos, a more typical manifestation of the SZ effect as seen in direct millimeter observations of galaxy clusters (e.g., Bleem et al., 2015; Hasselfield et al., 2013b; Planck Collaboration et al., 2016e). In our study of the SZ effect associated with radio-loud AGN, (Gralla & Crichton et al. (2014), Chapter 2) an SZ signal broadly consistent with that expected from the gravitationally shock heated ionized halos of the massive ($\gtrsim 10^{13}\,{\rm M}_\odot$) hosts was observed. While not precisely known, the halo masses of the quasars in this study are expected to be significantly lower in mass than the radio-selected sample and therefore the signal from purely gravitational heating is expected to be much lower. Galaxy-quasar clustering measurements at the lower limit of the redshift range we target ($z \sim 0.5$) yield quasar halo masses of $\sim 4 \times 10^{12} h^{-1} {\rm M}_\odot$ (Shen et al., 2013)

with a weak dependence of halo mass on quasar bolometric luminosity. Quasar-quasar clustering on the other hand yields a halo mass of $\sim 1 \times 10^{12} h^{-1} \mathrm{M}_{\odot}$ at $z = 2.4$ with no evidence for luminosity dependence (White et al., 2012). Wang et al. (2015) find that the cross-correlation signal between quasars and the CIB is well fit by a halo model for clustering corresponding to a host halo mass of $10^{12.36 \pm 0.87} h^{-1} \mathrm{M}_{\odot}$ for DR9 quasars with a median redshift of 2.5. The quasars in the latter two of these clustering studies were optically selected type 1 objects in the SDSS-III survey, and are thus comparable samples to that used in our work. Somewhat higher halo mass values $\gtrsim 5 \times 10^{12} h^{-1} \mathrm{M}_{\odot}$ are found in clustering studies of $z \gtrsim 2$ unobscured quasars by Richardson et al. (2012) and CMB lensing studies such as Sherwin et al. (2012) and DiPompeo et al. (2014, 2015). The latter two of these measurements are not directly comparable to the sample in this work as they are based on infrared-selected quasars with photometric redshifts.

Taking a range of $(1-5) \times 10^{12} h^{-1} \mathrm{M}_{\odot}$ we can estimate the expected magnitude of the SZ signal due only to the gravitationally heated virialized reservoirs of hot gas that would be associated with halos of this mass. Planck Collaboration et al. (2013b) find that the integrated SZ signal,

$$Y \equiv \int y \, \mathrm{d}\Omega = \frac{\sigma_{\mathrm{T}}}{m_{\mathrm{e}} c^2} \frac{\int p \mathrm{d}V}{D_{\mathrm{A}}^2(z)}, \tag{3.10}$$

of $z < 1$ quiescent galaxies closely traces the simple self-similar scaling with halo mass,

$$Y \, E^{-2/3}(z) \left(\frac{D_{\mathrm{A}}(z)}{500 \text{ Mpc}} \right)^2 = (2.9 \pm 0.3) \times 10^{-8} \mathrm{arcmin}^2 \left(\frac{M_{\mathrm{h}}}{10^{12} \mathrm{M}_{\odot}} \right)^{5/3} \tag{3.11}$$

down to a halo mass of $\sim 3 \times 10^{13} \mathrm{M}_{\odot}$. Broad agreement with this scaling relation is found in Gralla & Crichton et al. (2014) (Chapter 2) when comparing the magnitude of the SZ signal of the radio selected sample to the expected halo mass of radio-loud AGN hosts. The *Planck* study gives this relation using the quantities Y_{500} and M_{500}, defined with respect to a physical radius R_{500} enclosing a mean density of $500\rho_{\mathrm{c}}(z)$ (see also Le Brun et al., 2015). In Equation 3.11, we have accounted for a factor of $Y/Y_{500} \approx 1.8$, where Y corresponds to the total integrated SZ signal. This factor is calculated using the same universal radial pressure profile from Arnaud et al. (2010) as is used in Planck Collaboration et al. (2013b). A factor of $M_{\mathrm{h}}/M_{500} = 1.6$ is used, consistent with the conversion from M_{500} to M_{200} from the concentration relation of Duffy et al. (2008). This yields a closer proxy of the halo virial mass referred to here as M_{h}. We assume the entirety of the signal we observe is enclosed within the ACT beams such that Y, the total integrated signal is what our data constrain. This is a reasonable assumption as R_{200} for a $5 \times 10^{12} h^{-1} \mathrm{M}_{\odot}$ halo corresponds to $0\farcm4$ (within the ACT beam scales) at $z = 1.85$, the median redshift of our sample. Explicitly correcting for the band dependent beam dilution effect for an SZ signal of this scale would require a model dependent choice of SZ profile and result in corrections small relative to the measurement uncertainties (See Section 2.6). Combining Equations 3.10 and 3.11, we find

$$\frac{\int p \mathrm{d}V}{10^{60} \mathrm{erg}} \approx 0.011 \, E^{2/3}(z) \left(\frac{M_{\mathrm{h}}}{10^{12} \, \mathrm{M}_{\odot}} \right)^{5/3} . \tag{3.12}$$

While many of the assumptions made in deriving this relation may not strictly hold for quasar hosts, these arguments provide a rough estimate of the $\int p \mathrm{d}V$ signal one would

expect from purely gravitationally thermalized gas reservoirs hosted in these systems. For quasar halo masses in the range $(1-5)\times 10^{12}h^{-1}\mathrm{M}_{\odot}$ we find the expected level of this signal to be $\int p\mathrm{d}V = (0.4\text{–}5.8)\times 10^{59}$ erg at the median redshift of our catalog, $z = 1.85$. Thus these purely gravitational arguments under predict our measured result of $\int p\mathrm{d}V = (2.2\pm 0.6)\times 10^{60}$ erg making up at most $\sim$30 percent of the signal we observe, depending on the choice of halo mass. Given this amount of thermal energy the gas in these halos could either be gravitationally bound or unbound, again depending on the value taken for the halo mass.

The validity of this calculation is dependent on the details of the high-mass tail of the halo mass distribution of quasar hosts. Since, in the case of gravitational heating, the SZ contribution of each host halo is proportional to $M^{5/3}$, the effective mass that should be used in Equation 3.12 is $\langle M^{5/3}\rangle^{3/5}$ where the average is taken over the mass distribution of quasar host halos. How much higher this effective mass is compared to the halo masses we take from the literature depends on the behaviour of the high-mass tail of this distribution. As an example of how this can affect the interpretation of these results, we analytically approximate the average quasar host halo mass distribution of the $z\sim 1.4$ sample of the Richardson et al. (2012) clustering study. Using this approximation for the full mass distribution and calculating $\langle M^{5/3}\rangle^{3/5}$, we find that the effective mass scale corresponds to an expected signal from purely gravitational arguments of $\int p\mathrm{d}V \sim 4\times 10^{60}$ erg.

Unfortunately, the high-mass end of the quasar halo mass distribution, upon which this calculation relies, is not well constrained (Richardson et al., 2012; Shen et al., 2013). Shen

et al. (2013) find that data from clustering studies can be fit equally well by models with very different parameterizations for the mass dependence of the quasar halo occupation distribution, demonstrating the model dependent nature of results for halo mass distribution in the literature (including the relative contribution of correlated high-mass halos to these studies). We therefore do not attempt to correct for this in our primary discussion.

3.4.1 Comparison with Other Studies

Ruan et al. (2015) published a detection of quasar feedback in the *Planck* data at the level of $E_{\rm th} \sim 10^{62}$ erg, over an order of magnitude larger than one would expect from the physical arguments presented here and what we measure. This level of SZ effect is characteristic of the galaxy group mass scale and would leave a clear decrement at the level of several mJy around each quasar in 150 GHz data from ACT. Such a signal is challenged by both source studies, such as our own, and power spectrum studies with ACT data (Dunkley et al., 2013; Sievers et al., 2013). Furthermore, a thermal energy of 10^{62} erg would correspond to essentially 100 percent efficient feedback. Another issue with this level of $E_{\rm th}$ is that it greatly exceeds the binding energy ($E_{\rm b} \approx 2.5 \times 10^{59}$ erg $(M_{\rm h}/10^{12}$ M$_{\odot})^{5/3} E^{2/3}(z)$) of the host halos.

Verdier et al. (2016) and Soergel et al. (2017) have conducted additional *Planck* based studies since Ruan et al. (2015). These studies both find SZ signals of much lower magnitude than the values found in Ruan et al. (2015) and are broadly consistent with our results to within less than a factor of two in the case of Verdier et al. (2016) and to within the

statistical uncertainties of Soergel et al. (2017). However, it is difficult to directly compare our results with *Planck* based studies as the much coarser resolution of *Planck* means that the signals observed by these studies necessarily are more contaminated by structures correlated with the quasars on large physical scales. We directly observe (See Figure 3.2) correlated far-infrared emission on large scales the sub-$1'$ angular resolution of *Herschel*-SPIRE allows us to exclude from our modeling. With *Planck* data this is much more difficult and the consequences of this are apparent in the large disagreements in dust models from Verdier et al. (2016), Soergel et al. (2017) and our own work. As these dust models are additionally degenerate with the SZ constraints, we postpone detailed comparisons of our result to these studies to future work.

Cen & Safarzadeh (2015b) use a halo catalog from the *Millenium* simulation with analytic prescriptions for identifying quasar hosts (outlined in Cen & Safarzadeh (2015a)) and constructing an associated Compton-y map. Their study demonstrates that contaminating projected SZ signal from two halo correlations is important to account for in quasar stacking studies, particularly for large beam sizes, $\sim 10'$. This effect is less important for higher resolution, $\sim 1'$ (similar to the ACT beam scale), studies but may need to be modeled in future work. Additionally they find that such high-resolution studies may be promising in constraining models for the quasar halo occupation distribution. On a similar line, Dutta Chowdhury & Chatterjee (2017) find that fully incorporating the uncertainties involved with the halo occupation distribution of quasars broadens the uncertainties on the expected SZ signal such that gravitational heating could explain our results. Clearly progress in

understanding the gravitational signal needs to be made in the future for more sensitive studies to be able to make statements about energy injected through feedback.

3.5 Systematic Effects

A number of systematic considerations need to be taken into account in order to interpret the results of our modeling. The determination of the $L_{\rm bol}$, upon which our value for the feedback efficiency f systematically depends is discussed in Section 3.5.1. Additionally, the dependence of our SZ observable on the derived bolometric luminosities is investigated in Section 3.5.2. Systematic dependence of the results on our choice of dust emission model are explored in Section 3.5.3.

3.5.1 Optical Bolometric Luminosity Determination

As we investigate models that assume the thermal energy we observe through the SZ effect is dominated by converted quasar radiative energy (see the quasar feedback model described in Section 3.3), we require estimates for the optical bolometric luminosity, $L_{\rm bol}$, of each of the quasars in this sample. For this purpose we again make use of SDSS *i*-band absolute magnitudes, $\mathcal{M}_I(z=2)$ which are converted to rest-frame luminosities L_{2500} at 2500 Å and then to $L_{\rm bol}$ by applying the bolometric correction from Richards et al. (2006b). These estimated bolometric luminosities are shown in Figure 3.6. Since the DR10 survey was designed to target quasars at $z > 2$, its fainter magnitude limit ($i < 20.5$) yields an

increase in lower luminosity quasars at high redshift (Pâris et al., 2014) observed as the discontinuity at $z \sim 2$ in Figure 3.6.

Since the definition of our "quasar feedback" model parameter f depends directly on the $L_{\rm bol}$ values thus determined (see Equation 3.8), the results systematically depend on these bolometric correction factors. Richards et al. (2006b) find that these corrections vary in a systematic in a manner that depends on quasar luminosity and color. However, these variations within the observed quasar population are typically less than 15%. A more significant concern are the assumptions made in modeling the quasar emission in the construction of these estimates. An over estimation of these corrections can arise from double counting direct ultraviolet emission by also including re-radiated dust emission when integrating the SED. These effects are explored in Krawczyk et al. (2013) who, by restricting the integral of the SED to the range between 1 μm and 2 keV, find a bolometric correction of 2.75 from the 2500 Å monochromatic luminosity — significantly less than the value of 5 from Richards et al. (2006b) used in this work. Krawczyk et al. (2013) additionally explore a models and observations quasar spectra in the ultraviolet and X-ray, finding a range 2.75 and 5 for the 2500 Å bolometric correction. Furthermore, the studies of Marconi et al. (2004) and Elvis et al. (1994) find quasar bolometric corrections ranging from 3.6–5.1 and 3.6–7.3, respectively, when extrapolated to 2500 Å.

While we make use of the Richards et al. (2006b) bolometric correction we interpret these results from the literature as indicating that these values are still not known to better than 40 percent, a factor that systematically affects the interpretation of our SZ constraints

on quasar feedback.

3.5.2 Luminosity Dependence

The feedback interpretation of the SZ signal operates under the assumption that a fraction of the bolometric luminosity of these sources is being converted to thermal energy which we observe through the SZ effect. This therefore implies that the most bolometrically luminous sources should dominate in their contribution to our observed SZ distortion. This luminosity dependence is explicitly accounted for in the quasar feedback model but in this Section we explore an alternative means of measuring this dependence by evaluating the effect of luminosity cuts in the quasar catalog on the SZ amplitude extracted from fitting to the $\int p\mathrm{d}V$ model. Simply cutting the 8435 objects with optical bolometric luminosity $L_{\rm bol} > 1 \times 10^{46}$ erg (determined as described in Section 3.5.1) we find that the best-fitting $\int p\mathrm{d}V$ shifts from $(2.2 \pm 0.6) \times 10^{60}$ erg to $(1.3 \pm 0.6) \times 10^{60}$ erg. However, a naïve cut such as this may produce biased results as it significantly alters the sample's redshift distribution due to the strong redshift dependence of the optical bolometric luminosities (See Figure 3.6). We therefore perform a further test by selecting a range of redshift, $2.1 < z < 3.0$, over which the luminosity distribution remains qualitatively similar. The objects falling within this range are separated into two bins of bolometric luminosity, each of which is fit with a model including graybody dust and an SZ component parameterized through $\int p\mathrm{d}V$. We find that for the low luminosity bin ($L_{\rm bol} < 10^{46.3}$ erg) the best-fitting SZ amplitude is $\int p\mathrm{d}V = 2.2 \pm 1.1 \times 10^{60}$ erg, whereas for the $L_{\rm bol} > 10^{46.3}$ erg bin we find

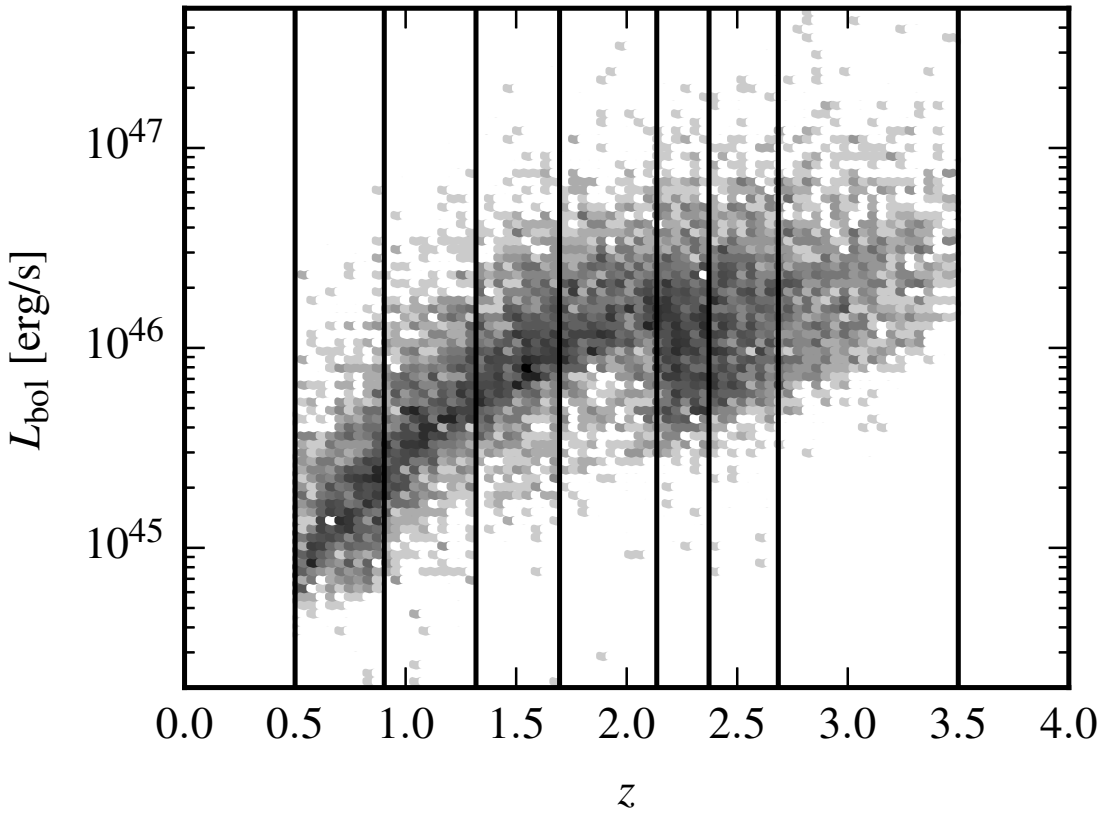

Figure 3.6: The optical bolometric luminosity–redshift distribution of combined SDSS DR7 and DR10 spectroscopic quasar sample falling within the ACT equatorial region ($-55^\circ \leq$ R.A. $\leq 58^\circ$, $1.^\circ5 \leq$ Dec. $\leq 1.^\circ5$) after the radio-loud cut has been applied. The density gray-scale used is logarithmic and the vertical black lines denote the boundaries of the redshift bins we use for the stacking analysis. The optical bolometric luminosity–redshift distribution of the subset of our sample which lies within the HerS region is found to be similar.

Table 3.3: Summary of fitting results for fiducial models as well as models with alternative dust treatments.

Model description	DoF	χ^2	PTE	$\Delta\text{DoF}_{\text{ref}}{}^a$	$\Delta\chi^2_{\text{ref}}{}^a$
Fiducial models					
Graybody only	33	51.0	0.02	0	0
Quasar feedback	32	29.2	0.61	1	21.8
$\int p\text{d}V$	32	36.3	0.28	1	14.7
Alternative quasar feedback models					
Fixed β [b]					
$\beta = 1.6$	33	41.8	0.14	0	9.2
$\beta = 1.8$	33	53.3	0.01	0	-2.3
Optically thick	31	26.7	0.69	2	24.3
Alternative dust only models					
Two temperature	26	28.1	0.36	7	22.9
Broken power law	31	39.4	0.14	2	11.6

[a] These values correspond to the reduction in degrees of freedom and χ^2 of each model with respect to the reference model which is the fit with no SZ effect and a single temperature graybody dust spectrum (the "Graybody Only" model).
[b] These models are found to still prefer non-zero values at the $\sim 3\sigma$ level in their marginalized constraints for the SZ amplitude. The negative $\Delta\chi^2_{\text{ref}}$ for the $\beta = 1.8$ model indicates it is a poorer fit than the reference graybody only model.

$\int p\text{d}V = 4.4 \pm 1.8 \times 10^{60}$ erg, again demonstrating a marginal shift to higher SZ amplitude for higher luminosity objects.

3.5.3 Alternative Emission Models

The significance of the SZ effect depends on the marginalization of the parameters of the assumed dust model in the fits. In this Section we explore some alternative dust models and report how the choice of dust model affects the SZ detection and the goodness of fit to the data. A summary of these fits to alternative models is provided in Table 3.3.

3.5.4 Fixed β models

In order to understand the effect of taking the dust emissivity index β as a free parameter in our fits, we attempt fits with the value of β fixed. As can be seen in Figure 3.3, there is degeneracy between the best-fitting value of β and the efficiency of quasar feedback, parameterized through f. A similar degeneracy is seen in the $\int p\mathrm{d}V$ model where, when fitting, the amplitude of the SZ signal is inversely proportional to the fit value for β. In Section 3.3.4 we noted that our fit value of β is on the low end of the theoretically allowed range of $1 \leq \beta \leq 2$, further motivating a check using models with values more commonly seen in the literature. We perform the same modeling of the stacked fluxes as described in Section 3.3 but instead of allowing β as a free parameter we hold its value fixed. We use the quasar feedback parameterization for the SZ effect here. Motivated by the results of Beelen et al. (2006) and Hardcastle et al. (2013) respectively, we fit models with β fixed to values of 1.6 and 1.8. As expected, these models produce worse χ^2 values than models in which β is a free parameter as shown in Table 3.3. The model with $\beta = 1.6$ provides an adequate fit to the data with a PTE of 0.14. The $\beta = 1.8$ model provides a considerably poorer fit with a PTE of 0.01. However, while detected at a lower amplitude ($f \approx 8.5\ \tau_8^{-1}$ percent) the marginal constraints on the SZ amplitude for both of these fixed β models prefer non-zero values at the $\sim 3\sigma$ level.

3.5.5 Optically Thick Model

We evaluate the effect of the assumption of dust optical depth $<< 1$ implicit in our fiducial dust SEDs by fitting the data with a model where we allow for an optically thick component. The corresponding dust SED for this optically thick model is

$$S_{\rm dust}(\nu, z, L_{\rm ir}, \tau_0, \beta, T_{\rm d}) = \frac{L_{\rm ir}}{4\pi D_{\rm L}^2(z)} \frac{\phi((1+z)\nu)}{\int \phi(\nu')\mathrm{d}\nu'}$$
$$\phi(\nu) = (1 - \mathrm{e}^{-\tau_0(\nu/\nu_{100\mu})^\beta}) B_\nu(T), \tag{3.13}$$

where $\nu_{100\mu}$ is defined such that τ_0 represents the dust optical depth at rest-frame wavelength of 100 µm. We fit the data with τ_0, β and $T_{\rm d}$ as the globally fit dust parameters and use the quasar feedback parameterization of the SZ effect. We find this model provides a good fit to the data (as summarized in Table 3.3) with $\chi^2 = 26.7$ for 31 degrees of freedom, corresponding to a PTE of 0.69. Constraints on the SZ effect, parameterized through f, are found to be unchanged. The dust opacity is not well constrained with $\log_{10}\tau_0 = 0.2^{+2.2}_{-0.5}$ but we find the expected positive correlation between dust optical depth and dust emissivity index β due to the broadening of the dust SED peak provided by the optically thick model.

The marginalized best-fitting emissivity index for this model is $\beta = 1.3 \pm 0.3$ and the dust temperature, $T_{\rm d} = 52 \pm 11$ K, is constrained to values centered higher but still consistent with those determined in the optically thin models.

3.5.6 Two Temperature Model

In this section, we examine whether the interpreted SZ distortion could instead be the result of an additional lower temperature dust component contributing to the SED at frequencies below the primary graybody peak. To test this, we attempt a model with no SZ component and a dust component that is made up of the sum of two graybody SEDs. Such models were found to be highly degenerate in the parameters describing the two dust components. To overcome some of this degeneracy we fix the temperature of the primary (high temperature) dust component to 40 K, consistent with what we find in the quasar feedback and $\int p\mathrm{d}V$ models. We then fit for a single value for the temperature of the cold dust component across all redshift bins, restricting it to be < 30 K with a truncated uniform prior. We fit the amplitudes of both components, parameterized through their infrared bolometric luminosity, $L_{\rm ir}$ as defined in Section 3.3, on a bin by bin basis. We find that the resulting best-fitting model provides a good fit to the data with a $\chi^2 = 28.1$ for 26 degrees of freedom, corresponding to the PTE of 0.35. The best-fitting value for the temperature of the cold dust component corresponds to 20 ± 3 K and the bolometric luminosities for this component range from $10^{10.7-11.4}$ $\mathrm{L}_{\odot}$, increasing with redshift. This two temperature model cannot be ruled out as an alternative explanation for the signal we observe. However (as shown in Table 3.3) this reduction in χ^2 of 22.9 with respect to the reference graybody dust only model comes at the expense of seven additional parameters, whereas both SZ models are significantly less complex, producing comparable χ^2 reductions for a single additional parameter. Applying the Bayesian information criterion (BIC), a test that explicitly penal-

izes additional model complexity, we find a ΔBIC improvement of >10. This corresponds to "strong evidence" against the preference of this two temperature model over the quasar feedback model based on this criterion.

3.5.7 Broken power-law Model

We additionally attempt fits using a dust model that has two emissivity indices, such that the dust spectrum takes the form of a broken power law at low frequencies.

The modeled dust spectrum then becomes

$$S_{\rm dust}(\nu, z, L_{\rm ir}, \nu_{\rm b}, \beta_0, \beta_1, T_{\rm d}) = \frac{L_{\rm ir}}{4\pi D_{\rm L}^2(z)} \frac{\phi((1+z)\nu)}{\int \phi(\nu')\mathrm{d}\nu'} \tag{3.14}$$

$$\phi(\nu) = \begin{cases} (\nu/\nu_{\rm b})^{\beta_0} B_\nu(T_{\rm d}) \text{ for } \nu \leq \nu_{\rm b} \\ \\ (\nu/\nu_{\rm b})^{\beta_1} B_\nu(T_{\rm d}) \text{ for } \nu > \nu_{\rm b} \end{cases}, \tag{3.15}$$

where $\nu_{\rm b}$ parameterizes the location of the spectral break with β_0 and β_1 parameterizing the emissivity index above and below this break respectively. We fit a model with only a dust component of this form to determine whether the SZ distortion we measure could instead be explained by such a spectrum. In this model, we fit single values for $\nu_{\rm b},\ \beta_0,\ \beta_1$ and $T_{\rm d}$ while the $L_{\rm ir}$ values are fit independently on a bin by bin basis. As shown in Table 3.3, the resulting χ^2 of 39.4 with 31 degrees of freedom (corresponding to a PTE of 0.14) indicates an adequate fit to the data. However, the best-fitting constraints on the emissivity indices are found to be $\beta_0 = 1.52^{+0.21}_{-0.25}$ and $\beta_1 = 0.25^{+0.18}_{-0.31}$ with the rest-frame spectral break at

$\nu_b = 1250^{+170}_{-210}$ GHz. This value for β_1 is well outside the theoretically allowed region of $1 < \beta < 2$, as discussed in Section 3.3.4, and therefore we reject this fit as less likely on physical grounds.

3.6 Conclusion

Using a stacking analysis of ACT and *Herschel*-SPIRE data with the SDSS spectroscopic quasar catalog we reconstruct millimeter and far-infrared SEDs of quasars spanning the redshift range $0.5 < z < 3.5$. We fit these data with a model for the stacked SED incorporating a dust component that is allowed to evolve as a function of redshift as well as an SZ distortion.

While the observed signal is dust dominated, we find 3–4σ for the thermal SZ effect associated with these systems for most dust models. In Section 3.5.3, we explore the effects of alternative dust parameterizations on this result. By fitting for the typical thermal energy associated with quasars, we find a best-fitting value of $E_{\rm th} = (6.2 \pm 1.7) \times 10^{60}$ erg. This exceeds, by almost an order of magnitude what would be expected for a gravitationally heated circumgalactic medium for the $(1-5) \times 10^{12} h^{-1} \mathrm{M}_{\odot}$ halos quasars are generally thought to occupy. However, if correct, the highest quasar halo mass estimates found in the literature could explain a large fraction of the observed SZ effect with purely gravitational heating. This observed SZ signal is found to be consistent with the scenario that this energy is being fuelled by quasar feedback in which up to $(14.5 \pm 3.3)\tau_8^{-1}$ percent of the quasar

radiative energy is thermalized in the surrounding medium. This picture is broadly consistent with the values of $\sim$5–7 percent efficiency typically employed by galaxy formation and evolution models (e.g., Hopkins et al., 2006; Springel et al., 2005), however, there are a number of systematic concerns in interpreting this result that are discussed in Section 3.5.

Forthcoming, deeper and wider ACT data will provide more precise estimates for the SEDs in the millimeter but without a better understanding of the halo masses and dust properties of high redshift quasar hosts, future studies will remain limited by associated systematics in the interpretation of the improved constraints.

Chapter 4

Pressure Profiles of SZ Selected Galaxy Clusters

4.1 Introduction

Galaxy clusters are the largest structures in the universe to have gravitationally relaxed. Therefore their distribution and evolution, in terms of abundance as a function of mass and redshift, are closely connected to the properties of the underlying matter density field (e.g., Carlstrom et al., 2002). As such, they represent powerful probes of the evolution of the universe on large scales. Additionally, the deep potential wells of these systems make them ideal laboratories for probing the influence of various astrophysical processes on the large ($\sim$ 15% by mass) diffuse ionized gas component of these systems, the intracluster medium (ICM). This is because it is difficult for any energetic process that may influence

this medium to overcome the large gravitational potentials present and remove gas from the cluster halo. As such, observations of the thermal state of the ICM can constrain the time integrated effect of processes which have acted to reheat and redistribute this medium over the cluster's history (e.g., Voit, 2005).

Studies of the radial distribution of the thermodynamic properties (entropy, density and pressure) of the intracluster medium (ICM) have found remarkable self-similarity among a wide range of observed clusters. This self-similarity is found with respect to characteristic, mass-dependent, thermodynamic quantities when these profiles are expressed as a function of radius, rescaled to a characteristic radius, consistently defined with their mass and the critical density of the universe (Equation 1.12) at the cluster redshift. A review of these self-similar expecations can be found in Nagai et al. (2007b) and are outlined in Section 1.3.1. That these predictions are on average consistent with observations is indicative that gravity is the dominant contributor to the energetics of the ICM in these $> 10^{14}\,\mathrm{M}_{\odot}$ systems.

The self-similar scalings thus observed are widely used in the SZ literature, with the empirically calibrated radial pressure profile results of Arnaud et al. (2010) being a common choice in lieu of other constraints. This profile shape, and its expected self-similar scaling with mass, are used, for example, to calibrate SZ the mass scaling cluster cosmology studies (e.g., Hasselfield et al., 2013b) as well as to obtain estimates for integrated measures of the SZ signal (e.g. Y_{500}) from measurements of unresolved systems (Greco et al., 2015; Planck Collaboration et al., 2013b). We discuss the systematic effects of assuming a pressure profile in our results for the SZ signal associated with radio galaxies

(Gralla & Crichton et al. 2014, Section 2.6.2) and Le Brun et al. (2015) further discuss the importance in choosing a pressure profile when evaluating the integrated SZ signal of low mass systems.

Deviations around an assumed self-similar pressure profile clearly systematically affect studies which rely on it but, furthermore, measuring the deviations around and evolution of self-similar profiles of galaxy clusters can yield information about non-gravitational processes, which have important astrophysical implications. Energetic feedback processes, as well as active accretion in these systems, are able to redistribute or reheat the ICM. As shown in Figure 2.1, powerful AGN can have a disruptive effect on the gravitationally stratified gas. While this figure shows a particularly violent outburst, the time integrated energy output of AGN and stellar feedback can have a significant influence on the ICM, measurable in the average thermodynamic properties of cluster gas. In fact, some kind of reheating process is required to reheat the ICM at the dense cores of galaxy clusters in order to prevent catastrophic radiative cooling at rates much higher than those observed observed among the cluster population (e.g., Churazov et al., 2002; Peterson et al., 2003).

Additionally, self-similar thermodynamic predictions assume that it is only the thermal energy of these systems, which, in virial equilibirum with their gravitational potentials, is sustaining this gas against collapse. However, significant non-thermal contributions to the gas pressure may play a role as well. Such effects could be sourced by, for example, magnetic fields, turbulence or bulk motions within the gas (e.g., Battaglia et al., 2012; Dolag et al., 2005). Not accounting for these additional sources of pressure can lead to the so-

called hydrodynamic mass bias, where mass estimates of clusters based on thermodynamic arguments underpredict masses observed through more direct means (e.g., von der Linden et al., 2014). Simulations suggest that additional sources of ICM pressure from mergers and feedback effects account for $\sim 30\%$ of the hydrostatic support within the characteristic radius R_{500}. Such effects enhance scatter in the the SZ-mass scaling relation by 10–15% (e.g., Battaglia et al., 2010; Nelson et al., 2012) and potentially impact the pressure profiles by $> 10\%$ at $\sim R_{500}$. The potential of evaluating the effects of such astrophysical processes on the shape and scatter of self-similar pressure profiles have led to a wide range of studies of the ICM pressure (as well as entropy and density) distributions. The study of Arnaud et al. (2010) finds, using a combination of X-ray measurements from *XMM*-Newton and extrapolated hydrodynamic simulations, remarkable self-similarity in inferred mean pressure profile among a sample of local, $z < 0.2$, galaxy clusters, with less than 30% dispersion around this profile for radii of $R > 0.2R_{500}$. Sun et al. (2011) find similar profiles and scatter in low redshift ($z < 0.12$) but significantly lower mass ($M_{500} = 10^{13}$–$10^{14}\,\mathrm{M}_{\odot}$) X-ray galaxy groups. In their study of massive nearby $z \lesssim 0.3$ systems using the SZ effect observed in *Planck* data, Planck Collaboration et al. (2013a) found a a consistently fit self-similar profile, with typical dispersions of $\gtrsim$20% seen among their sample. Hydrodynamic simulations on the other hand, have typically found profiles that are in general agreement with the Planck Collaboration et al. (2013a) and Arnaud et al. (2010) profiles (e.g., Battaglia et al., 2012) with typical scatters around these profiles of $\sim$20% (Trac et al., 2011). Recently McDonald et al. (2014) presented a stacking analysis of shallow *Chandra*

data for a sample of SZ clusters from the South Pole Telescope (SPT).

Here, we present a study of the average SZ derived pressure profiles of SZ selected galaxy clusters out to high redshift ($0.23 \leq z \leq 1.07$). For this purpose, we use a combination of data from ACT and *Planck*. While we do not strongly detect evolution in the pressure profiles thus obtained we, for the first time, present evidence for much larger scatter in fits to a self-similarly scaled profile. This tendency is driven by the highest redshift half of our cluster sample ($z > 0.46$) whose dispersions are seen to reach values of 80–100% at $R < 0.5R_{500}$ compared to the observed scatter of $\sim 50\%$ seen in the low redshift ($z \leq 0.46$) half of our sample. Such large and evolving dispersions are not seen in simulated injected profiles recovered with our same methodology. In this thesis, this work is presented as a work in progress and has not yet been published.

4.2 Likelihood Formalism

With the goal of extracting a measurement of the average, self-similar, pressure profile of a catalog of galaxy clusters using the SZ effect, we develop a two-step modeling pipeline. The first step, which is discussed in this section, is to individually fit for the pressure profile shape of each cluster, while the further step of combining these noisy estimates into an average profile for a set of clusters, is discussed in Section 4.2.1.

To construct the individual profile fits, we use 148 GHz data from ACT's equatorial and southern surveys using the first generation ACT data described in Section 1.4. This

data, which is sensitive down to the $1\farcm4$ beam scales of ACT is used in conjunction with an optimally combined multi-frequency map of the inferred Compton-y signal derived from all sky *Planck* data (Planck Collaboration et al., 2016c). This map is constructed using the Modified Internal Linear Combination Algorithm (MILCA, Hurier et al., 2013) and is further described in Section 1.6. This *Planck* data has a much coarser resolution of $7'$ but enables us to simultaneously constrain the larger $> 7'$ angular scales at which the cluster signal in the ACT data becomes increasingly contaminated by the CMB. As the *Planck* data is made up from an optimal linear combination over multiple frequency bands in a manner that removes the CMB signal, it complements the ACT data well.

In the literature there exists a number of approaches for extracting an estimate for the three dimensional radial profiles of ICM properties from beam-convolved and on-sky projected X-ray and SZ data. These include the so-called onion peeling (e.g., Fabian et al., 1981) and regularized deprojection and deconvolution (e.g., Croston et al., 2006) algorithms. The latter of these methods, which is used in a number of recent studies of galaxy cluster X-ray and SZ pressure profiles (e.g., Arnaud et al., 2010; Planck Collaboration et al., 2013a), solves for the best-fit three dimensional profile that is consistent with an observed projected radial profile in a forwarded modeling approach. This method defines a linear map of a set of three dimensional radial estimates of a profile (at radii chosen a priori) to the projected data space and solve for the corresponding vector of constraints which minimizes the computed χ^2 when comparing the projected map to the data. For this process to be successful, a regularization scheme is required so that noise is not amplified into the

resulting deprojected constraints due to the non-trivial mapping between the model and the data. This regularization requires some model dependent choices but is conventionally internally calibrated using cross-validation techniques utilizing the data at hand (Croston et al., 2006).

In this work we take a different but analogous approach, motivated by both the complicated scale-dependent noise in the ACT data and the limited resolution ($1\farcm4$ compared to $0\farcs5$ and $6''$ angular resolutions of e.g. *Chandra* and *XMM*-Newton) at which the clusters in this sample are detected. This is necessary as, although we restrict this analysis to SZ clusters that are detected at high signal-to-noise, the signal-to-noise in any given radial bin can be small. In this regime, regularized deprojection techniques can break down (Bouchet, 1995). One method of overcoming these limitations is to stack many individual profiles, with an a priori rescaling to the same self-similar radius. The resulting high signal-to-noise stacked signal may then be deprojected using one of the above mentioned techniques. This process is, however, not suitable here. Since the ACT noise is strongly scale dependent, resizing stamps of multiple clusters and averaging the resulting signals produces a noise model that is difficult to quantify. In brief, our approach is instead to fit individual clusters with a flexible parameterized form for a three dimensional profile that we can project onto and subtract from our two dimensional data. We then take the angular power spectrum of the residual and compare it with expectations from a calibrated noise model for our data, which can be expressed naturally in angular power spectrum form. Through this modeling, we are able to obtain the posterior distribution of the parameters of our profile model

that can be transformed into constraints on a deprojected three dimensional angular radial profile. This process is described in detail below.

We first construct a parameterized model for the three dimensional pressure profile. For this purpose, we use the the generalized Navarro-Frenk-White (gNFW) profile (Nagai et al., 2007b; Navarro et al., 1996),

$$\frac{P_(r)}{P_{500}} = \frac{P_0}{(c_{500}x)^{\gamma}(1+(c_{500}x)^{\alpha})^{(\beta-\gamma)/\alpha}}, \tag{4.1}$$

where $x = R/R_{500}$, and the power-law indices, γ, α and β correspond to the logarithmic slope of the central, intermediate and outer radial regions of the pressure profile, respectively. The scale radius, R_{500}, corresponds to the radius within which the average matter overdensity is 500 times the critical density at the redshift of the cluster. From hydrostatic arguments, this can be related to a characteristic self-similar electron pressure, P_{500} (See Section 1.3.1, Equation 1.34 and surrounding discussion). For the work presented here, P_{500} is propagated from the constraints on R_{500} that are marginalized over in the fitting in a manner consistent with the uncertainties on the mass estimates for each cluster. In the study presented here, these constraints are derived from dynamical mass estimates for the cluster sample from Sifón et al. (2016). The parameter c_{500} controls the radial location of the turnover in logarithmic slopes. This parametric form for the self-similarly rescaled electron pressure has significant freedom in the range of deprojected profiles it is able to model. Profiles of this form are commonly fit to the deprojected profiles of X-ray and SZ

clusters (e.g., Arnaud et al., 2010; Planck Collaboration et al., 2013a) as well as data from hydrodynamic simulations of the ICM (e.g., Battaglia et al., 2012; Nagai et al., 2007b). In projecting this profile onto the sky, we assume that the cluster is spherically symmetric and therefore the on-sky Compton-y signal is related to the parametric profile (Equation 4.1) through

$$\hat{y}(\theta) = B \otimes \left[\frac{\sigma_{\rm T}}{m_{\rm e}c^2} P_{500} \int P_{\rm e}(\sqrt{l^2 + (\theta D_{\rm A}(z))^2})\, {\rm d}l \right]. \tag{4.2}$$

Here, a convolution is performed with a transfer function B which accounts for both the instrumental beam and the specific pixelization scheme of the data in question. The integral is performed along the line of sight, and the radial angular coordinate, θ, enters as an impact parameter along which the three dimensional radial profile is evaluated. From this projected radial profile we construct a two dimensional model, $M(\phi)$, centered on the cluster under consideration and representing the Compton-y signal corresponding to the projected signal of a gNFW profile with parameters $\phi = \{P_0, c_{500}, \gamma, \alpha, \beta, R_{500}\}$. This can be directly compared to the two dimensional raw data of the cluster in question, D.

In Figures 4.1 and 4.2 we show for two example clusters, on the top row, from left to right, the $12' \times 12'$ ACT stamp around a cluster (D), the residual after the projected model is subtracted ($D - M(\phi)$) and lastly the projected model, $M(\phi)$. The bottom row shows the same information for the $30' \times 30'$ *Planck* cutouts. These stamps have been moderately filtered to emphasize the angular scales of the cluster signals for visualization purposes. While, we do not strongly resolve the spatial signal in any particular cluster, as can be seen in these stamps, our goal here is to obtain unbiased (albeit noisy) estimates of the profiles

shapes that can be combined to derive constraints on the average profile of many clusters.

The final step in our approach is to construct a likelihood function in the space in which the noise in the maps is well defined — in terms of the angular power spectrum of the data. Since the scale-dependence present in the ACT data is predominantly in the form of contributions from the CMB, whose properties are well defined in terms of its angular power spectrum, this is a suitable choice.

To demonstrate the scale dependent nature of the noise, we show in Figure 4.3, the angular power spectra of the ACT and *Planck* data in the equatorial region in the left and right plots respectively. These are shown in conjunction with the angular power spectra of simulated galaxy clusters (convolved with the appropriate instrumental beams for each data set). These simulated cluster signals are derived from the gNFW profile corresponding to the best fit average profile from Arnaud et al. (2010). All power spectra shown in this plot are arbitrarily normalized, so their magnitudes should not be directly compared, but their relative contributions at different angular scales are apparent.

The likelihood function takes the form

$$-2\ln\mathcal{L}(\phi) \propto [\mathcal{F}^2(D-M(\phi))]_k^{\mathrm{T}}\mathbf{C}^{-1}[\mathcal{F}^2(D-M(\phi))]_k, \tag{4.3}$$

where $[\mathcal{F}^2(D-M(\phi))]_k$ represents the operation of taking the angular power spectrum of the residual model-subtracted data map that takes the form of a vector after being binned and averaged by the magnitude of the angular wavenumber $\vec{k}$. While, in principle, the co-

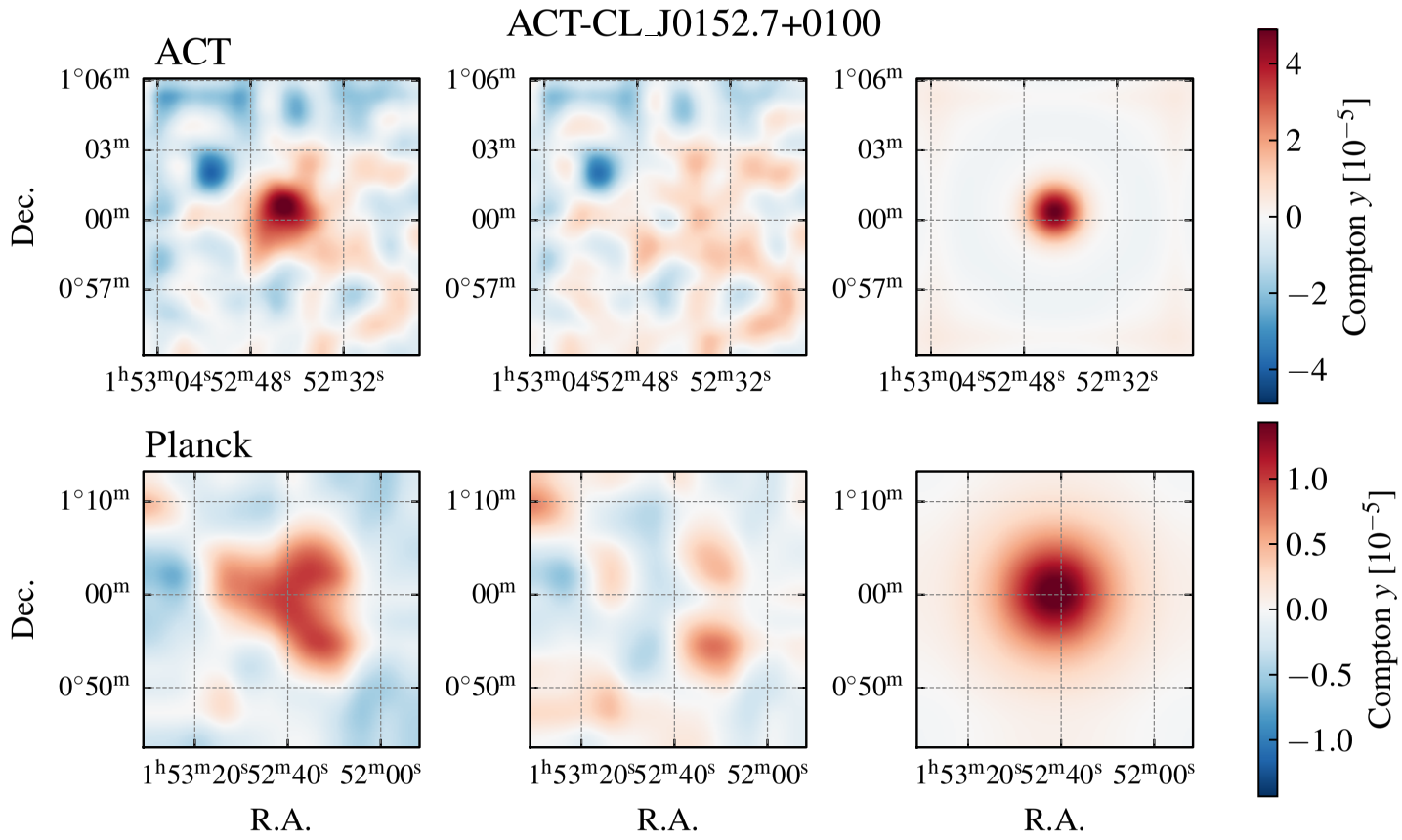

Figure 4.1: For galaxy cluster ACT-CL J0152.7+0100 ($z = 0.23$), we show: On the top row, extracted $12' \times 12'$ stamp of (from left to right) the raw ACT data, the residual after subtracting the best-fit projected pressure profile and lastly the projected model cluster. In the bottom row we show the corresponding extracted $12' \times 12'$ stamps from the Planck Compton-y map. To aid visualization, these data have been moderately filtered with bandpass filters which emphasize the angular scales of the cluster signal.

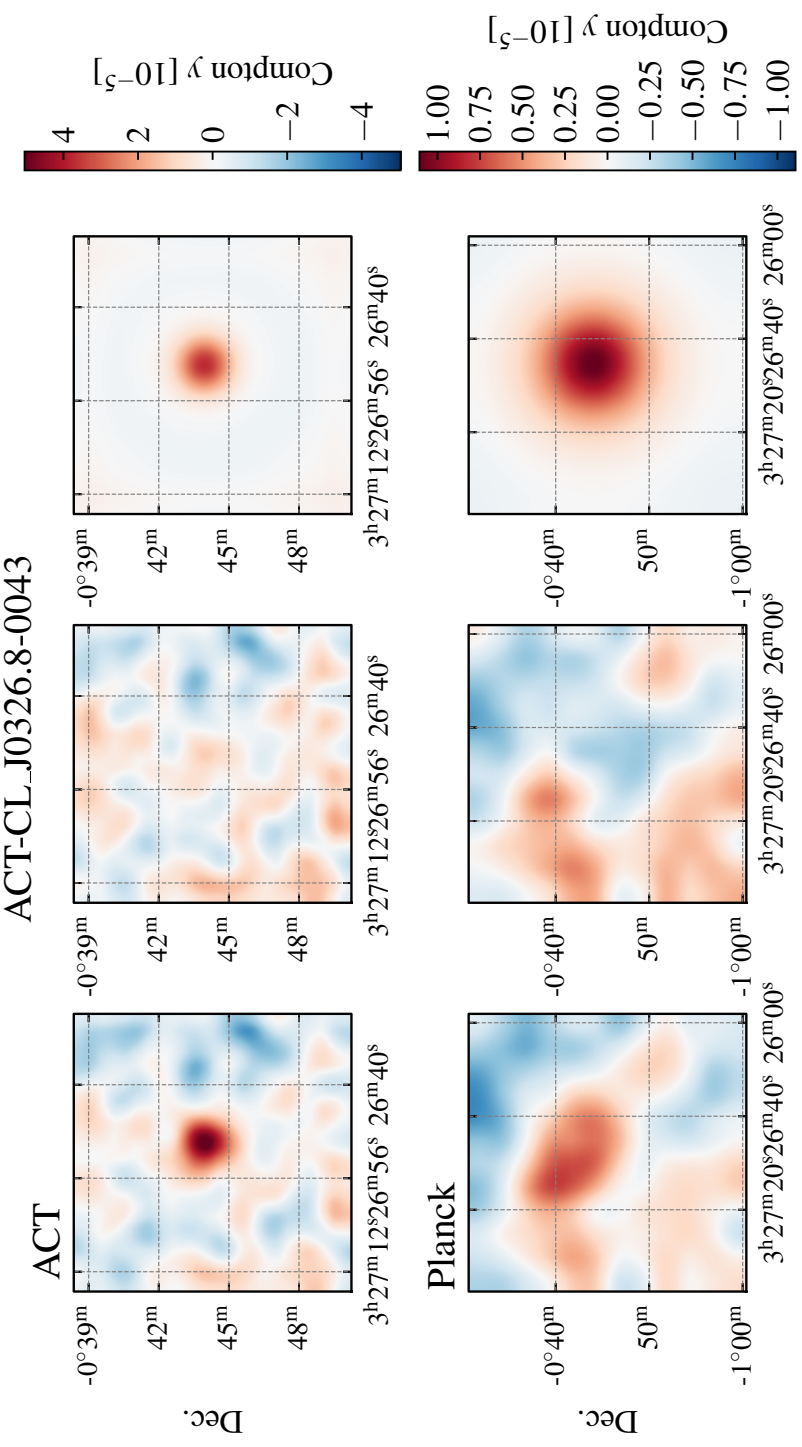

Figure 4.2: For galaxy cluster ACT-CL J0326.8-0043 ($z = 0.45$), we show: On the top row, extracted $12' \times 12'$ stamp of (from left to right) the raw ACT data, the residual after subtracting the best-fit projected pressure profile and lastly the projected model cluster. In the bottom row we show the corresponding extracted $12' \times 12'$ stamps from the Planck Compton-y map. To aid visualization, these data have been moderately filtered with bandpass filters which emphasize the angular scales of the cluster signal.

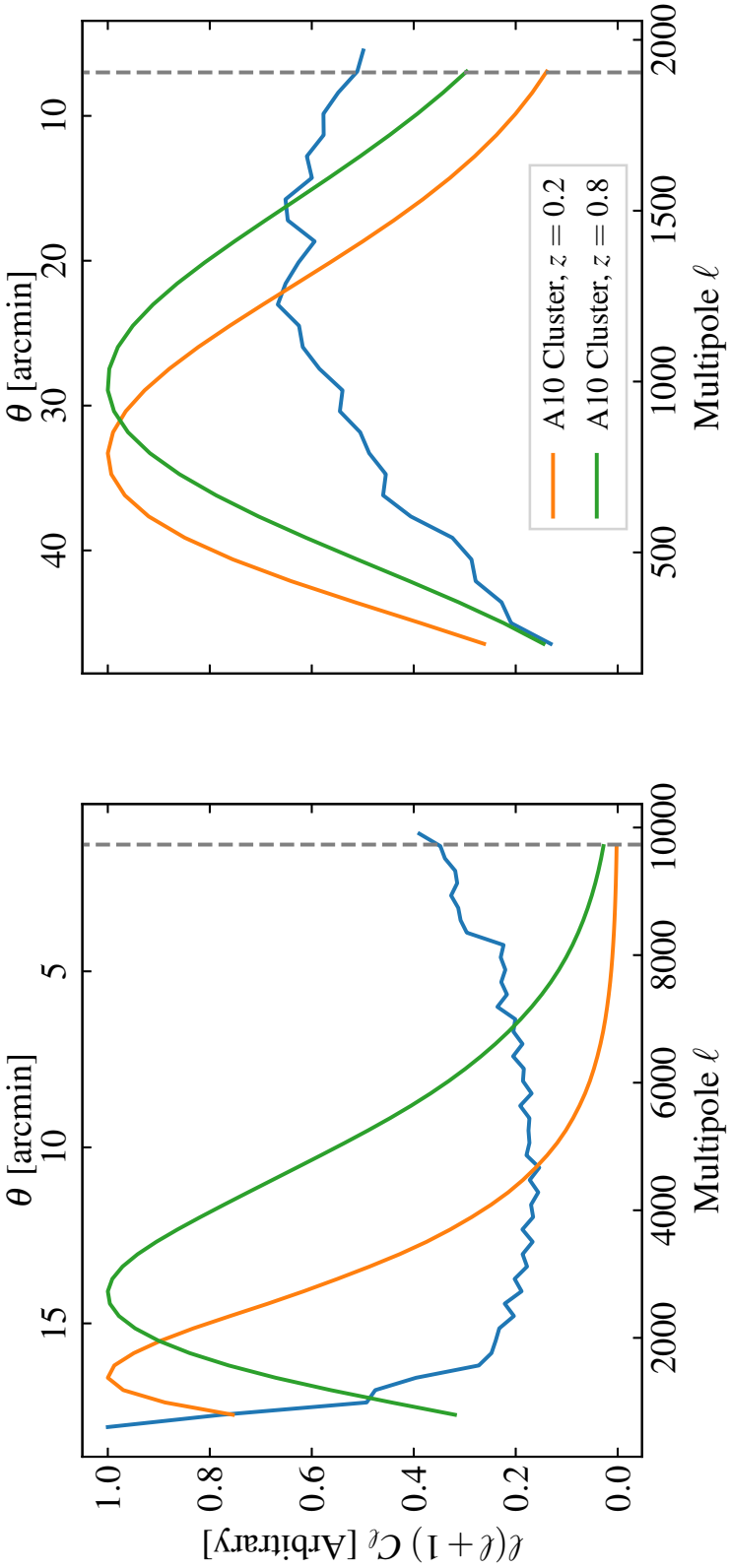

Figure 4.3: Blue: Arbitrarily normalized angular power spectra of the ACT (left) and *Planck* (right) data in the equatorial strip. Orange and green: The angular power spectra of injected galaxy clusters with gNFW profiles using the best-fit parameters of Arnaud et al. (2010), evaluated at $z = 0.2$ and $z = 0.8$, respectively and convolved with the appropriate beams. The magnitudes of these spectra should not be directly compared due to the arbitrary normalization used. The spectra are shown as a function of multipole ℓ with the corresponding angular scale shown on the top axis. The dashed lines show the FWHM of the instrument beams, indicating the limiting resolution of each dataset. This demonstrates the scale-dependent nature of the noise that needs to be accounted for when fitting for cluster profiles in these data.

variance matrices C for the binned power spectra of the ACT and *Planck* data could be derived from estimated instrumental noise and modeling for the other components contaminating the cluster signal (such as the CMB in the ACT data), we instead use an empirical approach for estimating them here. For this purpose, we evaluate the power spectrum of 1000 blank (avoiding known point sources and clusters) $12' \times 12'$ stamps of ACT data and 600 blank $30' \times 30'$ stamps of *Planck* data. We do this separately for each of the equatorial and southern ACT regions. We calculate the covariance matrix associated with each of these sets of null spectra and use these empirical covariance matrices in the likelihood function Equation 4.3.

For each cluster in our sample, we construct such a likelihood function for both the ACT and *Planck* data. We then employ an affine invariant MCMC sampling algorithm (EMCEE, Foreman-Mackey et al., 2013) to construct samples of the posterior distribution of the parameter vector ϕ, using the product of the likelihood functions for these two datasets. We employ uniform priors on $\log_{10} P_0 \in (-5,3)$, $\beta \in (1.515)$ and $\gamma \in (0,1)$. These bounds for β and γ are chosen so that the numerically evaluated line-of-sight integral of Equation 4.2 does not diverge. As there are regions in parameter space in which the gNFW parameters are highly degenerate and our data are due not strongly constrain the shape for any single given cluster, we cannot allow all of these parameters to vary freely. We therefore choose to impose Gaussian priors of $c_{500} = 1.177 \pm 0.2$ and $\alpha = 1.051 \pm 0.3$, based on the best-fit parameters from the study of Arnaud et al. (2010). For the scale radius R_{500}, we use a Gaussian prior based on the radius corresponding to a proxy for the mass of the cluster to

be fit, such as that described in Section 4.3.1. This represents another benefit of our method in that, in performing a Bayesian analysis, we are able to marginalize over the (potentially large) uncertainty on the scale radius with respect to which we are extracting profiles. This is in contrast to standard deprojection or stacking techniques which typically require point estimates for these values that need to be accurately obtained externally.

Figure 4.4 shows the results of this fitting process for 6 ACT-selected galaxy clusters (described in Section 4.3.1). Each of these plots show, for a different cluster, the gray region corresponding to the 68th percentile credible region occupied by the parameterized profiles extracted from the posterior distributions of the gNFW parameters for a particular fit. We also show here the purple points corresponding to volume averages of the three dimensional profile, binned by radius, with bin locations chosen so as to reduce covariance with adjacent bins. This process is discussed further in Section 4.2.1. The correlation matrices of these binned deprojected profiles are shown in the inset figures. The red line shows the best-fit gNFW parameters of Arnaud et al. (2010) to aid visual comparison between these plots.

4.2.1 Combining Profile Constraints

In Section 4.2 we showed how we model the posterior distribution for the parameters of the gNFW form for the pressure profile. These parameters, while representing constraints on the shape of the profiles, can be highly degenerate, with similar profiles able to be fit by significantly different sets of gNFW parameters. Therefore, while these posterior distributions contain information about the shapes of these profiles, a further step must be

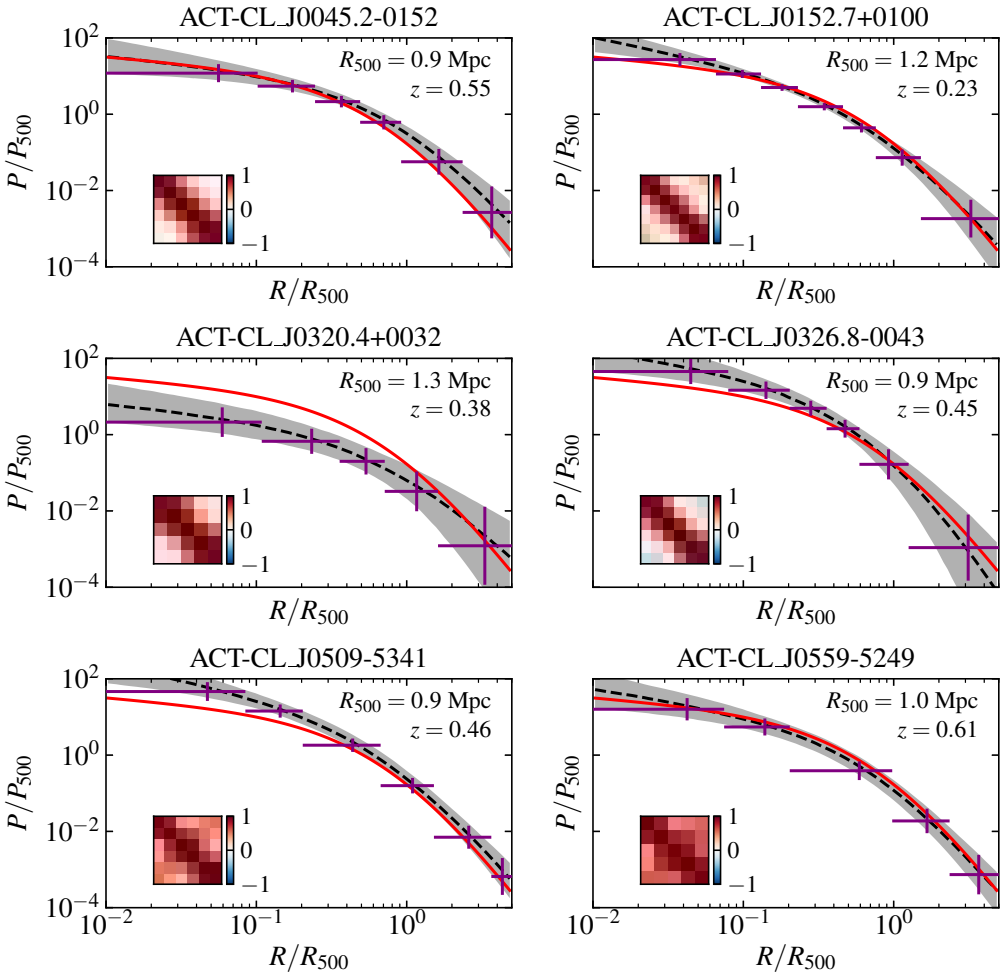

Figure 4.4: Extracted constraints on the three dimensional radial pressure profiles of 6 clusters from the catalog outlined in Section 4.3.1. The gray region in each of these plots shows the 68% credible region of our fits for the gNFW pressure profiles with the dashed black line corresponding to the 50th percentile of these same fits. These regions and lines are determined by evaluating the gNFW profile with parameters drawn from the posterior distributions from our MCMC chains for each cluster. The purple points show constraints on volume averages of these three dimensional profiles within radial bins chosen with sufficient spacing so as to reduce correlation with adjacent bins. The correlation matrices of these binned profiles are shown as the inset plots. The red line corresponds to a gNFW profile with parameters drawn from the best-fit values of the study of Arnaud et al. (2010) and is shown here only to aid in visually comparing the constraints on these different clusters.

taken to express these constraints in a manner in which they can be combined so as to determine an ensemble profile for a cluster catalog.

To do so, for a set of gNFW parameter samples drawn from the posterior distribution of each cluster fit, we evaluate the gNFW radial profile averaged within the three dimensional volume contained within each of a set of finely spaced bins in $x = R/R_{500}$. We then determine the correlation matrix between these bins and combine them into a coarser set such that the adjacent bins are determined to be no more the 75% correlated. We then reevaluate the volume averaged profiles in these coarse bins and compute the vector $\vec{P}_i$ (for cluster i) of the mean values (averaged over the samples of the gNFW parameter posterior distribution) of the pressure profile within these bins, and it's corresponding covariance matrix, C_i. This generates a Gaussian estimate for the constraint of a particular cluster in the space of $P/P_{500}(x)$ instead of in the more abstract space of the gNFW parameter posterior distribution. Examples of these constraints are shown in the purple points in Figure 4.4.

The advantage of reframing the obtained constraints in this manner is that we can now combine the pressure profile constraints from a number of different clusters. We write a new composite Gaussian likelihood function,

$$-2\ln\mathcal{L} \propto \sum_{i}^{\text{clusters}} (\vec{P}_i - \vec{B}_i(P_{500}(x))^T \mathsf{C}_i^{-1} (\vec{P}_i - \vec{B}_i(P/P_{500}(x))), \tag{4.4}$$

where $\vec{P}_i$ and C correspond to the calibrated binned constraints from an individual cluster i discussed above. $\vec{B}_i(P_{500}(x))$ represents the operation of binning a model pressure profile

$P/P_{500}(x)$ in the same manner as the binned constraints $\vec{P}_i$ for cluster i.

For the ensemble model profile $P/P_{500}(x)$ we will again make use of the gNFW parameterization, with the parameters $\phi = \{P_0, c_{500}, \gamma, \alpha, \beta\}$. These parameters now describe the ensemble profile of a set of clusters instead of the constaints on the profile of a single cluster. We do not model for intrinsic scatter around this profile. We sample for the posterior distribution of these parameters using an affine invariant MCMC sampling algorithm (EMCEE, Foreman-Mackey et al., 2013). Finally, we again use the posterior parameter distribution from gNFW fits to the average profile, to perform the same binned sampling of profiles as we did in the case of the individual chains. Thus we obtain not only constraints on the gNFW parameters of the average profiles, but these constraints projected into the space of the pressure profile, $P/P_{500}(x)$ and its associated bin to bin convariance matrix. An example of these extracted constraints on the average profile for a catalog of ACT galaxy clusters is shown in Figure 4.7.

4.3 Constraints on the Average Pressure Profiles of ACT Galaxy Clusters

4.3.1 The ACT Dynamical Cluster Catalog

While this method is generalizable to multiple samples of galaxy clusters overlapping with the ACT survey regions, we initially perform a pilot study of this method using a set

of ACT-selected galaxy clusters. These clusters have been detected in ACT data through a matched-filter analysis of their SZ signal at 148 GHz (assuming a scaled Arnaud et al., 2010, profile for the cluster shapes) in the southern (Marriage et al., 2011b) and equatorial (Hasselfield et al., 2013b) ACT surveys. This sample has been used to extract cosmological constraints using their observed abundance as a function of mass and redshift (Hasselfield et al., 2013b; Sehgal et al., 2011). The clusters have significant follow-up data available, with all having at least photometrically determined redshift measurements, either through overlapping deep optical surveys, or through dedicated photometric followup (Menanteau et al., 2013). Additionally, several of these clusters have auxiliary > 20 ks X-ray studies available through archival or dedicated followup programs with *XMM*-Newton and *Chandra*. A subsample of these systems have spectroscopic followup of multiple member galaxies, enabling a dynamical study of the gravitational potential of their dark matter halos (Sifón et al., 2013, 2016). This provides an accurate calibration of their masses which is independent of their SZ signal. For the work presented here, we use the sample of ACT-selected galaxy clusters with dynamical mass estimates as reported in Sifón et al. (2016).

Figure 4.5 shows the distribution of these 43 clusters as a function of their halo mass, expressed in terms of their dynamically determined masses, M_{500}, and redshift. This set of clusters spans a redshift range of $0.23 \leq z < 1.07$. In our study of the ensemble pressure profiles derived from this sample, we split this catalog into two subsamples by cutting above and below the median reshift of this sample, $z = 0.46$. This allows us to constrain possible evolution of the average pressure profile. The low redshift sample has a median redshift

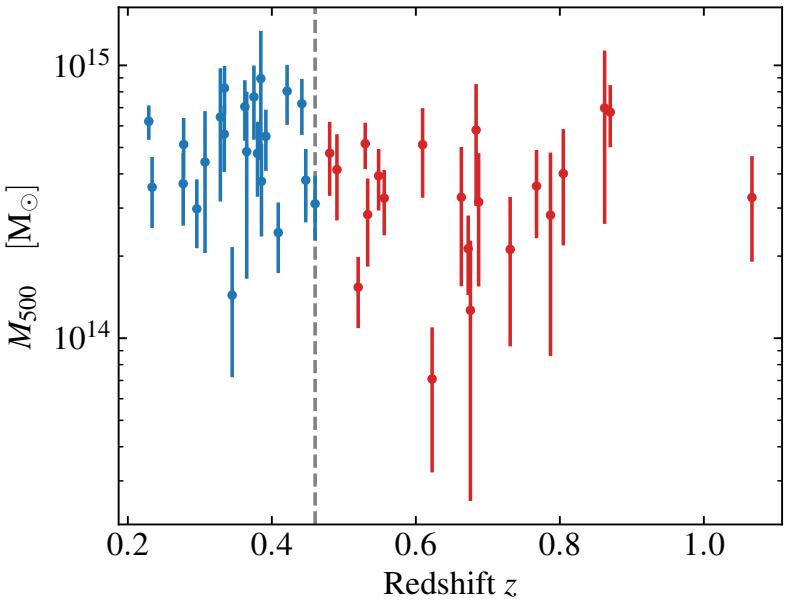

Figure 4.5: Redshift and mass distribution for the sample of ACT SZ detected galaxy clusters (Hasselfield et al., 2013b; Marriage et al., 2011b) with dynamical mass estimates and redshifts. The M_{200} values reported in Sifón et al. (2016) have been converted to M_{500} values following the halo concentration relation of Duffy et al. (2008). The median redshift of $z = 0.46$, defining the split between the low redshift (blue) and high redshift (red) subsamples, is displayed as the gray dashed line. The dynamical masses of these clusters are seen to have no strong dependence on redshift.

of $z_{med} = 0.37$ while the high redshift sample has a mean redshift of $z_{med} = 0.67$. For our fitting, we use the characteristic radii, R_{200}, as reported and determined in Sifón et al. (2016), converted to R_{500} using the halo concentration relation of Duffy et al. (2008). The radii thus determined, and their associated uncertainties, are used to construct priors that are marginalized over in the results reported here as discussed in Section 4.2. Figure 4.4 shows plots of the individual joint ACT and *Planck* pressure profile constraints from a subset of the clusters in this catalog, obtained through the method described in Section 4.2.

4.3.2 Ensemble Profiles

In this section we report the resulting constraints derived from applying the method outlined in Section 4.2 to the full catalog of clusters as described in Section 4.3.1, as well as to subsamples of this catalog split by redshift. By splitting in redshift, we attempt to constrain possible evolution in the average pressure profiles, and their dispersion, obtained through this method.

First, to verify the accuracy of our method, we inject simulated galaxy cluster signals into both the ACT and *Planck* data and attempt to recover the injected signal. For this purpose, we use the same catalog described in Section 4.3.1 for the simulated clusters masses and redshifts. This ensures that our simulated cluster catalogs have the same input properties as the catalog we use for our constraints from the real data. For the cluster signals, we inject smooth, gNFW profiles using the parameters for the best-fit pressure profile from Arnaud et al. (2010). These are injected at randomly chosen on sky locations. Following the method outlined previously, we construct estimates for the marginalized gNFW constraints on each of these profiles and then combine these constraints together in order to extract an average profile. We expect this average profile to be consistent with our choice of input profile signal.

Figure 4.6 shows the results of two separate random realizations of these simulations compared to the input profile. The lines show the binned constraints on the extracted average profiles in terms of the difference of these extracted constraints and the injected simulated profile binned in the same way. The points are rescaled by the square root of

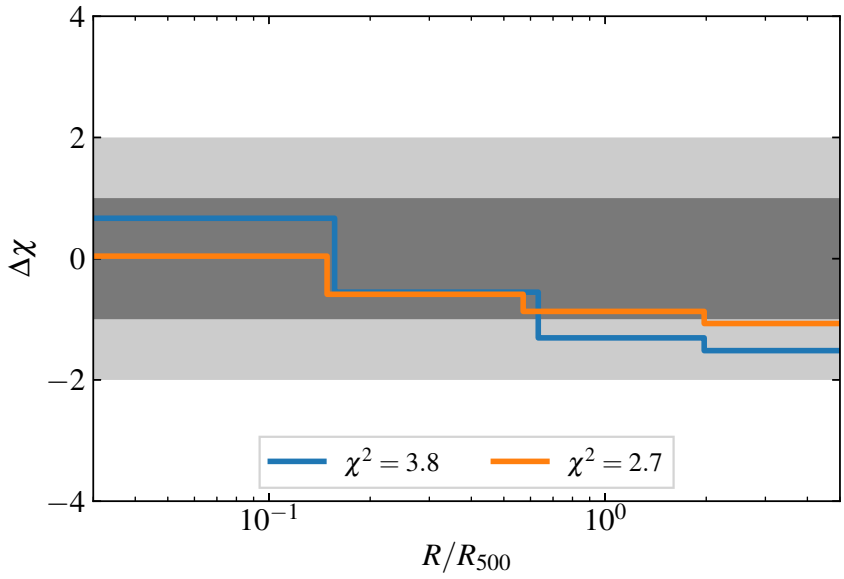

Figure 4.6: Residuals for the average pressure profiles of two realizations of simulated injected gNFW parameterized profiles using the Arnaud et al. (2010) parameter values. The legend shows the χ^2 values with respect to the hypothesis of the extracted signal being consistent with this injected signal. For 4 degrees of freedom, they correspond to probabilities to exceed of 0.43 and 0.61 for the blue and orange curve respectively.

the diagonal elements of the corresponding covariance matrix, such that the amplitude of each signal represents approximately the χ contribution of each point. These points are, however, significantly correlated (similarly to the constraints shown for the real data in Figure 4.7). Accounting for the full covariance matrix, we find the corresponding χ^2 values for the hypothesis of the extracted signal being consistent with the injected signal, for each of these realizations, are 3.8 and 2.7 respectively, for 4 degrees of freedom, corresponding to probabilities to exceed of 0.43 and 0.61. We therefore infer from this that our simulated injected profile is accurately recovered to within the uncertainties of our measurement.

We now present extracted constraints from the catalog of ACT galaxy clusters described in Section 4.3.1. Figure 4.7 shows the extracted fit for the average profile of the full cluster data set, displayed in the orange points as the binned average constraints. Pressure profiles from the X-ray and simulation based analysis of Arnaud et al. (2010) and the *Planck* based SZ analysis of Planck Collaboration et al. (2013a) are displayed alongside these constraints for reference. We also show, as the light gray lines, the extracted binned profile of each individual cluster in this sample (shown as the purple points for a subset of clusters in Figure 4.4). In Figure 4.8, we show constraints extracted in the same manner for each of the two redshift bins that we split our sample into. The lower panel of each of these plots shows a plot similar to that of Figure 4.6, showing the agreement comparing the best fit binned profiles and the profiles from the literature as a function of radial bin. In Table 4.1 we list the 50th percentile and bounds of the 68% credible regions for the marginalized gNFW parameters from the posterior distributions of the gNFW fits to these data. The

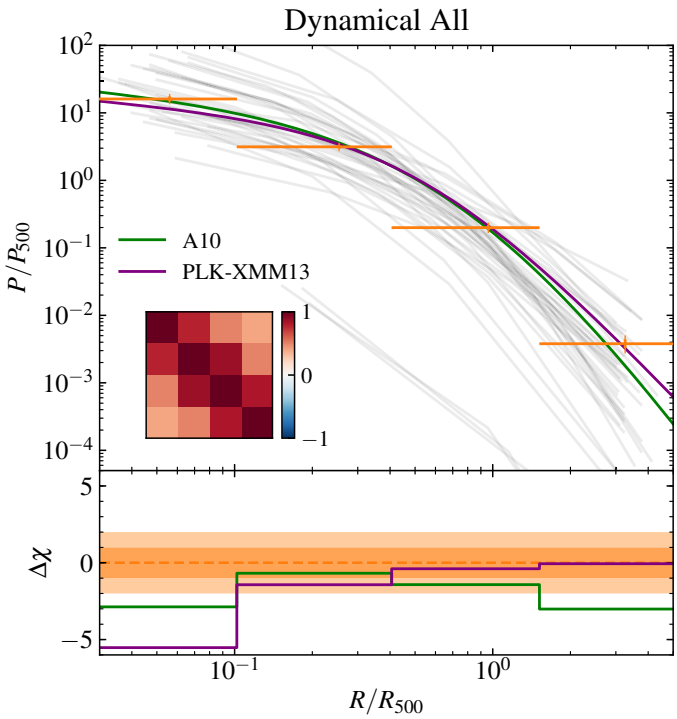

Figure 4.7: Extracted binned constraints on the average pressure profile of ACT SZ detected galaxy clusters with dynamical mass estimates from the catalog of Sifón et al. (2016) (orange points) The inset plot shows the correlation matrix of these binned constraints. The individual best-fit profiles are shown as the light gray lines. For comparison, we overplot the results for the best-fit gNFW profiles of Arnaud et al. (2010) in green and Planck Collaboration et al. (2013a) in purple. The lower panel shows the difference between our best fit average profile and those literature profiles binned in the same bins and rescaled by the square root of the diagonal elements of the estimated covariance matrix of our best-fit average profile. While we agree with the Planck Collaboration et al. (2013a) in the intermediate and outer radii, our constraints are consistent with significantly more signal than both literature profiles in the $R < 0.1R_{500}$ radial regime.

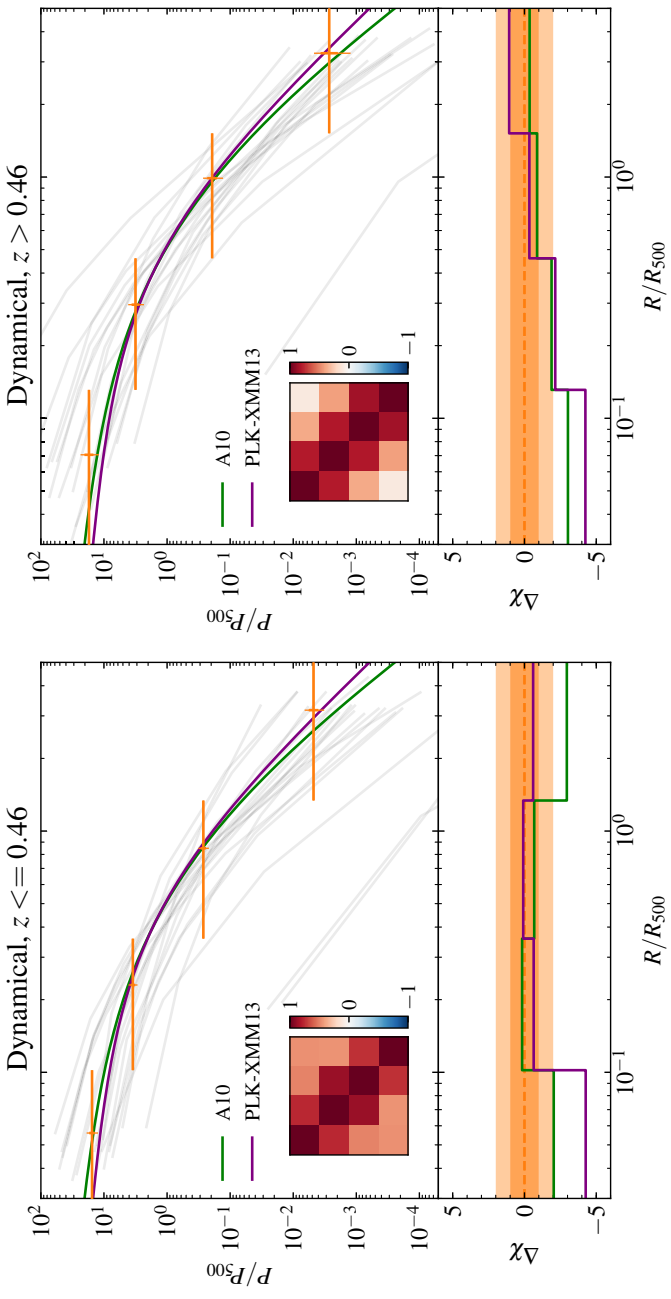

Figure 4.8: Extracted binned constraints on the average pressure profile of ACT SZ detected galaxy clusters in the low redshift bin (left) and high redshift bin (right). The inset plots show the correlation matrices of these binned constraints. Individual best-fit profiles are shown as the light gray lines in both plots. Additionally, we overplot the results for the best-fit gNFW profiles of Arnaud et al. (2010) in green and Planck Collaboration et al. (2013a) in purple. The lower panels show the difference between our best fit average profile and these literature profiles binned in the same bins and rescaled by the square root of the diagonal elements of the estimated covariance matrix of these best-fit average profiles. We find that the average profile for the low redshift and high redshift are not significantly different. Accounting for the full covariance matrix in each constraint, we determine a χ^2 value of 8.3 (for 4 degrees of freedom), for the null hypothesis that the difference in these profiles is consistent with zero. corresponding to a probability to exceed of 0.08.

Table 4.1: Marginalized constraints on the best-fit gNFW parameters for the average pressure profiles of SZ clusters. The covariance between these parameters is shown in the marginalized parameter contours of Figure 4.9.

	$\log_{10} P_0$	γ	α	β	c_{500}
All Clusters					
($z_{med} = 0.46$)	$0.67^{+0.07}_{-0.07}$	$0.60^{+0.05}_{-0.05}$	$1.05^{+0.05}_{-0.05}$	$4.89^{+0.19}_{-0.19}$	$1.13^{+0.06}_{-0.06}$
Low z Clusters					
($z_{med} = 0.37$)	$0.68^{+0.09}_{-0.09}$	$0.59^{+0.07}_{-0.06}$	$1.00^{+0.06}_{-0.06}$	$4.74^{+0.26}_{-0.24}$	$1.13^{+0.07}_{-0.08}$
High z Clusters					
($z_{med} = 0.67$)	$0.79^{+0.12}_{-0.11}$	$0.61^{+0.07}_{-0.07}$	$1.10^{+0.08}_{-0.08}$	$5.35^{+0.40}_{-0.36}$	$1.16^{+0.09}_{-0.09}$

marginalized constraints on these parameters, derived from these results, are plotted in Figure 4.9.

The principal result of this study is the observation that the dispersions in the individually fit pressure profiles appear to be a) higher than dispersions typically found in self-similar pressure profiles and b) dependent on redshift. This can be seen in the scatter of the gray lines in Figures 4.7 and 4.8, but is more clearly demonstrated in Figure 4.10. Here we show, as a function of R/R_{500}, the dispersion (formulated in terms of the percentage relative scatter) in the individually fit profiles around the best fit average gNFW profile observed in our cluster samples. The solid lines show this for the full ACT galaxy cluster sample while the dashed lines shown the same measurement for a realization of simulated injected clusters. The colors indicate dispersions measured for different subsamples, with the low redshift ($z_{med} = 0.37$) sample shown in blue and the high redshift ($z_{med} = 0.67$) shown in red. The full sample is shown as the orange curve. We split the simulated catalog using the same redshift cut. We observe, for our full sample, relative dispersions on the order of $\gtrsim$70% with values of $\gtrsim$50% and 80–100% for the low and high redshift samples

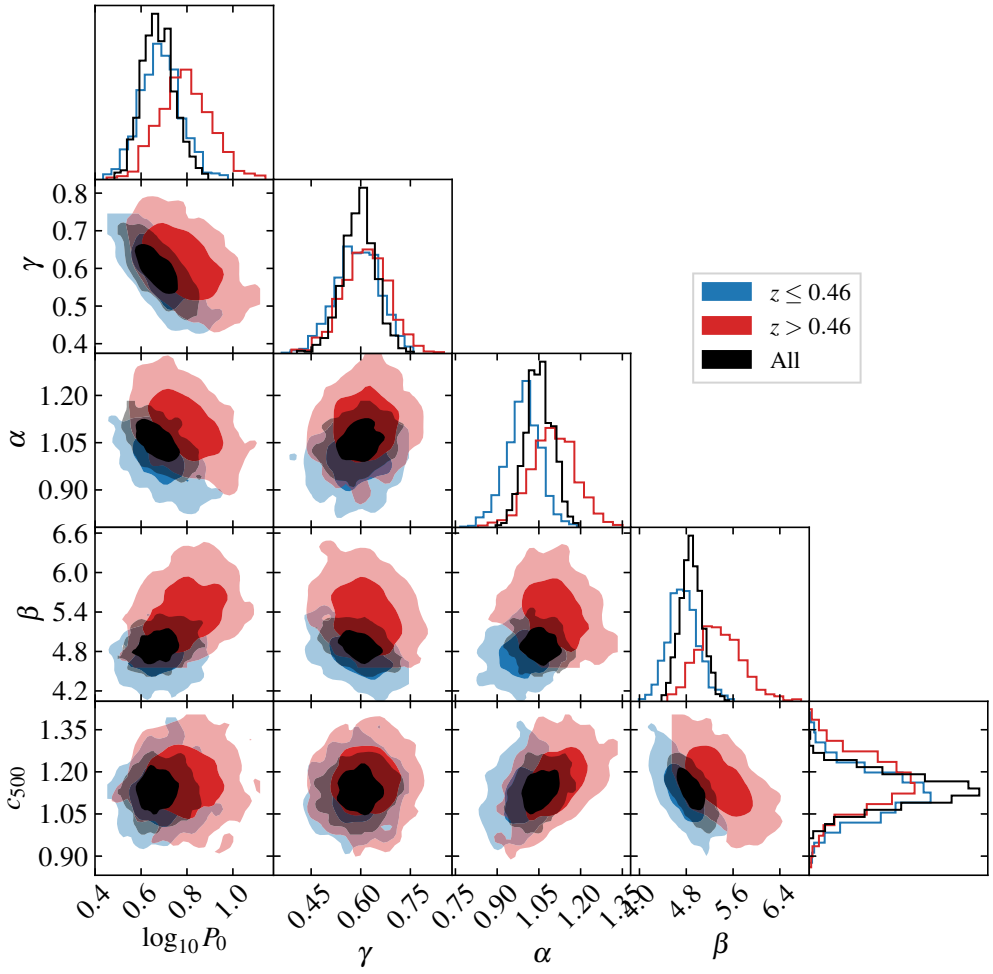

Figure 4.9: Contours for the 68% and 95% credible regions for the marginalized gNFW parameter constraints for average profiles of the ACT dynamical cluster sample. In black, the constraints for the full samples are shown while the blue and red contours show the constraints for the low redshift ($z \leq 0.46$) and high redshift ($z > 0.46$) samples, respectively. These parameters are found to be in broad agreement for all samples.

respectively. The dispersions from the simulated clusters are found to be $\gtrsim 40\%$ increasing somewhat at high radii but have a much weaker trend with redshift than the ACT cluster sample, particularly at $R/R_{500} < 0.5$. This indicates that a significant contributor to the evolution of the dispersion is inherent in the data and not our methodology. It is unlikely that such evolution could be due to selection effects, as the sample is drawn from an SZ-selected (and hence approximately mass limited) catalog. This increase in observed pressure profile scatter has not been previously observed within a consistently evaluated sample. While Sayers et al. (2013) use a Gaussian process technique to estimate the intrinsic scatter of SZ pressure profiles observed with Bolocam (separate from the scatter due to instrumental noise), they do not split their $0.15 < z < 0.89$ sample of X-ray selected clusters by redshift. They extract constraints on the intrinsic scatter on the order of 15–25% at $R = 0.2R_{500}$ and 30-50% at $R = 0.2R_{500}$ around their simultaneously constrained best fit profile. Naïvely assuming the total scatter we observe is the quadratic sum of measurement scatter and intrinsic scatter, this implies that the intrinsic scatter present in our samples within $R \lesssim 0.5R_{500}$ are $\sim$60%, 45% and 70–90% for the full, low redshift and high redshift samples respectively. A more robust approach for separating out measurement noise and intrinsic scatter will be presented in future work. Such evolution in the intrinsic scatter with redshift can be interpreted as the increased relevancy of non-gravitational effects at early epochs in cosmic evolution. Such results are not reported in simulations that observe typical scatters around their mean profiles of $\sim 20\%$ (Trac et al., 2011).

We additionally compare our results for the shapes of the extracted average profiles to

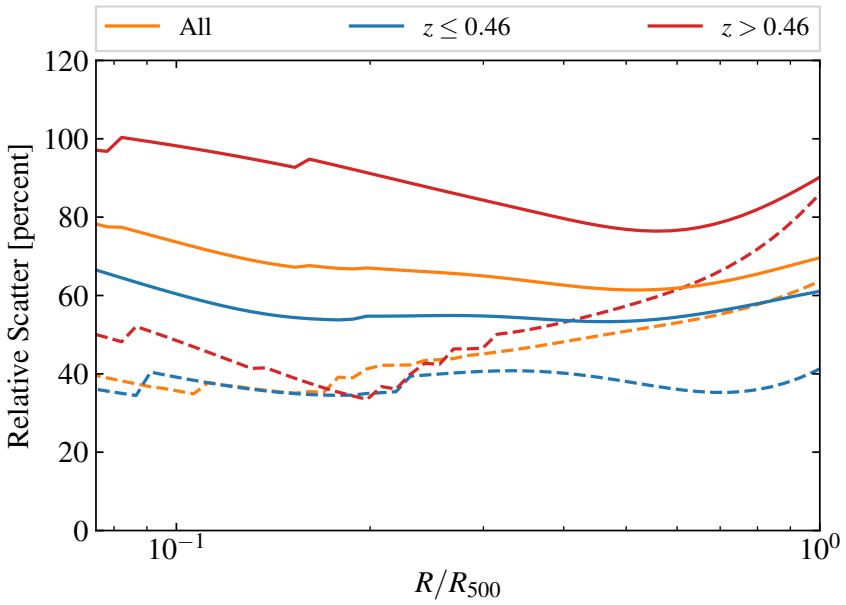

Figure 4.10: Estimated dispersions of the best-fit individual cluster profiles around the best-fit average cluster profile for different subsamples of our clusters, as a function of radius. The orange represents the dispersion for the full sample while the blue and red respresent dispersions for the low redshift ($z \leq 0.46$) and high redshift ($z > 0.46$) samples, respectively. The dashed lines show the same dispersions for extracted profiles from simulated injected cluster signals, split into redsift bins in the same way. The data clearly show significantly more scatter than one would expect, given the results from injected simulations, attributable to intrinsic scatter within the cluster population. Additionally, much of this excess scatter is seen to originate from the clusters in the high redshift subsample.

profiles derived from other studies in the literature. However, for reasons outlined below, it is difficult to make a direct comparison. We find that, in general, for $R \gtrsim 0.1R_{500}$, our results for these clusters are consistent with the constraint of Planck Collaboration et al. (2013a). We see the same tendency they observed in their sample of low redshift clusters for excess SZ signal out to high radii, $R \gtrsim R_{500}$, when compared to expectations from the Arnaud et al. (2010) fit to X-ray data.

In the core ($R \lesssim 0.1R_{500}$) of these clusters this consistency breaks down. We find our constraints on the deprojected average pressure profile is consistently higher than both the Arnaud et al. (2010) and Planck Collaboration et al. (2013a), despite recovering well simulated injected profiles in this radial regime (Figure 4.6). Unfortunately, at these radii, it is very difficult to make a direct comparison with other studies as the differences in approaches in the choice of the center around which models are fit, can introduce strong systematic effects. McDonald et al. (2014) motivates an approach for defining the center in their X-ray data based on the large scale centroid as opposed to the X-ray peak used in the studies of Arnaud et al. (2010), Planck Collaboration et al. (2013a) and Sayers et al. (2013). They show that for certain, morphologically disturbed, systems this can shift the assumed central location by $R = 0.3R_{500}$, which would correspond to more than half an ACT beam FWHM for the typical cluster redshifts in our sample. They show that the choice between these two different X-ray centers can make a 50% difference in the extracted density profile in the cores.

Here, as we are developing a method for extracting constraints for arbitrary samples

of SZ clusters in our data, which may or may not have auxiliary observations of the ICM, we use the SZ detection centers in our modeling. The literature profiles to which we are comparing all utilize some manner of X-ray derived centering. While SZ observations are less sensitive to density substructures than X-ray surface brightness observations, this still makes direct comparison difficult. Our centers are defined by evaluating the positions in the matched-filtered ACT data at which the data response is maximized assuming for the fiducial shape of the signal, a gNFW profile using the Arnaud et al. (2010) parameters. While this does take into account some large scale information about the cluster due to the filter used, since the position is chosen to maximize the response, this choice likely, on average, biases the SZ derived pressure profile high compared to what would be extracted by choosing a center location obtained from an independent approach. It is therefore likely that differences in centering play some role in the disagreement at $R \lesssim 0.1R_{500}$ but the degree to which this could contribute needs to be further investigated and will be treated in future work. One avenue our method allows for is the marginalization over cluster center location (using some prior estimate) when individually fitting the parameterized profiles for each cluster. This can yield constraints that account for possible biases imposed by our current centering on the SZ detection peak.

Split into redshift bins, we see no strong evolution in the profiles we derived. We find that the average profile for the low redshift ($z_{med} = 0.37$) and high redshift ($z_{med} = 0.37$) show no strong evidence of evolution. Taking into account the full covariance matrices in both profile contraints, we determine $\chi^2 = 8.3$ (for 4 degrees of freedom), for the null

hypothesis that the difference in these profiles is consistent with zero, corresponding to a probability to exceed of 0.08. The consistency of our obtained profiles can also be observed in the agreement of the gNFW parameter values shown in Figure 4.9 and Table 4.1.

This is in contrast with the observations of McDonald et al. (2014) who detect a strong increase in pressure by up to $\sim 50\%$ from $z \sim 0.8$ to $z \sim 0.5$ at $R < 0.1R_{500}$ that they attribute to the increasing density of growing cool cores. However, this observation is most significant at $R < 0.1R_{500}$, necessitating a higher resolution study, such as their *Chandra* based analysis, to probe in detail. High resolution SZ imaging of a similarly selected sample, such as that available with MUSTANG-2 (Dicker et al., 2014), an instrument on the Green Bank Telescope, could also constrain this evolution.

4.4 Conclusion

In this pilot study of ACT-selected SZ clusters, we detail a new method for extracting individual, SZ derived, pressure profiles from a combination of ACT and *Planck* data. These individual profiles are then combined into ensemble estimates of the average pressure profiles.

In our results, we find broad consistency in the shape of our profiles with that derived for the nearby, $z \lesssim 0.3$, systems in Planck Collaboration et al. (2013a), for $R > 0.1R_{500}$. While for $R < 0.1R_{500}$ this agreement breaks down, the effects of different techniques for centering the profiles need to be further explored in order to interpret this result. We

additionally find that the extracted average profile shapes shows strong signs of evolution with redshift.

We detect significantly more dispersion around our average profiles than has been observed previously and for the first time demonstrate that this dispersion is considerably higher in high redshift systems, increasing from $\sim$45% in our low redshift ($z_{med} = 0.37$) sample to $\sim$70–90% in our high redshift ($z_{med} = 0.37$) sample. This is indicative that a self-similarly scaled average pressure profile is a worse fit for any given cluster at earlier epochs in the universe's evolution and points to the increased relevancy of non-gravitational effects on the distribution of pressure in these systems, especially within $R < 0.5R_{500}$.

This method is generalizable to arbitrarily large samples of galaxy clusters with overlapping ACT data. Therefore applying these techniques to, for example, the large SZ cluster catalogs derived from forthcoming ACT survey data, such as the deeper and wider survey fields of ACTPol (Niemack et al., 2010) and Advanced ACTPol (Henderson et al., 2016), will yield enhanced constraints on these profiles. This will additionally allow for finer binning by redshift in order to further explore evolution in these observations.

Chapter 5

Conclusions

In this thesis I have presented three studies, all based on observational constraints provided by the thermal Sunyaev-Zel'dovich effect. I have leveraged this effect to investigate the thermodynamic state of collapsed structures — galaxies and galaxy clusters — and compared the results with expectations from self-similar scalings based on purely gravitational arguments.

In the first of these studies (Chapter 2), I presented the results of Gralla & Crichton et al. (2014) where, using a stacking approach with data from ACT and *Herschel*-SPIRE, we measured the average radio to far-infrared SEDs of radio-selected galaxies. We found that the emission from this 1.4 GHz-selected catalog was well modeled by a combination of a strong synchrotron component as well as a contribution from dusty emission at higher frequencies. In the millimeter, our modeling indicated the necessity of an additional component in the form of the SZ effect, which we detected at the 5σ level. While, due to their

selection, the majority of these systems likely host AGN, with power jets influencing their surroundings, we found the amplitude of this signal is consistent with expectations from self-similar arguments for purely gravitationally heated gas.

Second, I presented the results of Crichton et al. (2016) (Chapter 3), where a similar stacking approach is performed for optically selected radio-quiet quasars using ACT and *Herschel*-SPIRE data. We modeled the millimeter to far-infrared SEDs of these quasars in the redshift range $0.5 < z < 3.5$, finding that they are dominated by a luminous gray-body signal associated with re-radiated emission, likely from both the quasar itself and star formation associated within its host galaxy. We additionally found evidence for the requirement of an SZ contribution to the SEDs in the millimeter bands at the 3–4σ level, depending on the model used. In contrast with the radio galaxy study, we found that the magnitude of this signal is difficult to explain with purely gravitational arguments. Additionally, when modeling this SZ contribution as being due to energetic coupling of the quasar radiative output to the surrounding medium, this observed SZ signal is found to be consistent with an efficiency of this coupling of $(14.5 \pm 3.3)\tau_8^{-1}\%$, where τ_8 is the typical quasar active lifetime in units of 10^8 yr.

Finally, in Chapter 4, I presented a recent, as yet unpublished, study of the SZ pressure profiles derived for a sample of SZ selected ACT clusters. Here we motivated a new approach for extracting individual pressure profiles from ACT and *Planck* data as well as a method for combining the extracted individual noisy measurements into an estimate for the average, self-similarly scaled, pressure profile. By splitting a sample of SZ selected ACT

clusters, with dynamical mass estimates, into two redshift bins, we searched for evidence of evolution in the self-similar distribution of pressure in these massive systems. We found that, while the shapes of the average pressure profiles thus obtained are not significantly evolving between our two redshift bins ($z \sim 0.37$ to 0.67), there are large differences in the intrinsic scatter around these average profiles. Within $R < 0.5R_{500}$, we observed the 45% intrinsic scatter in the low redshift sample increasing to 70–90% in the high redshift sample. Such evolution has not been previously observed and could be indicative of the increased relevancy of non-gravitational processes in earlier epochs of cosmic history. This work will be extended with a more sophisticated approach for separating out instrumental and modeling based dispersion from intrinsic scatter as well as an evaluation of the effects of different profile centering choices on the extracted results.

Appendix A

Stacking

In this Appendix, I outline the statistical foundation upon which stacking is based. This discussion represents an expanded derivation based on the discussions found in Marsden et al. (2009) and Viero et al. (2013) and uses similar notation to these works.

Stacking is a method for constructing unbiased estimates for the average flux of a catalog of sources whose individual fluxes may be well below the noise limit of the data in question. While stacking is often presented as taking a simple weighted average of individual noise estimates, a more formal derivation of this fact acts to demonstrate the assumptions required for this to hold true.

This derivation starts with generating a likelihood function for the average flux of a dataset and then maximizing said likelihood in order to obtain the estimator.

We will assume that the data we are stacking takes the form of a map, M_i, in the form of measurements in discrete pixels indexed by i. This data is assumed to arise from the

contributions of an arbitrary number of catalogs $\alpha, \beta, ...$ of sources, each representing a source population with a mean flux $S_\alpha, S_\beta, ...$ The goal of this process is to obtain an unbiased estimate of the average flux S_α, of one of the contributing catalogs, α, given knowledge of the locations in the map of the sources in this catalog.

The data in pixel i can, on average, be modeled by

$$M_i = \sum_{\gamma}^{\text{catalogs}} S_\gamma N_{i,\gamma} + \sigma_i. \tag{A.1}$$

Here, $N_{i,\gamma}$ represents the number of sources from catalog γ in pixel i. The quantity σ_i represents some random noise contribution to this pixel. In order for the final result to be unbiased, it is necessary for the mean of this map to be subtracted and, for the sake of simplicity, we perform this subtraction upfront, relating the mean-subtracted map M' to the catalog contributions,

$$M'_i = \sum_{\gamma}^{\text{catalogs}} S_\gamma (N_{i,\gamma} - \mu_\gamma) + \sigma_i, \tag{A.2}$$

where $\mu_\gamma = \langle N_{i,\gamma} \rangle_{\text{pixels}}$ is the mean number of sources from catalog γ in each pixel.

If the noise contributions σ_i are Guassian and do not correlate with any of the catalogs N_γ (note that this is not typically the case for catalogs selected from the same data on which they are stacked), we can write a likelihood function:

$$-2 \ln \mathcal{L} \propto \sum_{i}^{\text{pixels}} \frac{(M'_i - \sum_\gamma^{\text{catalogs}} S_\gamma (N_{i,\gamma} - \mu_\gamma))^2}{\sigma_i^2}. \tag{A.3}$$

Maximizing this likelihood function for the average flux of a specific catalog α, S_α one finds:

$$\frac{\partial \ln \mathcal{L}}{\partial S_\alpha} = 0 \tag{A.4}$$

$$0 = \sum_i^{\text{pixels}} \left[M_i'(N_{i,\alpha} - \mu_\alpha) - \left[\sum_\gamma^{\text{catalogs}} S_\gamma (N_{i,\gamma} - \mu_\gamma) \right] (N_{i,\alpha} - \mu_\alpha) \right]. \tag{A.5}$$

The fact that M' is a mean subtracted map helps in simplifying this expression, as

$$\mu_\alpha \sum_i^{\text{pixels}} M_i' = 0, \tag{A.6}$$

since μ_α is a constant.

Additionally, since $N_{i,\gamma} - \mu_\gamma$ is explicitly mean subtracted,

$$\mu_\alpha \sum_i^{\text{pixels}} (N_{i,\gamma} - \mu_\gamma) = 0, \tag{A.7}$$

for all γ. We therefore have:

$$0 = \sum_i^{\text{pixels}} \left[M_i' N_{i,\alpha} - \left[\sum_\gamma^{\text{catalogs}} S_\gamma (N_{i,\gamma} - \mu_\gamma) \right] N_{i,\alpha} \right] \tag{A.8}$$

$$= \sum_i^{\text{pixels}} \left[M_i' N_{i,\alpha} - S_\alpha (N_{i,\alpha} - \mu_\alpha)^2 - \left[\sum_{\gamma \neq \alpha}^{\text{catalogs}} S_\gamma N_{i,\gamma} \right] N_{i,\alpha} \right], \tag{A.9}$$

where the second sum has had the terms from the catalog of interest, α, separated out.

The most significant assumption is that none of the source catalogs contributing to emission in the map are correlated with the catalog of interest or, put formally,

$$\sum_{i}^{\text{pixels}} \sum_{\gamma \neq \alpha}^{\text{catalogs}} S_\gamma N_{i,\gamma} N_{i,\alpha} = 0. \tag{A.10}$$

The requirement of this assumption to hold true represents the most significant potential bias of stacking studies: unknown correlated emission. While, in this formalism, the requirement is explicitly that there exists no correlations with any other source population within map pixels, in realistic data, the requirement is that there should be no significant correlations within the beam scale of the instrument in order for stacking to be unbiased. Whether this assumption holds is typically difficult to verify in real data and is often problematic in stacking studies.

However, under the assumption that this requirement holds we obtain for the maximum likelihood estimator of $\hat{S}_\alpha$, the so-called stacking equation:

$$\hat{S}_\alpha = \frac{\sum_i^{\text{pixels}} M_i' N_{i,\alpha}}{\sum_i^{\text{pixels}} (N_{i,\alpha} - \mu_\alpha)^2} \tag{A.11}$$

$$= \frac{\sum_i^{\text{pixels}} M_i' N_{i,\alpha}}{N_{\text{pixels}} \sigma_\alpha^2}. \tag{A.12}$$

Here, N_{pixels} is the number of pixels in the map and σ_α^2 is the pixel-space variance of catalog counts from catalog α.

One further assumption is often employed — that $N_{i,\alpha}$ is Poisson distributed and hence $N_{\rm pixels}\sigma^2_{N_{i,\alpha}} = N_{\rm pixels}\mu_\alpha = \sum_i^{\rm pixels} N_{i,\alpha} = N_{{\rm cat},\alpha}$, the number of sources in catalog α. Finally this leads to the familiar average of the data at pixel locations in the map once the sum is reformed to be over data at the coordinates of sources in the catalog:

$$\hat{S}_\alpha = \frac{\sum_j^{\rm catalog\ \alpha} M'_j}{N_{{\rm cat},\alpha}}. \tag{A.13}$$

We have assumed here that the noise contributions are uniform over map pixels, but this result simply generalizes to the inverse-variance weighted average in the case of non-uniform noise (so long as the weights do not strongly correlate with source positions).

Bibliography

Arav, N., Moe, M., Costantini, E., et al. 2008, ApJ, 681, 954

Arnaud, M., Neumann, D. M., Aghanim, N., et al. 2001, A&A, 365, L80

Arnaud, M., Pratt, G. W., Piffaretti, R., et al. 2010, A&A, 517, A92

Astropy Collaboration, Robitaille, T. P., Tollerud, E. J., et al. 2013, A&A, 558, A33

Battaglia, N., Bond, J. R., Pfrommer, C., & Sievers, J. L. 2012, ApJ, 758, 74

Battaglia, N., Bond, J. R., Pfrommer, C., Sievers, J. L., & Sijacki, D. 2010, ApJ, 725, 91

Becker, R. H., White, R. L., & Helfand, D. J. 1995, ApJ, 450, 559

Beelen, A., Cox, P., Benford, D. J., et al. 2006, ApJ, 642, 694

Bell, E. F. 2003, ApJ, 586, 794

Best, P. N., & Heckman, T. M. 2012, MNRAS, 421, 1569

Best, P. N., Kauffmann, G., Heckman, T. M., et al. 2005, MNRAS, 362, 25

BIBLIOGRAPHY

Best, P. N., von der Linden, A., Kauffmann, G., Heckman, T. M., & Kaiser, C. R. 2007, MNRAS, 379, 894

Birkinshaw, M. 1999, Phys. Rep., 310, 97

Bleem, L. E., Stalder, B., de Haan, T., et al. 2015, ApJS, 216, 27

Bohren, C. F., & Huffman, D. R. 1983, Absorption and scattering of light by small particles

Bouchet, L. 1995, A&AS, 113, 167

Bower, R. G., Benson, A. J., Malbon, R., et al. 2006, MNRAS, 370, 645

Boyle, B. J., & Terlevich, R. J. 1998, MNRAS, 293, L49

Brookes, M. H., Best, P. N., Peacock, J. A., Röttgering, H. J. A., & Dunlop, J. S. 2008, MNRAS, 385, 1297

Bryan, G. L., & Norman, M. L. 1998, ApJ, 495, 80

Carico, D. P., Keene, J., Soifer, B. T., & Neugebauer, G. 1992, PASP, 104, 1086

Carlstrom, J. E., Holder, G. P., & Reese, E. D. 2002, ARA&A, 40, 643

Cen, R., & Safarzadeh, M. 2015a, ApJ, 798, L38

—. 2015b, ApJ, 809, L32

Choi, E., Ostriker, J. P., Naab, T., & Johansson, P. H. 2012, ApJ, 754, 125

Churazov, E., Sunyaev, R., Forman, W., & Böhringer, H. 2002, MNRAS, 332, 729

BIBLIOGRAPHY

Ciotti, L., & Ostriker, J. P. 2001, ApJ, 551, 131

Condon, J. J. 1989, ApJ, 338, 13

Condon, J. J., Broderick, J. J., Seielstad, G. A., Douglas, K., & Gregory, P. C. 1994, AJ, 107, 1829

Cowie, L. L., Songaila, A., Hu, E. M., & Cohen, J. G. 1996, AJ, 112, 839

Crenshaw, D. M., Kraemer, S. B., & George, I. M. 2003, ARA&A, 41, 117

Crichton, D., Gralla, M. B., Hall, K., et al. 2016, MNRAS, 458, 1478

Croston, J. H., Arnaud, M., Pointecouteau, E., & Pratt, G. W. 2006, A&A, 459, 1007

Croton, D. J., Springel, V., White, S. D. M., et al. 2006, MNRAS, 365, 11

Dai, Y. S., Bergeron, J., Elvis, M., et al. 2012, ApJ, 753, 33

de Haan, T., Benson, B. A., Bleem, L. E., et al. 2016, ApJ, 832, 95

de Zotti, G., Massardi, M., Negrello, M., & Wall, J. 2010, A&A Rev., 18, 1

Di Matteo, T., Springel, V., & Hernquist, L. 2005, Nature, 433, 604

Dicker, S. R., Ade, P. A. R., Aguirre, J., et al. 2014, Journal of Low Temperature Physics, 176, 808

DiPompeo, M. A., Myers, A. D., Hickox, R. C., Geach, J. E., & Hainline, K. N. 2014, MNRAS, 442, 3443

BIBLIOGRAPHY

DiPompeo, M. A., Myers, A. D., Hickox, R. C., et al. 2015, MNRAS, 446, 3492

Dodelson, S. 2003, Modern cosmology

Dolag, K., Vazza, F., Brunetti, G., & Tormen, G. 2005, MNRAS, 364, 753

Duffy, A. R., Schaye, J., Kay, S. T., & Dalla Vecchia, C. 2008, MNRAS, 390, L64

Dunkley, J., Calabrese, E., Sievers, J., et al. 2013, J. Cosmology Astropart. Phys., 7, 25

Dunlop, J. S., & Peacock, J. A. 1990, MNRAS, 247, 19

Dünner, R., Hasselfield, M., Marriage, T. A., et al. 2013, ApJ, 762, 10

Dutta Chowdhury, D., & Chatterjee, S. 2017, ApJ, 839, 34

Eisenstein, D. J., Weinberg, D. H., Agol, E., et al. 2011, AJ, 142, 72

Elvis, M., Wilkes, B. J., McDowell, J. C., et al. 1994, ApJS, 95, 1

Fabbri, R. 1981, Ap&SS, 77, 529

Fabian, A. C., Hu, E. M., Cowie, L. L., & Grindlay, J. 1981, ApJ, 248, 47

Fabian, A. C., Sanders, J. S., Ettori, S., et al. 2000, MNRAS, 318, L65

Faucher-Giguère, C.-A., & Quataert, E. 2012, MNRAS, 425, 605

Ferrarese, L., & Merritt, D. 2000, ApJ, 539, L9

Ferraro, S., Hill, J. C., Battaglia, N., Liu, J., & Spergel, D. N. 2016, Phys. Rev. D, 94, 123526

BIBLIOGRAPHY

Fixsen, D. J. 2009, ApJ, 707, 916

Foreman-Mackey, D., Hogg, D. W., Lang, D., & Goodman, J. 2013, PASP, 125, 306

Fowler, J. W., Niemack, M. D., Dicker, S. R., et al. 2007, Appl. Opt., 46, 3444

Friedmann, A. 1922, Zeitschrift fur Physik, 10, 377

Gallagher, S. C., Hines, D. C., Blaylock, M., et al. 2007, ApJ, 665, 157

Gebhardt, K., Bender, R., Bower, G., et al. 2000, ApJ, 539, L13

Ghisellini, G., Celotti, A., Fossati, G., Maraschi, L., & Comastri, A. 1998, MNRAS, 301, 451

Gonçalves, T. S., Steidel, C. C., & Pettini, M. 2008, ApJ, 676, 816

Gralla, M. B., Gladders, M. D., Yee, H. K. C., & Barrientos, L. F. 2011, ApJ, 734, 103

Gralla, M. B., Crichton, D., Marriage, T. A., et al. 2014, MNRAS, 445, 460

Greco, J. P., Hill, J. C., Spergel, D. N., & Battaglia, N. 2015, ApJ, 808, 151

Greene, J. E., Zakamska, N. L., Ho, L. C., & Barth, A. J. 2011, ApJ, 732, 9

Griffin, M. J., Abergel, A., Abreu, A., et al. 2010, A&A, 518, L3

Griffin, M. J., North, C. E., Schulz, B., et al. 2013, MNRAS, 434, 992

Griffith, M. R., & Wright, A. E. 1993, AJ, 105, 1666

BIBLIOGRAPHY

Guth, A. H., & Pi, S.-Y. 1982, Physical Review Letters, 49, 1110

Hajian, A., Acquaviva, V., Ade, P. A. R., et al. 2011, ApJ, 740, 86

Hand, N., Appel, J. W., Battaglia, N., et al. 2011, ApJ, 736, 39

Hand, N., Addison, G. E., Aubourg, E., et al. 2012, Physical Review Letters, 109, 041101

Hao, J., McKay, T. A., Koester, B. P., et al. 2010, ApJS, 191, 254

Hardcastle, M. J., Ching, J. H. Y., Virdee, J. S., et al. 2013, MNRAS, 429, 2407

Hasselfield, M., Moodley, K., Bond, J. R., et al. 2013a, ApJS, 209, 17

Hasselfield, M., Hilton, M., Marriage, T. A., et al. 2013b, J. Cosmology Astropart. Phys., 7, 8

Henderson, S. W., Allison, R., Austermann, J., et al. 2016, Journal of Low Temperature Physics, 184, 772

Ho, S., Hirata, C., Padmanabhan, N., Seljak, U., & Bahcall, N. 2008, Phys. Rev. D, 78, 043519

Hogg, D. W. 1999, ArXiv Astrophysics e-prints, astro-ph/9905116

Hopkins, P. F., Hernquist, L., Cox, T. J., et al. 2005a, ApJ, 630, 705

—. 2006, ApJS, 163, 1

Hopkins, P. F., Hernquist, L., Cox, T. J., & Kereš, D. 2008, ApJS, 175, 356

BIBLIOGRAPHY

Hopkins, P. F., Hernquist, L., Martini, P., et al. 2005b, ApJ, 625, L71

Hu, W., & Dodelson, S. 2002, ARA&A, 40, 171

Huang, J.-S., Rigopoulou, D., Magdis, G., et al. 2014, ApJ, 784, 52

Hurier, G., Macías-Pérez, J. F., & Hildebrandt, S. 2013, A&A, 558, A118

Ineson, J., Croston, J. H., Hardcastle, M. J., et al. 2013, ApJ, 770, 136

Jakobsen, P., Jansen, R. A., Wagner, S., & Reimers, D. 2003, A&A, 397, 891

Kaiser, N. 1986, MNRAS, 222, 323

—. 1991, ApJ, 383, 104

Kim, J., Park, C., Rossi, G., Lee, S. M., & Gott, III, J. R. 2011, Journal of Korean Astronomical Society, 44, 217

Kimball, A. E., & Ivezić, Ž. 2008, AJ, 136, 684

Kirkpatrick, A., Pope, A., Alexander, D. M., et al. 2012, ApJ, 759, 139

Krawczyk, C. M., Richards, G. T., Mehta, S. S., et al. 2013, ApJS, 206, 4

Lacey, C., & Cole, S. 1993, MNRAS, 262, 627

Le Brun, A. M. C., McCarthy, I. G., & Melin, J.-B. 2015, MNRAS, 451, 3868

Lin, Y.-T., Partridge, B., Pober, J. C., et al. 2009, ApJ, 694, 992

BIBLIOGRAPHY

Linde, A. D. 1982, Physics Letters B, 108, 389

Lisenfeld, U., Isaak, K. G., & Hills, R. 2000, MNRAS, 312, 433

Liu, G., Zakamska, N. L., Greene, J. E., Nesvadba, N. P. H., & Liu, X. 2013a, MNRAS, 430, 2327

—. 2013b, MNRAS, 436, 2576

Madau, P., Pozzetti, L., & Dickinson, M. 1998, ApJ, 498, 106

Magorrian, J., Tremaine, S., Richstone, D., et al. 1998, AJ, 115, 2285

Mandelbaum, R., Li, C., Kauffmann, G., & White, S. D. M. 2009, MNRAS, 393, 377

Marconi, A., Risaliti, G., Gilli, R., et al. 2004, MNRAS, 351, 169

Marriage, T. A., Baptiste Juin, J., Lin, Y.-T., et al. 2011a, ApJ, 731, 100

Marriage, T. A., Acquaviva, V., Ade, P. A. R., et al. 2011b, ApJ, 737, 61

Marsden, D., Gralla, M., Marriage, T. A., et al. 2014a, MNRAS, 439, 1556

—. 2014b, MNRAS, 439, 1556

Marsden, G., Ade, P. A. R., Bock, J. J., et al. 2009, ApJ, 707, 1729

Martini, P. 2004, in in Coevolution of Black Holes and Galaxies (Cambridge: Cambridge University Press), ed. L. C. Ho, 169

Martini, P., & Weinberg, D. H. 2001, ApJ, 547, 12

BIBLIOGRAPHY

Massardi, M., Ekers, R. D., Murphy, T., et al. 2011, MNRAS, 412, 318

McDonald, M., Benson, B. A., Vikhlinin, A., et al. 2014, ApJ, 794, 67

McNamara, B. R., & Nulsen, P. E. J. 2007, ARA&A, 45, 117

McNamara, B. R., Wise, M., Nulsen, P. E. J., et al. 2000, ApJ, 534, L135

Menanteau, F., Sifón, C., Barrientos, L. F., et al. 2013, ApJ, 765, 67

Mocanu, L. M., Crawford, T. M., Vieira, J. D., et al. 2013, ApJ, 779, 61

Murray, N., Chiang, J., Grossman, S. A., & Voit, G. M. 1995, ApJ, 451, 498

Nagai, D., Kravtsov, A. V., & Vikhlinin, A. 2007a, ApJ, 668, 1

Nagai, D., Vikhlinin, A., & Kravtsov, A. V. 2007b, ApJ, 655, 98

Navarro, J. F., Frenk, C. S., & White, S. D. M. 1996, ApJ, 462, 563

—. 1997, ApJ, 490, 493

Negrello, M., Hopwood, R., De Zotti, G., et al. 2010, Science, 330, 800

Negrello, M., Clemens, M., Gonzalez-Nuevo, J., et al. 2013, MNRAS, 429, 1309

Nelson, K., Rudd, D. H., Shaw, L., & Nagai, D. 2012, ApJ, 751, 121

Neto, A. F., Gao, L., Bett, P., et al. 2007, MNRAS, 381, 1450

Niemack, M. D., Ade, P. A. R., Aguirre, J., et al. 2010, in Proc. SPIE, Vol. 7741, Millimeter, Submillimeter, and Far-Infrared Detectors and Instrumentation for Astronomy V, 77411S

Nims, J., Quataert, E., & Faucher-Giguère, C.-A. 2015, MNRAS, 447, 3612

Novak, G. S., Ostriker, J. P., & Ciotti, L. 2011, ApJ, 737, 26

Oliver, S. J., Bock, J., Altieri, B., et al. 2012, MNRAS, 424, 1614

Pâris, I., Petitjean, P., Aubourg, É., et al. 2014, A&A, 563, A54

Patanchon, G., Ade, P. A. R., Bock, J. J., et al. 2008, ApJ, 681, 708

Pedregosa, F., Varoquaux, G., Gramfort, A., et al. 2011, Journal of Machine Learning Research, 12, 2825

Peebles, P. J. E. 1980, The large-scale structure of the universe

Peterson, J. R., Kahn, S. M., Paerels, F. B. S., et al. 2003, ApJ, 590, 207

Planck Collaboration, Aghanim, N., Arnaud, M., et al. 2011, A&A, 536, A12

Planck Collaboration, Ade, P. A. R., Aghanim, N., et al. 2013a, A&A, 550, A131

—. 2013b, A&A, 557, A52

—. 2016a, A&A, 594, A13

Planck Collaboration, Aghanim, N., Arnaud, M., et al. 2016b, A&A, 594, A22

—. 2016c, A&A, 594, A22

Planck Collaboration, Ade, P. A. R., Aghanim, N., et al. 2016d, A&A, 594, A24

—. 2016e, A&A, 594, A27

Press, W. H., & Schechter, P. 1974, ApJ, 187, 425

Proga, D., Stone, J. M., & Kallman, T. R. 2000, ApJ, 543, 686

Rawlings, S., & Jarvis, M. J. 2004, MNRAS, 355, L9

Reichard, T. A., et al. 2003, AJ, 125, 1711

Rephaeli, Y. 1995, ARA&A, 33, 541

Reyes, R., Zakamska, N. L., Strauss, M. A., et al. 2008, AJ, 136, 2373

Richards, G. T., Lacy, M., Storrie-Lombardi, L. J., et al. 2006a, ApJS, 166, 470

Richards, G. T., Strauss, M. A., Fan, X., et al. 2006b, AJ, 131, 2766

Richardson, J., Zheng, Z., Chatterjee, S., Nagai, D., & Shen, Y. 2012, ApJ, 755, 30

Riechers, D. A., Bradford, C. M., Clements, D. L., et al. 2013, Nature, 496, 329

Ruan, J. J., McQuinn, M., & Anderson, S. F. 2015, ApJ, 802, 135

Sadler, E. M., Jackson, C. A., Cannon, R. D., et al. 2002, MNRAS, 329, 227

Sadler, E. M., Ricci, R., Ekers, R. D., et al. 2006, MNRAS, 371, 898

Sajina, A., Partridge, B., Evans, T., et al. 2011, ApJ, 732, 45

Sayers, J., Mroczkowski, T., Czakon, N. G., et al. 2013, ApJ, 764, 152

BIBLIOGRAPHY

Scannapieco, E., & Oh, S. P. 2004, ApJ, 608, 62

Schirber, M., Miralda-Escudé, J., & McDonald, P. 2004, ApJ, 610, 105

Schneider, D. P., Richards, G. T., Hall, P. B., et al. 2010, AJ, 139, 2360

Schneider, P. 2006, Extragalactic Astronomy and Cosmology

Sehgal, N., Trac, H., Acquaviva, V., et al. 2011, ApJ, 732, 44

Sehgal, N., Addison, G., Battaglia, N., et al. 2013, ApJ, 767, 38

Shen, Y., Strauss, M. A., Oguri, M., et al. 2007, AJ, 133, 2222

Shen, Y., McBride, C. K., White, M., et al. 2013, ApJ, 778, 98

Sherwin, B. D., Das, S., Hajian, A., et al. 2012, Phys. Rev. D, 86, 083006

Sievers, J. L., Hlozek, R. A., Nolta, M. R., et al. 2013, J. Cosmology Astropart. Phys., 10, 60

Sifón, C., Menanteau, F., Hasselfield, M., et al. 2013, ApJ, 772, 25

Sifón, C., Battaglia, N., Hasselfield, M., et al. 2016, MNRAS, 461, 248

Soergel, B., Giannantonio, T., Efstathiou, G., Puchwein, E., & Sijacki, D. 2017, MNRAS, 468, 577

Springel, V., Di Matteo, T., & Hernquist, L. 2005, MNRAS, 361, 776

Sun, M., Sehgal, N., Voit, G. M., et al. 2011, ApJ, 727, L49

BIBLIOGRAPHY

Sunyaev, R. A., & Zeldovich, I. B. 1980, ARA&A, 18, 537

Sunyaev, R. A., & Zeldovich, Y. B. 1970, Ap&SS, 7, 3

Swetz, D. S., Ade, P. A. R., Amiri, M., et al. 2011, ApJS, 194, 41

Symeonidis, M., Willner, S. P., Rigopoulou, D., et al. 2008, MNRAS, 385, 1015

Tasker, N. J., Condon, J. J., Wright, A. E., & Griffith, M. R. 1994, AJ, 107, 2115

Thornton, R. J., Ade, P. A. R., Aiola, S., et al. 2016, ApJS, 227, 21

Thoul, A. A., & Weinberg, D. H. 1995, ApJ, 442, 480

Tinker, J., Kravtsov, A. V., Klypin, A., et al. 2008, ApJ, 688, 709

Trac, H., Bode, P., & Ostriker, J. P. 2011, ApJ, 727, 94

Trainor, R., & Steidel, C. C. 2013, ApJ, 775, L3

Turnshek, D. A. 1984, ApJ, 280, 51

Urry, C. M., & Padovani, P. 1995, PASP, 107, 803

Vantyghem, A. N., McNamara, B. R., Russell, H. R., et al. 2014, MNRAS, 442, 3192

Verdier, L., Melin, J.-B., Bartlett, J. G., et al. 2016, A&A, 588, A61

Vieira, J. D., Crawford, T. M., Switzer, E. R., et al. 2010, ApJ, 719, 763

Viero, M. P., Moncelsi, L., Quadri, R. F., et al. 2013, ApJ, 779, 32

BIBLIOGRAPHY

Viero, M. P., Asboth, V., Roseboom, I. G., et al. 2014, ApJS, 210, 22

Vikhlinin, A., Kravtsov, A., Forman, W., et al. 2006, ApJ, 640, 691

Vogelsberger, M., Genel, S., Springel, V., et al. 2014, MNRAS, 444, 1518

Voit, G. M. 2005, Reviews of Modern Physics, 77, 207

von der Linden, A., Mantz, A., Allen, S. W., et al. 2014, MNRAS, 443, 1973

Wang, L., Viero, M., Ross, N. P., et al. 2015, MNRAS, 449, 4476

Weinberg, S. 2008, Cosmology (Oxford University Press)

Weymann, R. J., Carswell, R. F., & Smith, M. G. 1981, ARA&A, 19, 41

White, M., Myers, A. D., Ross, N. P., et al. 2012, MNRAS, 424, 933

White, R. L., Becker, R. H., Helfand, D. J., & Gregg, M. D. 1997, ApJ, 475, 479

Worseck, G., Fechner, C., Wisotzki, L., & Dall'Aglio, A. 2007, A&A, 473, 805

Wyithe, J. S. B., & Loeb, A. 2003, ApJ, 595, 614

Xu, C., Livio, M., & Baum, S. 1999, AJ, 118, 1169

York, D. G., Adelman, J., Anderson, Jr., J. E., et al. 2000, AJ, 120, 1579

Zakamska, N. L., & Greene, J. E. 2014, MNRAS, 442, 784

Zubovas, K., & King, A. 2012, ApJ, 745, L34

Vita

Devin Thomas Crichton was born in Johannesburg, South Africa on the 23rd of February 1988, and is the son of Christine Crichton and Dr Graham Thomas Crichton. He attended the University of KwaZulu-Natal, completing a B.Sc (Honors) in 2009 and an M.Sc. in Mathematical Sciences (with astrophysics focus) in 2011. Devin joined the Johns Hopkins University in 2011, funded through the Fulbright Foreign Student program. Here, he obtained an M.A. in Physics and Astronomy in 2013 and completed the requirements for Ph.D. candidacy in 2014. The work presented in this thesis was defended on July 17th 2017 and the final version of this thesis was submitted on July 19th 2017.